# REAL TIME DETECTION AND CLASSIFICATION OF SUBSURFACE TARGETS USING SFCW GPR

## A DISSERTATION

*Submitted in partial fulfillment of the requirements for the award of the degree of*

**INTEGRATED DUAL DEGREE**

**(Bachelor of Technology and Master of Technology)**

**in**

**ELECTRONICS AND COMMUNICATION ENGINEERING**

**(With Specialization in Wireless Communication)**

**By**

**SHASHI KANT PANDEY**



**DEPARTMENT OF ELECTRONICS AND COMPUTER ENGINEERING**
**INDIAN INSTITUTE OF TECHNOLOGY ROORKEE**
**ROORKEE -247 667 (INDIA)**

**JUNE, 2011**

## CANDIDATE'S DECLARATION

I hereby declare that the work, presented in this dissertation report, entitled **"Real Time Detection and Classification of Subsurface Targets Using SFCW GPR,"** being submitted in fulfillment of partial requirements for the award of the degree of Integrated Dual Degree (Bachelor of Technology and Master of Technology) in Electronics and Communication Engineering with Specialization in Wireless Communication, in the Department of Electronics and Computer Engineering, Indian Institute of Technology, Roorkee is my original work. The results submitted in this dissertation report have not been submitted for the award of any other Degree or Diploma.

Date: 24-06-2011

Place: ROORKEE

(Shashi Kant Pandey)

IDD ECW- V year
Enrolment # 061210
ECE Deptt.
IIT Roorkee

## CERTIFICATE

This is to certify that the statement made by the candidate is correct to the best of my knowledge and belief. This is to certify that this dissertation entitled, **"Real Time Detection and Classification of Subsurface Targets Using SFCW GPR,"** is an authentic record of candidate's own work carried out by him under my guidance and supervision. He has not submitted it for the award of any other degree.

Date:

Place:

(Dr. Dharmendra Singh)
Associate Professor,
ECE Deptt., IIT Roorkee

# ACKNOWLEDGEMENT

Carrying out this one year long work wouldn't have been possible with a single person's effort and I would like to thank all who have stood by me in carrying out this work.

I would like to extend my gratitude to my guide Dr. Dharmendra Singh for his constant encouragement, support and guidance. He would set doable but simultaneously challenging tasks before me which kept me motivated for the whole year.

I would like to thank the whole team of Remote Sensing Lab. I have really enjoyed the time spent with them. Special thanks are extended to Mr. Abhay N. Gaikwad, Mr. Rishi Prakas Shrivastava, Prashant Chaturvedi and Vishal Narain Saxena. There were times when I was stuck and discussions with them paved solutions.

I would like to thank Shravan without whom carrying out experimental work would have been a herculean task. He has dedicatedly given me his time so that I could conduct my experiments.

I am also thankful to my friends. Time spent with them after a day's work was always refreshing.

And above all my heartfelt gratitude is for my parents Shri Karuna Kant Pandey and Smt. Meera Pandey and sisters Aradhana and Vijayalakshmi. They have stood by me at each and every moment and made me believe in myself when I had doubts over it.

Shashi Kant Pandey

Roorkee

# ABSTRACT

This dissertation deals with application of Stepped Frequency Continuous Wave Ground Penetrating Radar for real time detection and classification of subsurface targets. Rohde and Schwarz provided FSH4 was used in Vector Network Analyzer mode and was interfaced with a computer to enable real time target detection and classification. A double ridged ultra wideband horn antenna (R&S HF 907) was used to transmit as well as receive EM waves.

Three targets- an air cavity, a metal sheet and a water bottle were buried at various depths under different volumetric moisture levels of soil. By the application of preprocessing techniques like Hamming Window Filtering, Median Filtering on A-Scan GPR data range profile was generated. ICA clutter removal technique was applied on B-Scan images generated by clubbing 30 A-Scans to look for probable presence of targets.

Thereafter, application of postprocessing techniques like back projection and Hough Transform was used to enhance target visibility and confirm the presence of targets at various depths and under various moisture levels of soil. Velocity correction was also applied to locate targets at exact depths they were buried at.

Once presence of targets was detected, energy density spectrum was generated for each location. This energy density spectrum was then used to classify the targets by the use of neural networks for pattern classification. Contextual masking for successive identification of targets was also used to bolster the classification ability of the system.

# ACRONYMS

| | |
|---|---|
| 1D | One Dimension |
| 2D | Two Dimensions |
| DUT | Device under Test |
| EDS | Energy Density Spectrum |
| FFT | Fast Fourier Transform |
| IFFT | Inverse Fourier Transform |
| SFCW | Stepped Frequency Continuous Wave |
| GPR | Ground Penetrating Radar |
| HPBW | Half power Beam Width |
| RADAR | Radio Detection and Ranging |
| RF | Radio Frequency |
| S | Scattering |
| SAR | Synthetic Aperture Radar |
| SVD | Singular Value Decomposition |
| ICA | Independent Component Analysis |
| PCA | Principal Component Analysis |
| UWB | Ultra Wide Band |
| VNA | Vector Network Analyzer |
| VSWR | Voltage Standing Wave Ratio |
| EM | Electro-magnetic |
| SNR | Signal to Noise Ratio |

# TABLE OF CONTENTS

# LIST OF FIGURES

# LIST OF TABLES

# Chapter 1. INTRODUCTION AND MOTIVATION

## 1.1. Introduction to GPR Technology

Ground-penetrating radar (GPR) is a geophysical method that uses radar pulses or waves to image the subsurface [1], [2]. It is the only non-invasive technique capable of accurately locating both metallic and non-metallic buried objects, without prior knowledge of their position. This non-destructive method uses electromagnetic radiation in the microwave band (UHF/VHF frequencies) of the radio spectrum, and detects the reflected signals from subsurface structures. GPR can be used in a variety of media, including rock, soil, ice, fresh water, pavements and structures. It can detect objects, changes in soil composition, and voids and cracks [2], [3].

However, GPR performance is sensitive to the depth of the buried targets, their dielectric coefficient, soil moisture etc. [4], [5]. Detectability of a target greatly depends upon its electric and magnetic properties contrast with respect to soil [3]. The performance of GPR system also depends on its parameters. For example, range of frequency of operation decides the resolution of the system. Transmitted power and sensitivity of the receiver determines the maximum penetration up to which presence of targets can be detected [4], [6]. And therefore, without any further research and development this technology will remain of little use.

GPR uses a transmitting antenna and a receiving antenna (bistatic mode of operation) or only one containing both functions (monostatic mode of operation) [1], [2]. The transmitting antenna radiates short pulses of high-frequency (usually polarized) radio waves into the ground. When the electromagnetic wave hits a buried object or a boundary with different dielectric constant, there is a sharp change observed in the received return signal strength because of the reflections at the boundary [1]–[4]. GPR uses these concepts of electromagnetic wave propagation to image and locate changes in electrical and magnetic properties in the ground. Detectability of a subsurface feature apart from its contrast in electrical and magnetic properties with soil also depends upon its geometrical shape [7]–[9]. For example a cylindrical object, though may have a great

contrast w.r.t soil as far as its electric and magnetic properties are concerned, it may not get detected at all because it reflects EM waves in different directions.

The electrical conductivity of the ground, the transmitted central frequency, and the radiated power limit the depth range of GPR [10], [11]. As conductivity increases, more electromagnetic energy is dissipated into heat, and hence, the penetration depth also decreases. Higher frequencies do not penetrate as far as lower frequencies, but give better resolution [12]. Penetration depth achieved by GPR system also depends upon the medium. Good penetration depth is achieved in sandy soils or massive dry materials such as granite, limestone and concrete where the depth of penetration has been reported up to 15 m. In moist and/or clay-laden soils and soils with high electrical conductivity such as sand near saline water resources penetration is only up to a few centimeters [13].

GPR has many applications in a number of fields [3], [4], [6], [10], [13]. It is used to study bedrock, soils, groundwater and ice in the Earth Sciences. In engineering field it is used for non-destructive testing of structures and pavements. It can be used to define landfills, contaminant plumes thereby having its application in environmental remediation. In archaeology it has been used for mapping archaeological features and cemeteries. It has military applications as well in the form of detection of landmines, unexploded ordnance and tunnels.

### 1.2. Problems in GPR

1. Non-linearity and unpredictability of the subsurface makes the modeling and computation of the subsurface parameters extremely difficult. This unpredictability leads to unexpected behaviour of radar response [6], [12], [13].
2. The subsurface keeps on changing in aspects like its dielectric constant, roughness, moisture content and texture. The GPR system needs to be accustomed to these changes [5].
3. Apart from the electrical and magnetic properties of a target its shape and size also has a great impact on GPR signal. For example a cylindrical object which may have a good contrast to the soil as far as its electric properties are concerned,

may not give strong reflections. The reason being that the reflected signals get directed in directions away from the antenna [7]–[9].

4. Different objects reflect the radar waves differently and these reflections also vary with depth. As the only information available with the receiver is the reflected wave, it cannot discriminate between reflections from a good reflector at greater depth and a bad reflector at a shallow depth [5], [8], [9].
5. Resolution issues are there for detection of shallow targets. Resolution is inversely proportional to operating bandwidth. For example, in this work, to get a resolution of 7.5 cm bandwidth was 2 GHz. Purchasing antennas having a constant gain over such a wide range is a costly affair. And a resolution of 7.5 cm means that a target which is less than 7.5 cm deep from the surface of the soil would not give a different reflection from the reflection due to air-soil interface [2], [11].
6. Various problems like clutter effects, antenna coupling, background noise make the detection of objects difficult. There are various signal processing techniques which otherwise give very good imaging resolution for example MUSIC algorithm. But sometimes reflections from weak dielectric materials are confused with noise and they don't get detected at all [14]–[17].
7. Also, if target identification is the problem at hand, depth-wise and soil moisture-wise variations of the received GPR signals hamper the algorithms used. Trained information is required for each object of different material at different depths and under different moisture level of the soil. Training GPR for all such variations is a very time consuming job [3], [5].
8. Real time data processing has limitation of computer memory and its processing speed. However, with the developments in VLSI this is no longer a very challenging problem and can be expected to be overcome soon.

### 1.3. Motivation

Ground Penetrating Radar (GPR) is an important remote sensing tool used to detect and localize the presence of subsurface targets. With its use in new areas, e.g. its use in landmine detection, it has become imperative to detect and image the buried targets in

real time. Real time detection is however, limited by the delay involved in data accumulation and data transfer and the memory limitations of processing softwares like MATLAB and LABVIEW. This long data acquisition time at each scan position depends upon two-way travel time for the EM signal to reach targets at a chosen maximum range, number of frequency points at which we seek the response of the ground (in case of SFCW GPR system) and the time for receiver to build up sufficient SNR. However, this delay won't matter a lot if we can successfully detect and identify subsurface targets. Moreover, with the advent of technology, faster processors are now available and total data acquisition is getting reduced. Primary focus of a research should be to detect all subsurface targets and to identify them.

There are various hurdles which make target detection and classification of targets difficult. For example cable-antenna reflections, antenna-air reflections, air-surface reflections are not information of our concern but strongest reflections are obtained at these interfaces. In a normalized B-Scan image, this makes the detection of low dielectric materials very difficult. Internal noise gets mixed up with reflected signals from targets and needs to be separated out. There are heterogeneities present in the soil itself which results in noise in the B-Scan images making it difficult to distinguish the presence of target in the soil. Solutions are required to address these problems. Therefore, study of imaging algorithms is required for SNR improvement of the image so that presence of targets can be detected.

After presence of targets has been detected, the next task is to classify targets. If we are trying to find one particular type of target, the rest of them are clutters for us. Their detection is like false alarm to use. In real time environment, false alarm means wastage of time on irrelevant data. Hence, study of target/clutter discrimination is a must if we have to make our system reliable.

It is these objectives which are the motivating factors for this work. Three targets were taken viz. an air cavity, a metal sheet and a water bottle. They were buried at different depths and under different moisture conditions of the soil. It was tried that GPR system detects the presence of all of them and classify them in real time.

## 1.4. Basic GPR Systems

There are three types of GPR systems classified on the basis of modulation schemes they employ. These are pulse radar, frequency modulated continuous wave radar (FMCW radar) and stepped frequency continuous wave radar (SFCW radar).

### 1.4.1. Time Domain Pulse Systems

Pulse radar consists of a single pulse of single frequency. The time duration of this pulse is in pico-seconds and the time gap between transmitted and received signal is used for range profiling. Measuring this time gap requires complex circuit and errors creep in while measuring this. Hence, it is not possible to calibrate the system response. Apart from this the power peak is very large and hence there is a need of distributing the power in order to reduce power losses and improve penetration depths. In pulse radar systems it is not possible to compensate the imperfections of RF electronics, antenna and feed system. Transmitting such a short duration pulse requires a very high speed ADC because of the need of instantaneous high bandwidth [18].

### 1.4.2. Frequency Modulated Continuous Wave Radar Technology

FMCW radar has a waveform where the frequency of the continuous wave is linearly changed from a minima to maxima. Typical sweep time of an FMCW radar changes from 1 to 100 ms giving a high pulse energy using a low transmitted power. As the time duration of the wave is large, the receiver has to start receiving the back-scattered signals while the transmitter is still transmitting. This results in problem in homodyning the transmitted and the received waveform [19], [20].

### 1.4.3. Stepped Frequency Continuous Wave Radar Technology

SFCW radar technology [2], [4], [6], [10], [11], [21] is comparatively the latest advent in radar field. Frequency-stepping is a modulation technique used to increase the total bandwidth of the radar. The SFCW radar obtains the distance to a target by measuring the coherent target reflections over $n$ number of stepped frequencies within the given bandwidth. '$n$' stepped frequencies are transmitted and the system response is noted over these frequencies. It is then converted into time domain by taking inverse FFT and this

time domain response when mapped on distance indexes gives the range profile at a certain point. The main advantage that SFCW offers over pulse systems are as follows:

1. It is capable to compensate the imperfections of RF electronics, antenna, and feed system through post processing of the collected data.
2. It is easier to generate a sinusoid of a given frequency than to measure the delay response as is done in time domain pulse systems. This delay response is in nanoseconds.
3. Stepped frequency microwave sources possess superior dynamic range and stability compared to pulse systems. They also permit control of frequency range, thus allowing an improvement in penetration performance.
4. In SFCW we get an increased dynamic range because of extremely narrow band filter used for receiving tones in spite of a lower peak transmittable power when compared to impulse one.

However, there are some disadvantages associated with SFCW over time domain pulse systems.

1. Increased system complexity and high component cost have discouraged its use in the past. However, as the cost of RF technologies is decreasing considerably, this no longer remains a problem.
2. Scanning a range of frequency in a stepped manner requires longer acquisition time. Hence, if target is moving it may become hard to detect it. Second real time systems won't be that fast if we go for this. However, this issue can be resolved by reducing the number of frequency steps.

It is because of the considerations of these pros and cons that SFCW radar was chosen for carrying out this work. In section 1.5 concepts of SFCW radar will be dealt with.

## 1.5. Concept of SFCW Radar

Stepped Frequency radar is similar to CW radar with the main exception concerning the fact that the frequency can be changed in discrete, highly repeatable and stable, steps to cover the desired bandwidth [22]. The phase and amplitude of the received tone is then

sampled and the equivalent time-domain sweep is reconstructed via Inverse Fast Fourier Transform. Figure 1.1 gives a block diagram of SFCW GPR.

### 1.5.1. System parameters for SFCW GPR

In SFCW radar the very first step involves choosing the frequency range of operation. If we go for higher frequency range we get better resolution but higher frequencies attenuate faster. Hence, a trade off has to be made. For this work frequency range of operation was chosen as 1 GHz to 3 GHz. Resolution also depends on bandwidth of operation [2], [10], [11]. However constraints are there to get a constant gain of antenna for the desired bandwidth. From the selected range of frequency it becomes clear that bandwidth was 2GHz. For the chosen bandwidth we select the number of frequency steps. More the number of frequency steps more would be the acquisition time. In this work number of frequency steps was 601. A stepped frequency waveform can be best approximated by Figure 1.2.

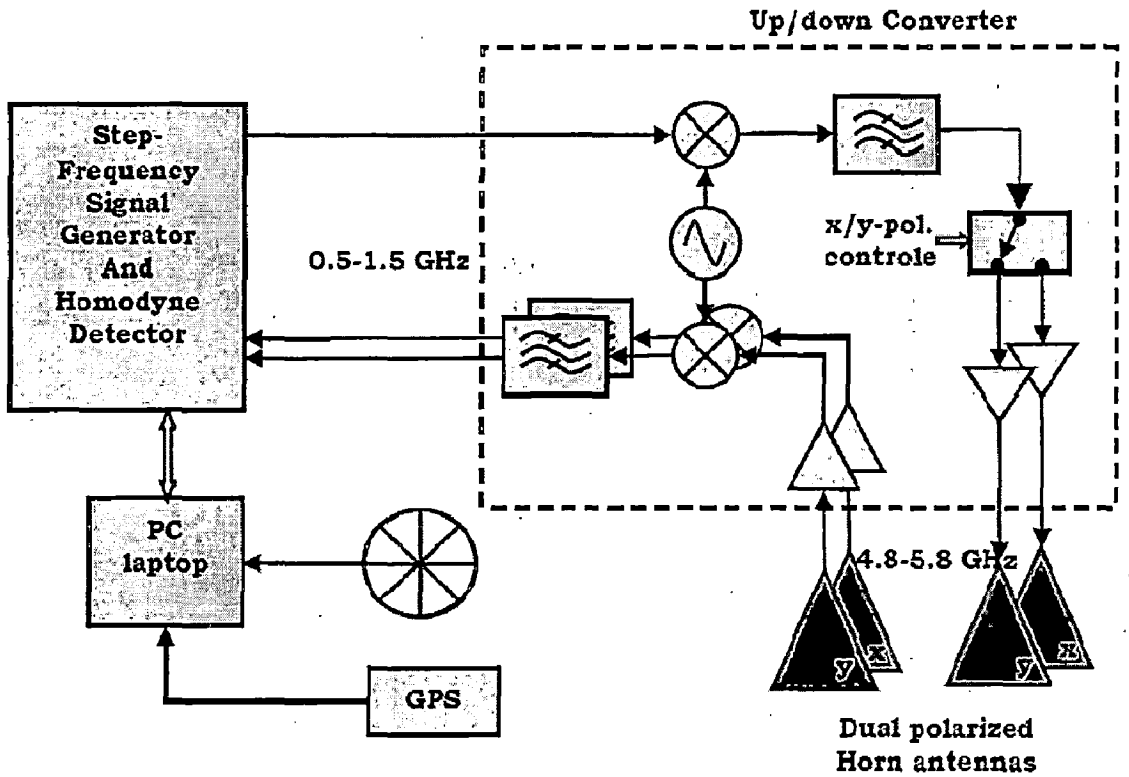


**Figure 1.1: A block diagram of SFCW GPR [10]**

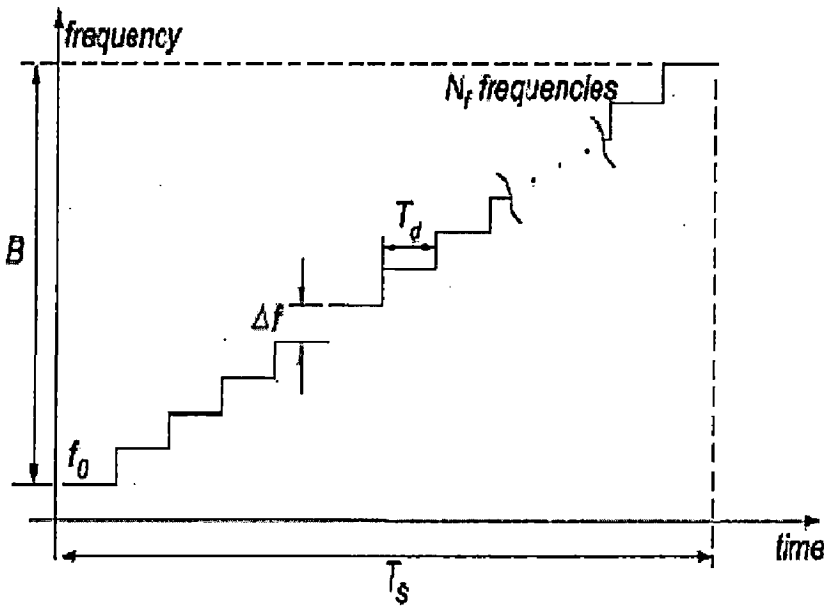


**Figure 1.2: A stepped frequency waveform [10]**

From the above figure it is clear that the frequency of $n^{th}$ pulse can be written as [13]:

$$f_n = f_o + n\,\Delta f \tag{1.1}$$

where, $f_o$ is the starting frequency and $\Delta f$ is the frequency step size. The frequency response measured by the SFCW radar is sampled in the frequency domain with a sampling interval $\Delta f$. If the reference signal for the $n^{th}$ pulse is [13]

$$A_1 \cos(2\pi(f_o + n\,\Delta f)t) \tag{1.2}$$

Then the reflected signal after a round trip delay of $2R/c$ can be represented as [13]

$$A_2 \cos(2\pi(f_o + n\,\Delta f)(t - 2R/c)) \tag{1.3}$$

Hence, the output of the phase detector can be modeled as the product of the received signal with the reference signal followed by a low pass filter. Consequently the $n^{th}$ phase difference comes out to be [13]

$$\varphi_n = 2\pi(f_o + n\,\Delta f)(t - 2R/c) \tag{1.4}$$

$$\varphi_n = \frac{4\pi f_o R}{c} + 2\pi\left(\frac{\Delta f}{T}\right)\left(\frac{2R}{c}\right)nT \tag{1.5}$$

In the above equation while the fist term is constant for a stationary target, the second term is depth dependent. That is, the range is converted into a frequency shift $f_s$ which is given as [13]

$$f_s = \left(\frac{\Delta f}{2}\right)\left(\frac{2R}{c}\right) \tag{1.6}$$

Now as from DFT, $\Delta f_s = 1/NT$, by differentiating both sides, we get the range resolution of the SFCW system as [13]

$$\Delta R = \frac{c}{2N\Delta f} \tag{1.7}$$

Where, $N\Delta f$ is equal to the system bandwidth. Hence, for the system used for this dissertation work resolution was 7.5 cm.

When the Nyquist sampling criterion for unambiguous reconstruction is applied

$$\frac{1}{\Delta f} \geq 2\tau_{max} \tag{1.8}$$

where, $\tau_{max}$is the maximum target delay in the synthesized time-domain response. If mixing is applied in the receiver, the baseband spectrum becomes single-sided, and the Nyquist sampling criterion reduces to

$$\frac{1}{\Delta f} \geq \tau_{max} \tag{1.9}$$

which gives the unambiguous range as [13]

$$R_{max} = \frac{c}{2\Delta f} \tag{1.10}$$

With bandwidth of 2 GHz and number of frequency steps 601, $\Delta f = 3.33\ MHz$ approx. Hence, unambiguous range, $R_{max} = 45\ m$. However, we will investigate till 1 $m$ only.

### 1.5.2. Signal Processing in SFCW Radar

Figure 1.3 gives the flowchart of the signal processing in SFCW radar [2], [4], [10], [11].

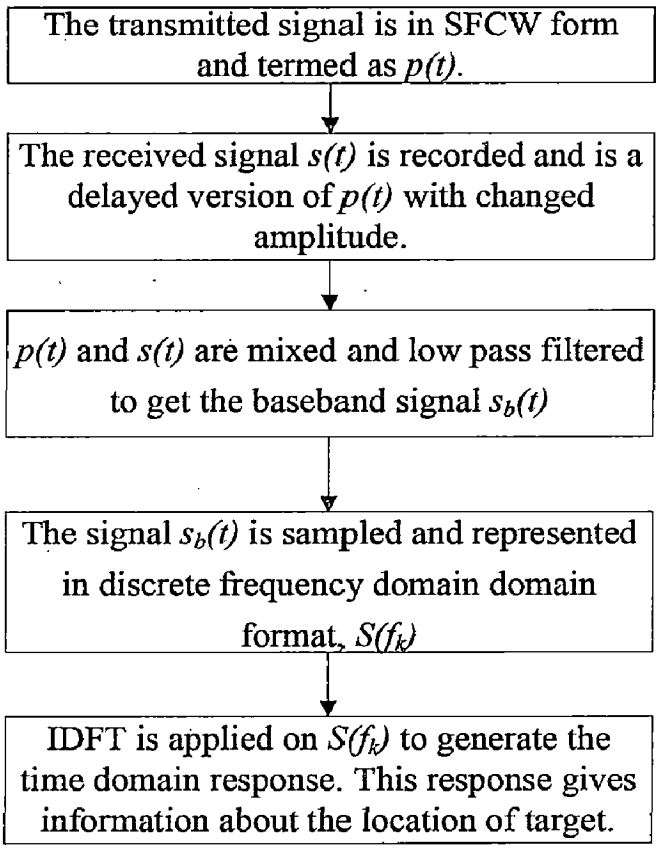


**Figure 1.3: Signal processing in SFCW radar**

A detailed explanation of the steps involved in signal processing in SFCW radar is as follows:

1. The SFCW signal $p(t)$ is mathematically represented by [13]:

$$p(t) = \sum_{i=0}^{N_f-1} \exp(j2\pi(f_0 + i\Delta f)t) \,.\, rect\left(\frac{\left(t - \frac{T_d}{2}\right)}{\frac{(2 - iT_d)}{T_d}}\right) \tag{1.11}$$

   where the dwell time $T_d$ represents the time spent on each frequency. The duration of the whole waveform, the scan time $T_s = N_f T_d$.

2. Assuming that the radar signal is reflected from a single scatterer having a frequency independent reflection coefficient $\Gamma$. The reflected signal $s(t)$ can be written as a delayed version of the transmitted signal multiplied by the reflection coefficient.

$$s(t) = \sum_{i=0}^{N_f-1} \Gamma \exp(j2\pi(f_0 + i\Delta f)(t - \tau)) . rect\left( \frac{\left(t - \frac{T_d}{2}\right)}{\frac{(2 - iT_d - \tau)}{T_d}} \right) \quad (1.12)$$

3. After homodyning in the quadrature mixer and low-pass filtering, the received echo becomes a complex baseband signal [13]

$$s_b(t) = \sum_{i=0}^{N_f-1} \Gamma \exp(j2\pi(f_0 + i\Delta f)\tau) . rect\left( \frac{\left(t - \frac{T_d}{2}\right)}{\frac{(2 - iT_d)}{T_d}} \right) \quad (1.13)$$

The baseband signal is now a staircased sine wave where each step corresponds to the response measured at each frequency. The amplitude and the phase is determined by the reflection coefficient of the target while the frequency of the sine wave is proportional to the delay $\tau$.

4. If the signal is sampled in the middle of each step, we get a complex array [13]

$$s[k] = \Gamma \exp(-2\pi(f_o + k\Delta f)\tau), k = 0,1,2 \ldots, N_f - 1 \quad (1.14)$$

which can also be written as:

$$S(f_k) = \Gamma \exp(-2\pi f_k \tau) \quad (1.15)$$

5. Taking IDFT of 1.15 can give us the synthesized time-domain response

$$\hat{s}(t) = IDFT\{S(f_k)\} \quad (1.16)$$

Hence, by observing the amplitude of the reflected wave we can know the reflection coefficient of the target and by observing the phase delay in the reflected wave we can deduce the location of the target.

Antenna is positioned at a location and its range profile is generated by observing the frequency domain response of the SFCW radar at that point. Generating downrange profile at a particular location of our interest is called A-Scan. If antenna is moved along a particular direction we will get a 2-D image which can give us information about the depth and the length of the target in azimuth direction which is the direction along which antenna is moved. This scanning along a particular direction is called B-Scan. If several B-Scans, each parallel to each others, are done we get a C-Scan image. C-Scan is generated at a particular depth and gives the cross-range and azimuth-range of the target at that depth [22]–[24].

However, there is some unwanted information in this time domain response which needs to be eliminated by further pre-processing and post-processing. For example, as signal enters antenna from the coaxial cable there is a change of medium and the range profile will give reflection at that point. This information is unwanted and needs to be eliminated. Similarly antenna-air reflection is not of our concern and needs to be eliminated. How these are eliminated has been explained in Chapter 3.

There are clutter effects from various noise and disturbance sources which interfere in the correct detection and location of the target in question. This noise can be taken care of by the use of frequency domain filtering which will also be explained later in Chapter 3.

## 1.6. Objective

Considering the motivation to this work, following objectives were set:

1. Study and implementation of various imaging techniques so that subsurface targets could be detected at various depths and under various moisture levels of the soil in real time. In this case those subsurface targets were air cavity, metal sheet and water bottle.
2. Study and implementation of various classification techniques so that these targets viz. air cavity, metal sheet and water bottle could be classified after their presence has been detected in real time.

## 1.7. Dissertation Overview

This work is organized as follows.

Chapter 1 deals with introduction to GPR technology and problems faced in implementation of GPR system for target detection or classification. Hard terrains pose greatest challenge to this technology as sometimes EM waves fail to penetrate the ground and sometimes clutters become irresolvable. Basic types of GPR systems have been discussed and it has been discussed why SFCW radar system has been preferred over time domain pulse system and frequency modulated continuous wave radar systems. This is followed by an introduction to SFCW parameters. This chapter ends with motivation and objectives set to carry out this work.

Chapter 2 deals with brief review of the works done in the past in this field. How system performance has been improved and what are the conditions where work still needs to be done to enhance the system performance have been discussed in brief. Imaging methods adopted by various researchers have been reviewed to choose the one that suits our needs. This chapter also gives a brief account of various methods for target detection and target classification as used in the past.

Chapter 3 deals with methodology employed to solve the problem. It starts with the experimental arrangement used to take readings. Then it deals with data collection methodology where it deals with VNA calibration, time gating, A-Scan readings and then B-Scan readings. Chapter 3 also deals with data processing algorithms used to identify and classify subsurface targets. In the end this chapter concludes with a model development which is a flowchart to guide how real time data collection is to be done and how target detection and classification is to be done using this data.

Chapter 4 has implementation, results and discussions of the work of the experimental work done. It gives information about the results obtained in various conditions that were set for this experimental work. It also explains the reasons for results so obtained. Results have been given for the effect of preprocessing and post-processing techniques on the GPR data. Imaging results are there which show how target is detected. Target

classification results are there to show the effectiveness of each method so used for the same.

In the end Chapter 6 gives the concluding remarks and the work that still remains to be done to improve the system performance.

# Chapter 2. BRIEF REVIEW

Considering the volume of research going on in GPR, we can say that it is a very dynamic field of study. Research has been going on in the fields of Improving SFCW GPR Performance, GPR imaging, subsurface target detection using GPR and GPR target classification. This chapter has been divided into four sections to enhance the understandability of research going on in this field.

## 2.1. Improving SFCW GPR Performance

Probably one of the landmark researches to explain the working of SFCW GPR has been done by Parrini et al. [1]. They have designed a GPR system for detection of buried objects in historical sites by the use of range profiling using A-Scans at various locations. They have emphasized on the need of background subtraction for successful peak generation. Their GPR system uses Digital Direct Synthesizer (DDS), a Phase Lock Loop (PLL) and a Quadrature Modulator (I/Q Modulator) and works in L-S band of frequency. Their system does this commendable job of explaining how SFCW GPR generates the signal and how signal processing is done.

To address the large data acquisition time Gurbuz et al. [25] have proposed compressive sensing for data acquisition and imaging method for SFCW-GPRs. They have exploited the fact that the target space is sparse and it is sufficient to observe readings at a small number of random frequencies to construct an image of the target space. Though, this reduces the data acquisition time, causes higher computational costs. The imaging results with experimental GPR data have exhibited less clutter than the standard migration methods and are robust to noise and random spatial sampling. There method has improved the resolution also as the closely spaced targets which cannot be resolved by standard migration methods have been shown to be resolved here.

Tremendous work has been done to improve the time domain response of the SFCW GPR signal. Kong et al. [14] have proposed a sidelobe suppression algorithm via the reiterative minimum mean-square error strategy, where a minimum mean-square error filter has been designed for each range cell. Their work addresses the inherent problem of conventional method of taking IFFT to generate range profile which is the masking of

small targets by large nearby targets owing to the high range sidelobes that result from IFFT. They have made use of Minimum Mean Square Error (MMSE) filter to produce refined estimates of range profile and power of each range cell. In this direction similar works have been done by Genderen and Nicolaescu [15] in their Imaging of Stepped Frequency Continuous Wave GPR data using the Yule- Walker parametric method and by Luo et al.[26] in their work on sidelobe suppression method based on adaptive pulse compression (APC) for random stepped frequency radar. Random stepped frequency radar chooses the transmitted frequencies randomly, which helps suppress range ambiguities but with increased side lobe levels of random noise. In their work Luo et al. have used APC to suppress these sidelobes. Muqaibel et al. [27] have made use of Hamming window to separate noise from signal due to target in frequency domain. Their results show that noise has been suppressed in the range profile after Hamming window has been applied in frequency domain.

Rappaport [5] has based his study on the effect of moisture on subsurface detection. His studies have brought forth the fact that poor target/soil contrast makes detection of non-metallic mines difficult. Greater soil moisture implies higher dielectric constant, which in turn increases contrast and scattering of radar waves. But simultaneously this also increases the contrast between the air and the soil, increasing clutter. And as signal attenuates faster in moist soil, detection of target becomes tougher.

Langman and Inggs [4] have worked on 1-2 GHz SFCW radar for landmine detection and have emphasized on the issues that need to be taken care of while processing GPR data. They have called for the need to accustom the GPR system to changes in the dielectric behaviour, roughness, moisture content and texture of the medium.

### 2.2. GPR Imaging

Range profile as generated by A-Scan doesn't reliably give the exact location of subsurface targets. And often low dielectric materials go unnoticed in a single scan. To counter these imaging has to be to done. Various methods have been proposed by various researchers from time to time. Morrow and Genderen [7] in their work on Effective Imaging of Buried Dielectric Objects have proposed Synthetic Aperture Technique for

imaging of materials having poor target/soil contrast. They have used conventional preprocessing measures employed in frequency domain to expose weak scatterers and enhance radar image. These methods include average background removal, analytic window functions such as Blackman-Harris or complex cepstrum window of either minimum or maximum phase. They have also relied on reflected signal strength to calculate dielectric permittivity of the material and later on have used this to classify targets. Ozdemir and Ling [8] have applied a Fourier based imaging algorithm based on SAR concepts to image high permittivity (bottled water) and low permittivity (plastic) dielectric objects. In their coherent imaging algorithm they have used many spatial points to provide sufficient SNR to their 3D GPR images. Panzner et al. [9] have studied radar signatures of complex buried objects in ground penetrating radar to produce SAR focussed radar scan of H-shaped, E-shaped and complex zigzag polystyrene objects. They have passed the measured raw data through Gaussian Pulse Shaper followed by a carrier remover. After this they have passed it through SAR processor and have taken IFFT of the resultant data to produce those radar scans.

To counter internal noise in GPR system Shrestha et al. [16] have made use of a combination of MUSIC (Multiple Signal Classification) and FFT (Fast Fourier Transform) to produce high resolution images. But this technique requires high precision in measured receiving signal level ratio and measuring device. The main disadvantage of using MUSIC is that often reflections from low dielectric materials, which are only a bit stronger than noise, may get confused with noise and hence may get eliminated.

For clutter removal and noise suppression various researchers have done tremendous work. Zhao et al. [17] have applied Karhunen-Lo´eve Transform (KLT) to improve the signal-to-noise ratio of the GPR data. For the GPR data set they have found its covariance matrix and then the eigenvalue matrix of this covariance matrix. Clutter due to air-soil interface will be the most correlated element among traces and hence it will have corresponding to it the eigen-vector corresponding to highest eigenvalue. Similarly, the random noise is most uncorrelated from trace to trace and will be represented by lowest eigenvalues. Intermediate eigenvalue are of our concern and eigenvectors corresponding to them are used to generate B-Scan images. Liu and Leung [28] have used chaos

modulation to suppress clutter. A chaotic waveform generated by using Chebyshev map is multiplied by Gaussian pulse waveform and is transmitted. They have observed that this improves the range resolution and solves the problem of clutter better. In a similar fashion, Dobrotin and Leitas [29] have used inverse filtration. Using SVD for clutter removal Verma et al. [24] have found in their work that SVD-clutter removal technique works better when compared to ICA or PCA to remove the clutter and detect the target for UWB through wall imaging. The use of Independent Component Analysis for GPR Signal Processing has been explored by Zhao et al.[30] Delac et al. [31] in their Comparative Study of PCA, ICA and LDA have pointed out that ICA minimizes both second-order and higher-order dependencies in the input data and attempts to find the basis along which the data (when projected onto them) are statistically independent. They have used FERET database and used various combinations of PCA, ICA and LDA for face recognition. They have found that ICA is a good choice to combat temporal changes in data. Aapo Hyvärinen [32] in his Fast and Robust Fixed-Point Algorithms for Independent Component Analysis has given a fixed point algorithm which is fast at convergence making implementation of ICA computationally fast.

For imaging back projection has been used widely. It is based on the simple fact that range profile generated after an A-Scan doesn't show only those targets which lie along the perpendicular drawn from the ground surface and passing through the antenna. That range profile has reflections due to all the targets that are covered by the swath of the antenna. Cui et al. [33] have used back projection algorithm to SFCW through wall imaging by analyzing the time-domain back-projection algorithm and the stepped frequency imaging. Morrow and Genderen [7] have also used UWB synthetic aperture technique (SAT) that employs selective frequency space filtering and then back projection in their Effective Imaging of Buried Dielectric Objects. Zhou and Su [34] have proposed an algorithm called Multiply Back Projection (MBP) which is similar to the conventional back projection with the addition of pairing multiplication procedure. They have claimed that their algorithm suppresses artifacts in the imaging results, though at the cost of more number of computations involved. Lei et al. [35] have come with TAM-BP algorithm for GPR application. In this algorithm they have accounted for time

delay occurring due to the dielectric constant of soil to improve the image quality. However, computational complexity remains with their method as well.

To counter discontinuities in B-Scan images methods like column filtering and interpolation have been used. Zhang [36] has discussed column filtering approach in his paper on optimizing building detection in satellite images using texture filtering. Interpolation is another image processing technique to smoothen the image. Various interpolation techniques have been discussed by Teoh et al. in their paper [37]. To remove random noise in the GPR images thresholding has been applied by Chandra [23] in his dissertation work on study of through wall imaging in UWB range for target detection. Out of Otsu thresholding and mean deviation based thresholding he has preferred mean deviation based thresholding for its computational efficiency.

### 2.3. GPR Target Detection

A great volume of work has been done to detect targets in the images so obtained after GPR imaging. Yigit et al. [38] have presented an overview on the imaging aspects of GPR. Using standard C-Scan they have detected the presence of multiple targets buried in a sand pit. And then by using ω-k SAR focusing technique they have bettered the image so obtained. Similarly they have also detected the water leakage from a pipe as leakage increases the conductivity of the sand and EM wave could not penetrate into this saturated region due to high conductivity of the mud. Liu et al. [39] have applied Hyperbola Fitting after various pre-processing techniques like elimination of ground-surface echo, normalization, background subtraction, edge-detection using Sobel operator and hyperbola edge thinning to detect the presence of multiple targets. In a similar fashion Pasolli et al. [40] have applied unsupervised Genetic Algorithm (GA) to detect the presence of multiple targets by finding hyperbolas in edge-detected binary GPR image. They have iteratively called GA to search best hyperbola in the binary image till all the objects have been found. In the genetic optimizer, each chromosome models the apex position and the curvature associated with the candidate pattern, while the fitness function expresses the Hamming Distance between the pattern and the binary image content. Having detected all the targets they have used Support Vector Machine classifier

to identify those targets based on the dielectric behaviour of the object. They have also estimated the size of the targets using Gaussian process regression approach.

Statistical measures of noise and targets have also been used for target detection in Through Wall Imaging by Debes et al. [41] They have found a general probability density function of target and that of noise by observing pixel values corresponding to target and noise in B-Scan image generated for different heights of scan. Hypothesis testing has then been used for unsupervised target detection.

Al-Nuaimy et al. [42] have made use of neural networks and pattern classification for automatic detection of buried utilities and solid objects with GPR. The use of neural networks for pattern classification gives them a high resolution image of the shallow subsurface in a highly reduced computational time. The neural network in their work makes use of the spectral features of the data to identify areas in the radargram containing useful reflections. Thereafter they have applied the Hough Transform as a pattern recognition technique to locate and identify the hyperbolic anomalies associated with buried targets. Thus, they have successfully generated high resolution images suitable for precise location and mapping of subsurface utilities and ordnance.

## 2.4. GPR Target Classification

The most challenging aspect in GPR is to classify the targets that have been detected. Ability to classify targets reduces false alarms in real time environment. Ho et al. [43] have used spectral characteristics from GPR data to discriminate between landmine and clutter. They have exploited the fact that landmine targets and clutter objects often have different shapes and/or composition, yielding different energy density spectrum (EDS) that may be exploited for their discrimination. They have calculated the metric correlation coefficient of the frequency domain spectra for GPR data and based on the value so obtained have distinguished landmine from target. Gader et al. [44] have made use of depth wise whitening to extract features of landmines and clutters to differentiate them. They have computed a single depth wise Constant False Alarm Rate (CFAR) for anomaly detection on the depth dependent adaptively whitened data.

For target classification Daniels et al. [45] have relied on RMS errors of the difference of normalized autocorrelation coefficients and normalized FFT between reference targets and test targets. They have postulated that a better way for classification would be multiplication of the two RMS errors. They have also made use of Pearson's Correlation Coefficient for target classification. Using these they have differentiated several prototypes of landmines from coke can, bottle and pipe. Also, they have discouraged the use of correlation vectors such as variance, skewness and kurtosis of autocorrelation functions of the targets for their discrimination as these didn't yield better results.

Santos et al.[46] have made use of neural networks for pattern classification of metallic and non-metallic targets using GPR reflections in a test site in Brazil. For the test targets they extracted three parameters. First was the normalized arithmetic mean of the maximum amplitude from range profiles obtained after A-Scans. The second feature was its respective normalized standard deviation and the third feature was the depth of the target in order to account for the amplitude variation due to depth. They have trained a three layer neural network for pattern classification to classify targets into metallic and non-metallic targets.

Time frequency signatures have also been used for target classification by various researchers. Strifors et al. [47] have used fuzzy-cluster representation of time frequency signatures as a means for automatic classification of buried mine-like targets. They have used pseudo-Wigner distribution to extract time-frequency domain target signatures and later on have used fuzzy method to classify the targets. In a similar fashion Sun and Li [48] have also used time-frequency analysis for plastic landmine detection. They have compared Wigner-Ville distribution (WVD) and Choi-Williams distribution (CWD) methods of producing time-frequency signatures of the targets and as WVD suffers from cross-term interference problem they have gone for CWD. Later on they have used Principal Component Analysis for signature classification. In addition to the satisfactory results which they appeal to have arrived at, they also maintain that time-frequency pattern is highly non-stationary for clutters as well as landmines making the implementation of conventional detection designs very difficult.

In an attempt to classify targets, Sugak and Sugak [49] have studied the phase structure of signals with respect to GPR measurement and its sensitivity to the change of electrical properties of soil. They are hopeful that their study can be used for determination of physical properties of soil and of targets and hence targets can be classified using this phase information. They have used Chebyshev windowing DFT instead of the conventional method to find IDFT which gives them more informative phase spectrum estimation.

Based on the reflected signal strength of various targets Jain [22] has distinguished three targets – a metal sheet, a water bottle and an air cavity in sandy soil and controlled laboratory environment in his dissertation work. He has used contextual masking and successive identification of targets to classify these targets. This was preceded by his rigorous study of normalized reflected signal strength of these targets at different depths under different moisture conditions of sand. By contextual masking he could get the normalized reflected signal strength of the next target and could identify it.

# Chapter 3. METHODOLOGY

The aim of this work was to detect and classify subsurface targets in real time. To achieve these four things were essential -

- to assemble an experimental setup which is capable of data acquisition and data processing in real time.
- to set parameters of this experimental setup so that target features can be extracted for different burial depths of targets and for different moisture levels of soil.
- to decide how data is to be collected so that useful information can be extracted.
- to choose data processing algorithms which can be useful to extract information out of GPR data so that targets can be detected and classified.

This chapter deals with the same aspects of conducting the experiments. Section 3.1 gives the details of experimental setup and system parameters. Section 3.2 enunciates data collection methodology and section 3.3 gives an account of data processing algorithms used for target detection and classification.

## 3.1. Experimental Setup

With the knowledge of SFCW radar and latest researches that have been done in GPR, which have been dealt with in Chapter 1 and Chapter 2 respectively, experimental setup was designed to take GPR readings.

Choosing system parameters was based on conditions in which experiment was carried out. The very first step was choosing the frequency range of operation. As it has been discussed before that M/W signals at higher frequencies though offer better resolution, attenuate faster. The antenna that was used for carrying out the work was lightweight double ridged ultrawideband horn antenna. The antenna used (R&S HF-906) works in the range of 1 GHz to 18 GHz. The VNA available (R&S FSH 4) works in the range of 100 kHz to 3.6 GHz. Hence, keeping these in mind, the lower limit of frequency of operation was set as 1 GHz and the upper limit was set as 3 GHz. This 2 GHz of bandwidth offered a range resolution of 7.5 cm. No. of scanning points in this frequency range was set as

601. Also, to get maximum penetration depth, the tracking generator attenuation of the VNA was set at 0 dB and hence, the transmitted power by VNA was 1 mW.

An indigenous system was designed to collect and process GPR readings in real time. Following sections explain the experimental set up and data collection methodology used to carry out this research work.

### 3.1.1. Experimental Arrangement

To enable real time processing of data, a vector network analyzer (R&S FSH 4) was connected to a PC using LAN. This offered real time target detection and identification. NI VISA 4.5 and VXI Plug`n`Play, provided by Rohde and Schwarz were used to connect the laptop with FSH4. The development environment was MATLAB 2009b provided by MATHWORKS. The Vector Network Analyzer gave reflection values at different frequency steps between the chosen range of frequency of operation through a double ridged ultrawideband horn antenna (R&S HF-906). Section 3.1.3 and section 3.1.4 explain the details of the VNA and the antenna. Schematic of the experimental setup and an image of actual connection have been shown in the Figure 3.1. Experimental parameters have been summarized in Table 3.1.

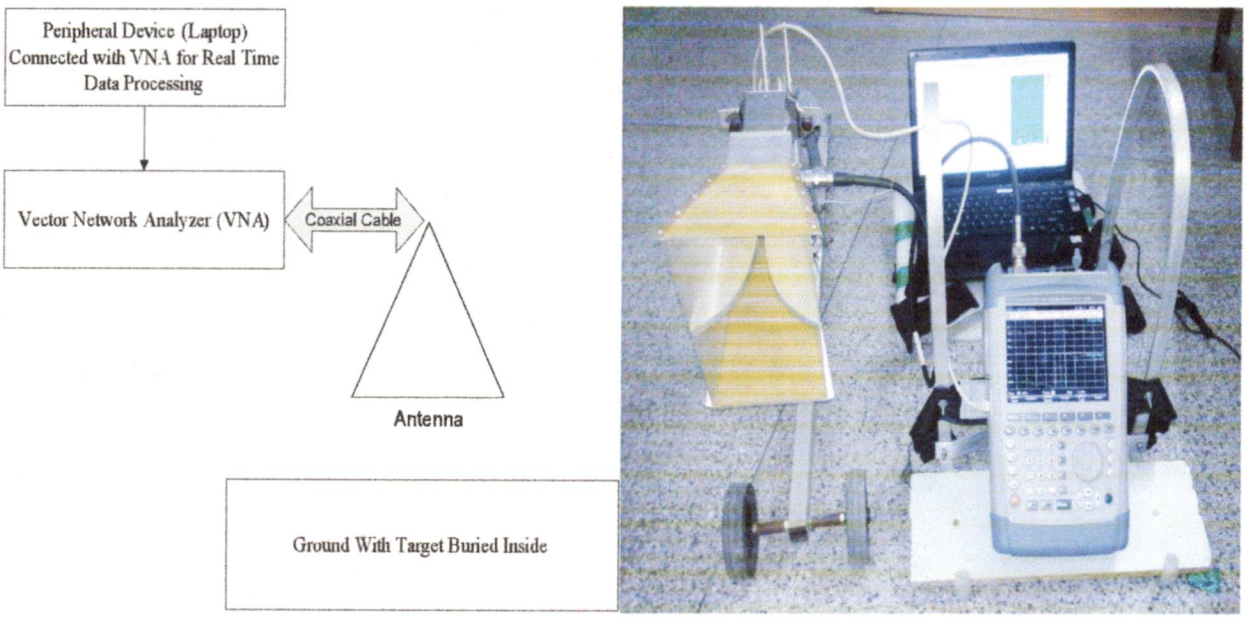


**Figure 3.1: (a) Block diagram from data collection set up, (b) Actual image of data collection set up**

**Table 3.1: System parameters for conducting experiments**

| | |
|---|---|
| Antenna | Double-ridged waveguide type (HF 906) |
| Vector Network Analyzer | R&S FSH4 |
| VNA Power | 1 mW (at tracking generator attenuation=0 dB) |
| Cable Loss (for 2 m length) | 1-1.5 dB |
| Frequency Range for Operation | 1 GHz to 3 GHz |
| $\Delta f_o$ | 3.33 MHz |
| No. of frequency points | 601 |
| Range resolution | 7.5 cm |
| Unambiguous range | 45 m |
| Investigated range | 1 m |

### 3.1.2. Targets and Soil Conditions

Three targets- an air cavity, a metal sheet and a water bottle- were taken as targets for carrying out the experiments and were buried at different depths under different moisture conditions. The targets were buried in soil having lots of clutters in the form of gravels at different depths and under various moisture level of the soil. Several B-Scans each consisting of 30 A-Scans were done to detect their presence in the soil and later on to classify them. As it has been discussed earlier that the detectability of a subsurface feature depends upon the contrast in electrical and magnetic properties, and its geometric relationship with the antenna, the values of S11 depend on the difference of dielectric constant of the medium and the target. The images of the targets have been shown in Figure 3.2 and their properties have been summarized in Table 3.2.

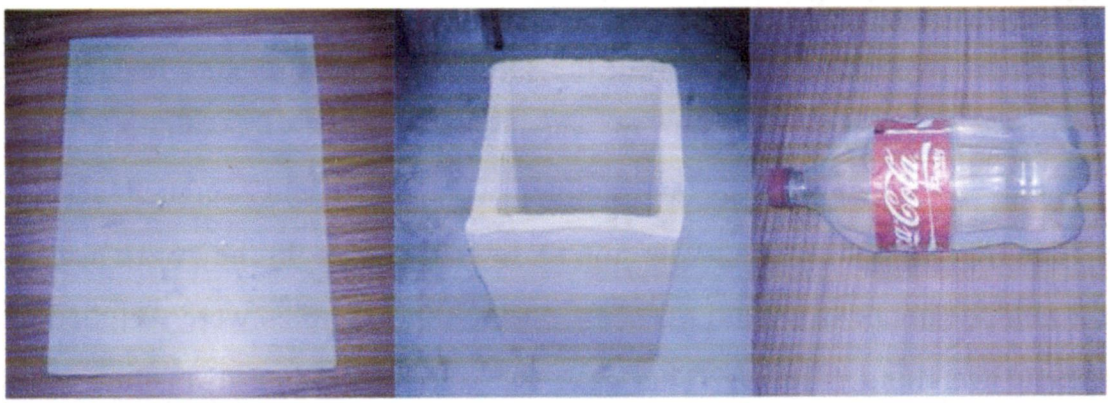

(a) A Metal Sheet (b) An Air Cavity (c)A Water Bottle

**Figure 3.2: Targets taken for carrying out experiments**

**Table 3.2: Properties of targets used for experiments**

| Target Type | Target Size | Dielectric Constant |
|---|---|---|
| Air Cavity | 30 cm by 18 cm by 18 cm | 1 |
| Metal Sheet | 25 cm by 25 cm | ∞ |
| Water Bottle | 30 cm, diameter 10 cm | 80 |

An area of 2 meters by 1.5 meters was cleared and targets were buried in it at several depths under different moisture conditions. Moisture content of the soil was increased by adding water in a controlled fashion to study the effect of moisture on GPR signals received. Figure 3.3 shows the picture of the ground cleared to conduct experiments. The antenna was mounted on a moving device so that it can slide in transverse direction above ground. The transmitted signal is stepped from 1 GHz to 3 GHz in 601 steps.

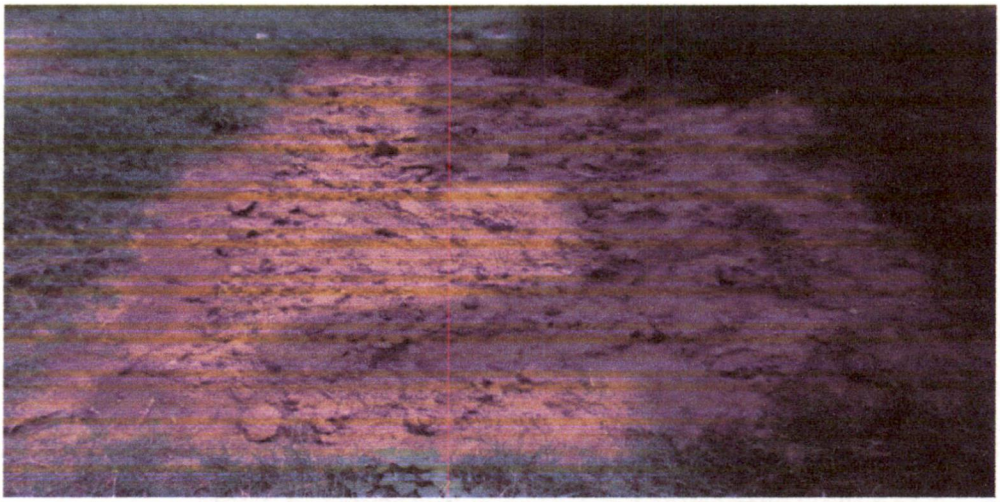

**Figure 3.3: Ground area cleared to conduct experimetnts**

To measure the dielectric constant of the soil at different moisture levels volumetric soil moisture i.e. the ratio of volume of water in soil sample to volume of soil has to be calculated. To measure this, soil samples were taken and weighed accurately on an electronic weighing machine. After noting down their weight they were heated in an oven for around 12 hours at around 80°C after which the samples were weighed again on the electronic weighing machine. This gave the weight lost due to heating and hence, the weight of water in the soil sample taken. Percentage of water by weight in the soil samples when multiplied by 1.6 gave volumetric measure of soil moisture $m_v$. Following equation gives the method to calculate volumetric soil moisture.

$$m_v = 1.6\left(\frac{W_{before\_heating} - W_{after\_heating}}{W_{before\_heating}}\right) \quad (3.1)$$

The effect of moisture on the real part of dielectric constant of soil can be computed as following [50]:

$$\varepsilon' = 3.03 + 9.3m_v + 146m_v^2 - 76.7m_v^3 \quad (3.2)$$

At different volumetric measures of soil moisture the dielectric constants of the soil as obtained have been summarized in the Table 3.3.

**Table 3.3: Dielectric constant of soil at different volumetric measures of soil moisture**

| Moisture Content | Dielectric Constant of the Soil | Depths of insertion of air cavity, metal sheet and water bottle in the soil surface |
|---|---|---|
| 7.5 % | 4.52 | 10 cm, 15 cm, 20 cm |
| 15.5 % | 7.70 | 10 cm, 15 cm, 20 cm |
| 20.5 % | 10.41 | 10 cm, 15 cm, 20 cm |

### 3.1.3. Vector Network Analyzer (VNA)

A Vector Network Analyzer is used to measure the S-parameters which are the transmission and reflection coefficients for the device under test. These S-parameters contain both amplitude and phase information about the device under test. In SFCW monostatic GPR mode S11 values at different frequency steps in given bandwidth are observed. The reflection coefficient (S11) is the ratio of the reflected signal voltage level to the incident signal voltage level.

The vector network analyzer used for carrying out this dissertation work is Rhode and Schwarz VNA (R&S FSH 4 (100 kHz to 3.6 GHz)). The analyzer transmits a stimulus signal to the input port of the device under test (DUT) and measures the reflected wave. For this dissertation work VNA was used to generate frequencies in the range of 1 GHz to 3 GHz. This SFCW wave was divided in 601 points. VNA specifications have been summarized in Table 3.4.

**Table 3.4: VNA Specifications [51]**

| | |
|---|---|
| Data Points | 601 |
| Output Port Power | nominal 1 mW (at tracking generator attenuation=0) to –40 |
| Result Formats | Magnitude (dB), phase, magnitude (dB) + phase |
| Connector | N-Female, 50 Ω |
| Calibration Standard | R&S®FSH-Z28 Combined Open/Short/50 Ω Load |
| Operating Bandwidth | 1 GHz to 3 GHz |

### 3.1.4. Antenna

The antenna used in this works was Rohde and Schwarz HF 906 double ridged waveguide horn antenna HF 906 with linear polarization, which is a broadband compact transmitting and receiving antenna for the frequency range 1GHz to 18 GHz. The RF connector is N Female and the nominal impedance is 50 Ω. The gain of the antenna is 8 to 10 dbi for 1 to 3 GHz operating range of frequency. For this frequency range half power beamwidths in E-plane and H-plane are $80^{\circ}$ and $100^{\circ}$ respectively for the antenna. Antenna specifications have been summarized in Table 3.5. VSWR of antenna for frequency range 1 GHz to 3 GHz is given in Figure 3.4.

**Table 3.5: Antenna Specifications [52]**

| | |
|---|---|
| Frequency range | 1 GHz to 18 GHz |
| polarization | Linear |
| RF connector | N female |
| Nominal impedance | 50 Ω |
| Gain (for 1 GHz to 3 GHz) | 8 dBi to 10 dBi |
| VSWR (for 1 GHz to 3GHz) | < 2.5 |
| HPBW at 1 GHz in E-Plane | $80^{\circ}$ |
| HPBW at 1 GHz in H-Place | $100^{\circ}$ |
| Max. RF input power | 300 W CW , 500 W PEAK |
| Max . height | 160 mm |
| Max . width | 250 mm |
| Max . length | 290 mm |
| Weight | 1.5 kg |

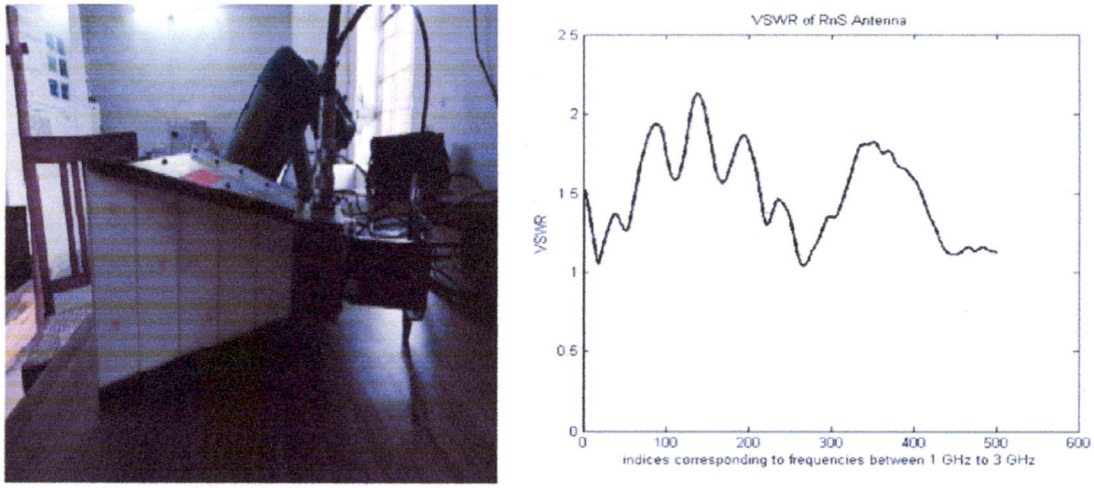


(a) R&S HF 906,Double Ridged Horn Antenna

(b) VSWR of HF-906 between 1 GHz to 3 GHz

**Figure 3.4: HF 906 double ridged horn antenna and it s VSWR from 1 GHz to 3 GHz**

The swath, $\Delta$ at the investigated depth $d$ from the antenna is given by:

$$\Delta = \pi ab \tag{3.3}$$

Where $a$ is semi-major axis and $b$ is the semi-minor axis of the ellipse. The values of $a$ and $b$ are calculated by equations given below:

$$a = d \tan\frac{\theta_a}{2} \tag{3.4}$$

$$b = d \tan\frac{\theta_b}{2} \tag{3.5}$$

Therefore,

$$\Delta = \pi d^2 \tan\frac{\theta_a}{2}\tan\frac{\theta_b}{2} \tag{3.6}$$

As $\theta_a = 80^\circ$ and $\theta_b = 100^\circ$ for HF906 antenna, at investigated depths as measured from antenna flare swath area are 1963.49 $cm^2$ for $d$=25 cm, 2827.43 $cm^2$ for $d$ = 30 cm and 3848.45 $cm^2$ for $d$=35 cm.

## 3.2. Data Collection

### 3.2.1. VNA Calibration

Calibration is the process of eliminating systematic, reproducible errors from the measurement results. Calibration plays an important role in determining the accuracy of the measurement system. The process involves the following stages:

1. A set of calibration standards is selected and measured over the required sweep range.

2. The analyzer compares the measurement data of the standards with their known, ideal response. The difference is used to calculate the system errors using a particular error model (calibration type) and derive a set of system error correction data.

3. The system error correction data is used to correct the measurement results of a DUT that is measured instead of the standards.

Since, we have to use S11 parameter only; full one port calibration of FSH4 was carried out by R&S®FSH-Z28 Combined Open/Short/50 Ω Load kit. The three standard measurements are used to derive all three reflection error terms:

- The short and open standards are used to derive the source match and the reflection tracking error terms.

- The match standard is used to derive the directivity error.

The port 1 of the VNA was calibrated for S11 parameter from start frequency 1GHz to stop frequency 3 GHz. The number of scanning points taken in the frequency range of operation was set as 601. The calibrated range profile of the VNA with no DUT connected at the end has been shown in Figure 3.5.

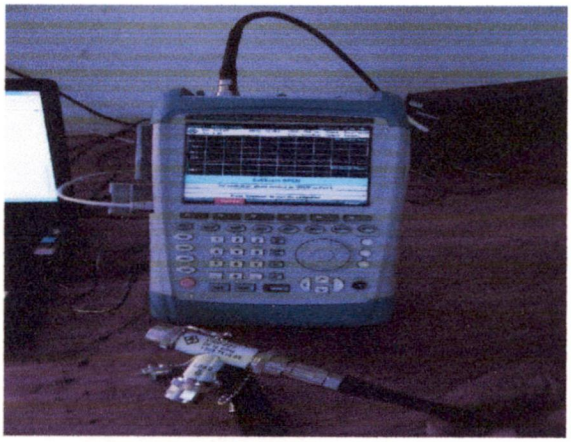

(a) VNA being calibrated for 1 GHz to 3 GHz

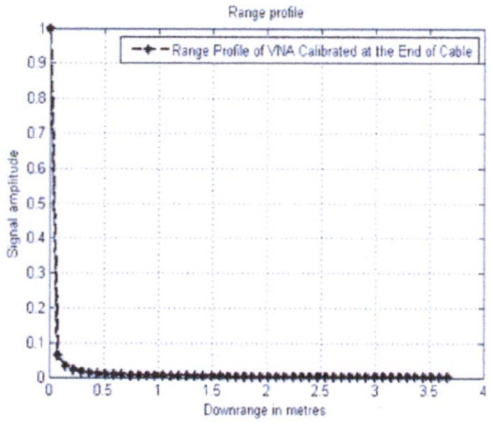


(b) Calibrated range profile of VNA with no DUT connected

**Figure 3.5: VNA Calibration and range profile of calibrated VNA with no DUT attached**

### 3.2.2. Time Gating

Now, VNA has been calibrated till the end of the cable. When antenna is connected at the end of the cable as DUT, reflections are there as signal enters antenna from the cable and then as signal propagates from antenna to the air. As all the distances can be conveniently measured from the antenna flare, we apply time gating to shift the zero of the distance at the antenna flare and ignore the reflections at cable-antenna interface and antenna-air interface [53]. An aluminum metal sheet is placed just at the flare of the antenna. No signal will pass through the metal sheet and we will get a sharp reflection at the point where the flare ends. This distance will be subtracted from the distances that we get henceforth. It is found that this distance is 30 cm. Time gating method has been shown in Figure 3.6.

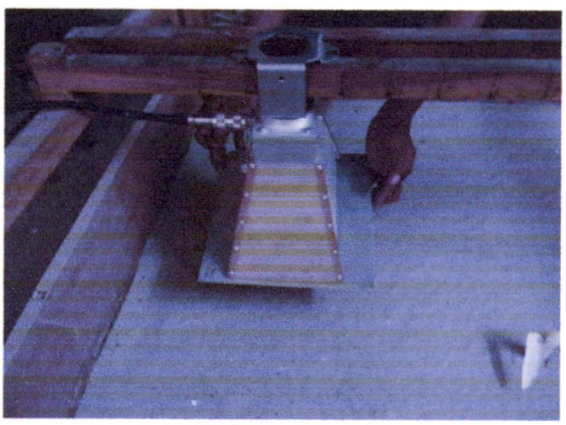

(a) Method for time gating

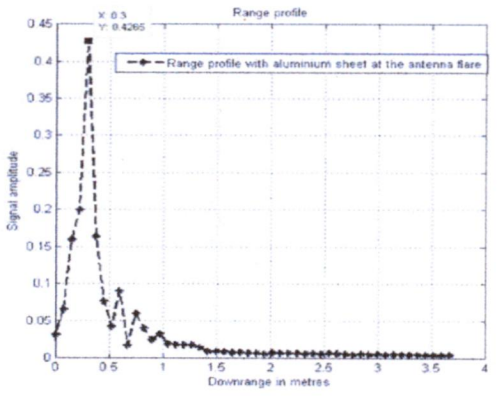


(b) Range profile with aluminium sheet at antenna flare

**Figure 3.6: Time gating and range profile with aluminum sheet at antenna flare**

### 3.2.3. A-Scan

A-Scan is one dimensional trace and gives range profile at a particular depth. Antenna is placed at any point of interest and signal is collected. As the received data is in frequency domain, IFFT is taken to get signal strength versus time delay. This information is mapped on distance indexes. In the plot so obtained peaks are looked for to locate a probable presence of target [22], [23]. A flowchart for A-Scan algorithm is given in Figure 3.7.

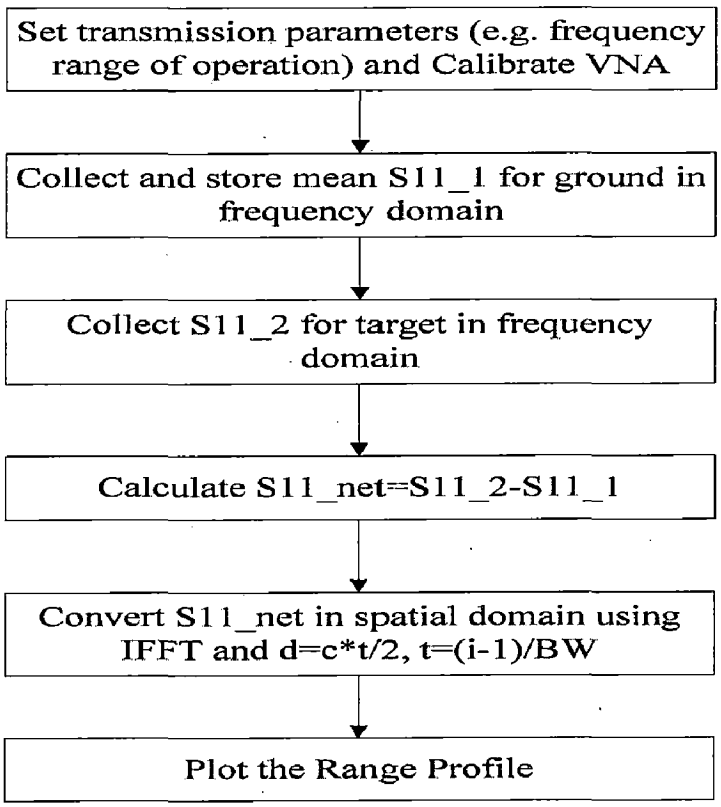


**Figure 3.7: Flowchart for A-Scan algorithm**

The detailed algorithm can be explained as follows:

1. We decide for the range of frequency for which observation is to be taken. A compromise has to be made as higher frequencies offer better resolution but attenuate faster. Also range resolution gets fine as operating bandwidth is increased. For the selected range the VNA is calibrated. If we change the range of frequency, VNA has to be calibrated again.

2. S11 is collected for the ground in frequency domain when no target is present. This contains information about the range profile of the sand. As in practical cases it is not feasible to take ground reading at the same location at which target is being investigated, an assumption is made. Several S11 readings are taken at various locations where we know that no target is there and its mean is taken as S11 for ground. Let this S11 be represented as $S11_1$.
3. S11 is taken at the investigated location in frequency domain. Let this S11 be represented as $S11_2$.
4. We calculate $S11_{net} = S11_2 - S11_1$. This implies that the background information about the ground has been removed and now $S11_{net}$ has information pertaining to the target only.
5. This frequency domain data is in 601 points. A time matrix is defined with same number of points to convert this frequency data into time data.
6. The IFFT is applied on this frequency domain data of 601 points. Inverse Fourier Time Domain data can be represented as:

$$s(t) = \sum_{n=1}^{N} S(f_n)\exp(j2\pi f_n t) \tag{3.7}$$

Where N is the maximum number of data points that is set as 601 here. $S(f_n)$ is the received reflected signal in frequency domain at $n^{th}$ frequency. '$n$' varies from 1 to 601. And $s(t)$is the received reflected signal in time domain. '$t$' varies from 0 to $(N-1)/BW$ with step interval of $1/BW$. In this case $BW$=2 GHz.

7. This time domain data is mapped in spatial domain to get range profile. This mapping is done by setting:

$$z = ct/2 \tag{3.8}$$

where, $z$ is the distance along the range profile.

8. By plotting the time matrix data obtained after the IFFT against the distance $z$, location of the buried object can be located by observing the peaks in the range profile.

### 3.2.4. B-Scan

Stacking A-Scans along a dimension of the soil pit results in the formation of B-Scan. A B-Scan gives us a 2-D image which tells us about the depth at which the target is located and the extent of the target in azimuth direction, i.e. along the direction in which scanning has been done. Concept of B-Scan is explained by Figure 3.8.

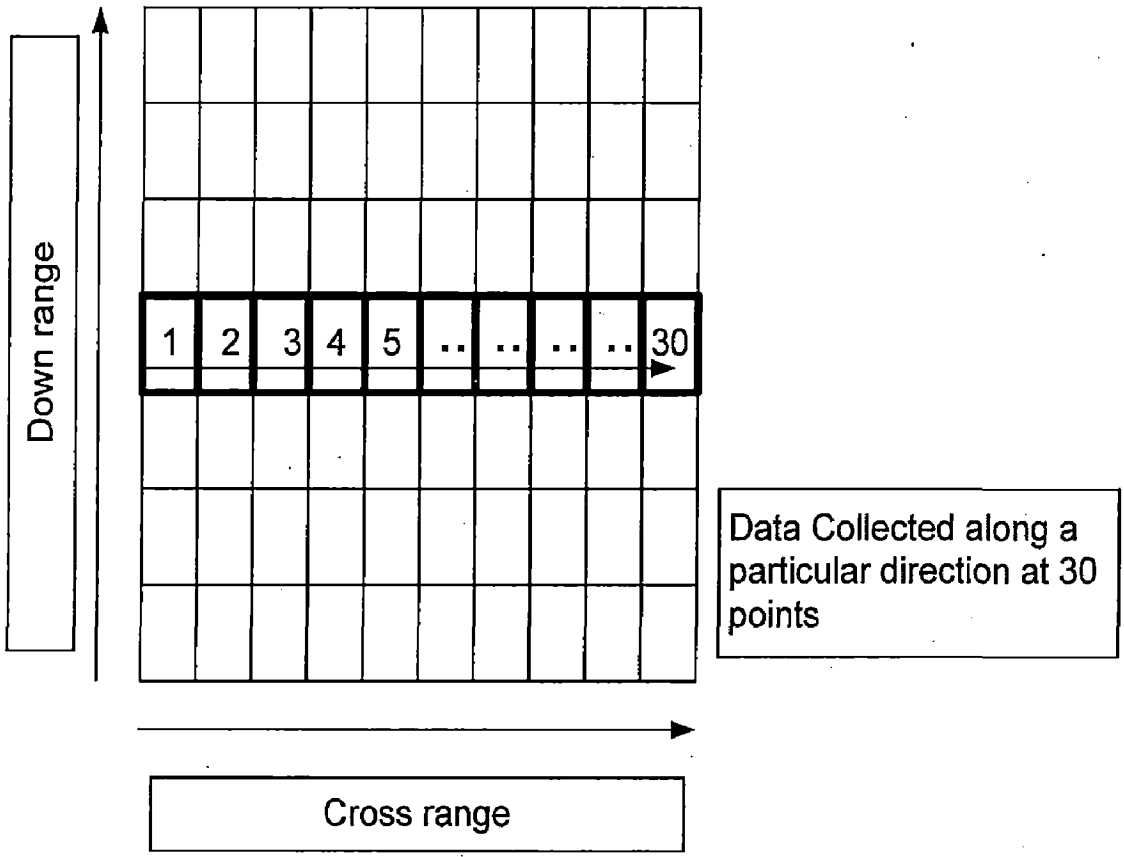


**Figure 3.8: B-Scan as stacking of several A-Scans**

B-Scan can be uniform as well as non-uniform. In uniform B-Scan, spacing between successive B-Scans is always the same, however, in non-uniform B-Scan it is not so. In this work a regular spacing could not have been maintained and hence non-uniform scanning has been done. For this work, targets were buried at different depths under different moisture conditions in a straight line. Several B-Scans of 30 A-Scans were done to detect and classify the targets [22], [23]. A flowchart for B-Scan algorithm is given in Figure 3.9.

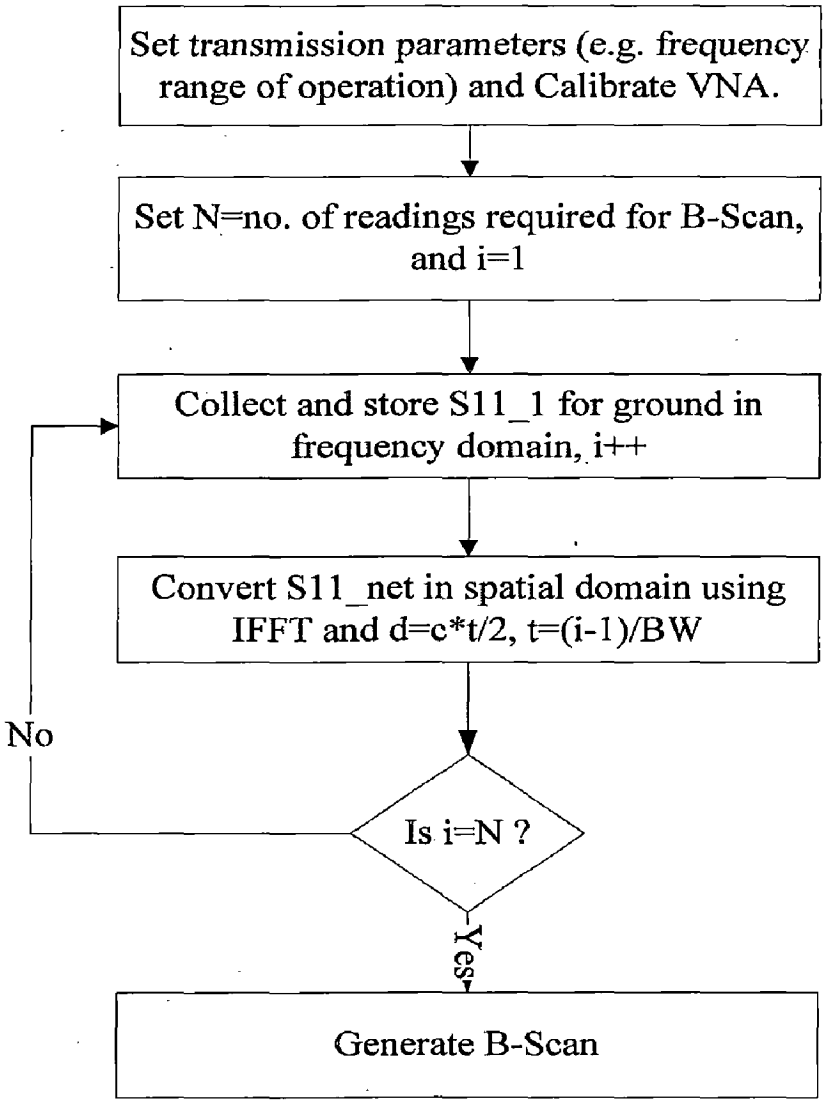


**Figure 3.9: Flowchart for implementation of B-Scan algorithm**

Usually a B-Scan image is visualized with the scanning direction (distance) horizontally, and the time vertically. B-Scan image can be represented by equation (3.9) in which signal intensity is varying with the distances.

$$I(x,z) = s(x,z) = \sum_{n=0}^{N-1} S(f_n)\exp\left(j2\pi f_n(2z/c)\right) \tag{3.9}$$

Where, $x$ is the antenna scanning position and $z$ is the downrange locations for all the antenna positions.

## 3.3. Data Processing Algorithms for GPR

Previous section discussed how data was taken. Now the task at hand is to process this data so that meaningful conclusions can be drawn. This section deals with various data processing algorithms which have been applied on the GPR data to arrive at the results. Selection of these methods have been based on the brief review of previous works done be various researchers in this field. The flowchart given in Figure 3.10 shows various data processing algorithms used for target detection and classification.

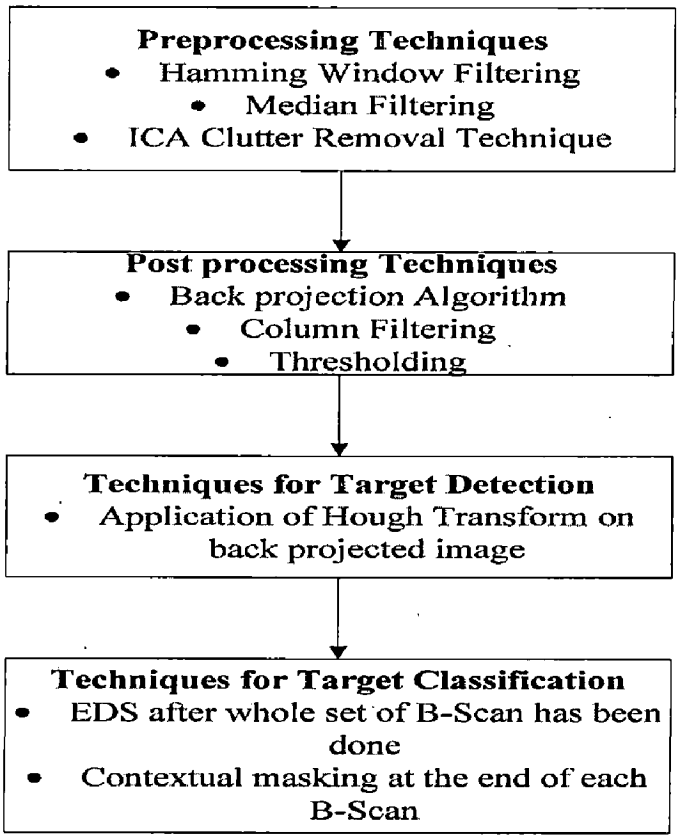


**Figure 3.10: Flowchart showing data processing algorithms used at each step in target detection and classification**

### 3.3.1. Preprocessing Techniques

**Filtering-** The noise and signal in frequency domain can be separated by Hamming Window Filtering or Median Filtering.

Hamming window [27] is a digital manipulation of the sampled signal in an FFT analyzer which forces the beginning and ending samples of the time record to zero amplitude. This

filtering rolls of the abrupt transition in frequency domain which in time domain means lower side lobes. For an '$N$' length sample the coefficients of a Hamming window are computed from the equation (3.10):

$$w(n) = 0.54 - 0.46\cos\left(\frac{2\pi n}{N}\right), \qquad 0 \leq n \leq N \tag{3.10}$$

Median filtering [54] is another technique that is widely used to remove abrupt internal noise in usually a time series signal. It is a nonlinear technique that applies a sliding window to a sequence. With median filtering, the center value in a window is determined by the *median* of the neighborhood values. Unlike averaging which compensates a sudden random noise in a group of samples by replacing each value in the window by the mean of the signal values in that window, median filtering attempts to eliminate the random noise completely.

**ICA Clutter Removal Technique for B-Scan Images** - When readings are taken in soil, reflections from clutters sometimes overshadow reflections from targets. Hence we don't need only removal of clutter; we need information about all the signal sources that make the final signal. From section 2.2 in the Chapter on brief review it was observed that Independent Component Analysis (ICA) [30]–[32] divides data into statistically independent components which gives it advantage over other clutter removal techniques like Singular Value Decomposition (SVD) or Principal Component Analysis (PCA). SVD or PCA represent data into uncorrelated components. Independent Component Analysis (ICA) minimizes both second-order and higher-order dependencies in the input data and attempts to find the basis along which the data (when projected onto them) are statistically independent. It is because of this property that ICA is widely used in many applications such as feature extraction and noise reduction from the images.

ICA assumes that the observed data $X$ has been generated from source data $S$ through a linear process $X = AS$, where both the sources $S$ and the mixing matrix $A$ are unknown. ICA is able to estimate both the sources $S$ and the mixing matrix $A$ from the observed data $X$ with very few assumptions which are:

a) Sources are independent and linearly mixed using a stationary and instantaneous mixing.
b) There are at least as many mixtures present as the no. of sources and most sources have Gaussian distribution.

Consider a B-Scan data which can be represented by a rectangular matrix $X_{ij}$, whose dimension is $M \times K$, ($i=1,2,.....M$; $k=1,2,....,K$). Here '$i$' denote the distance index and $k$ denotes the antenna position index. ICA assumes that every $x_i$ is a linear combination of each $s_j$ as follows:

$$x_i = \sum_{j=1}^{N} a_{ij} s_j \tag{3.11}$$

$j= 1,2, 3,...., N$ ($N$=no. of independent components to be calculated). In matrix notation

$$X = AS \tag{3.12}$$

Here $A$ is an $M \times N$ basis transformation or mixing matrix, and $S$ is the matrix holding the $N$ independent source signals in rows of $K$ samples. ICA of matrix $X$ can be found by finding a full rank $N \times M$ separating matrix $W$ such that output signal Matrix can be defined by $Y=WX$ and contain the components as independent as possible measured by an information theoretic cost function. The estimation of source signal can be done using equation (3.13) [32]

$$\hat{s}_j(k) = \sum_{i=1}^{M} w_{ji} x_i(k) \tag{3.13}$$

$j$=1,2,3,.....,$N$ (independent components). In the matrix notation

$$\hat{S} = WX \tag{3.14}$$

ICA looks for a linear transformation $W$ to maximize the "non-Gaussianity" of $s_i$ so that the transformed variables $\hat{s}_i$ are independent and the distribution functions for $s_i$ is least Gaussian. How ICA works has been summarized in the flowchart given in Figure 3.11.

The function $g(x)$ is given as:

$$g_1(x) = \tanh(a_1 y) \tag{3.15}$$

$$g_2(y) = y \exp\left(-\frac{y^2}{2}\right) \tag{3.16}$$

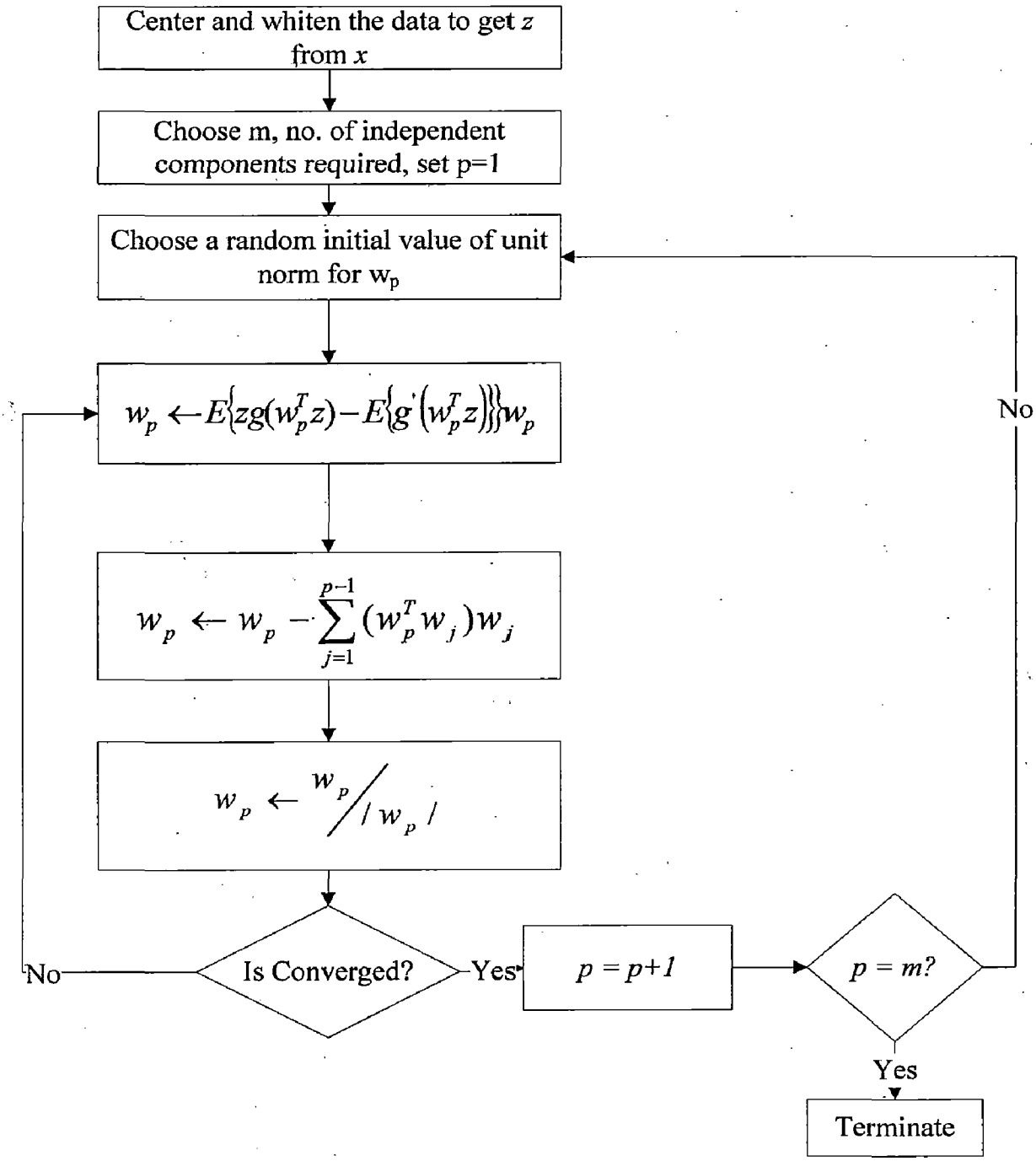


**Figure 3.11: Flowchart for implementation of ICA method of clutter removal from GPR images**

### 3.3.2. Post-processing Techniques

**Back projection [33]–[35]-** Back projection imaging algorithm is widely used in GPR imaging for image generation because of the high quality image it generates. A range profile generated by an A-Scan gives the signal strength as a function of time. In a raw B-Scan we consider that the reflected signal value is due to reflection from objects directly below the antenna. However, this is not true. It may be because of any object that falls in the swath of the antenna. The signal received at a given time can be from any of the pixel locations where total flight time is equal to this specific time bin. The total flight time is time to travel from transmitting antenna to the pixel and then back to receiver.

Figure 3.12 shows examples of pixel location where the reflected signal can come from (for a set of) collocated transmitting and receiving antenna elements. The back projection technique consists of recording the amplitude of each time bin on a spatial grid based on total flight time. After that all the recorded amplitudes from each channel are added together on the spatial grid. At the target locations the signal amplitude will add up coherently.

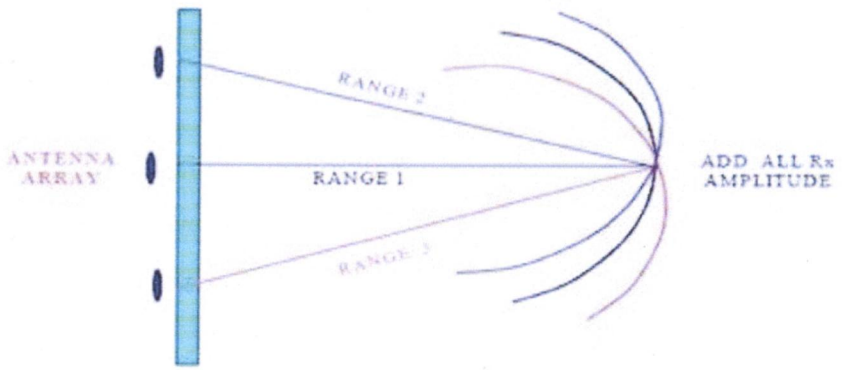


**Figure 3.12: Image showing back projection algorithm [55]**

The back projection algorithm can be implemented as follows:

1. Divide the whole region into small pixels.
2. For each pixel calculate the total flight time from transmitter to pixel and pixel to a receiver.

3. Record the corresponding received time bin amplitude for each pixel from the corresponding range profile means take the value of signal amplitude from the range profile and put it in that spatial grid.
4. Repeat step 2 and 3 for all receiver elements.
5. Sum the recorded amplitudes on the spatial grid.

The detailed back-projection algorithm applied for different moisture conditions of the soil has been given in Figure 3.13.

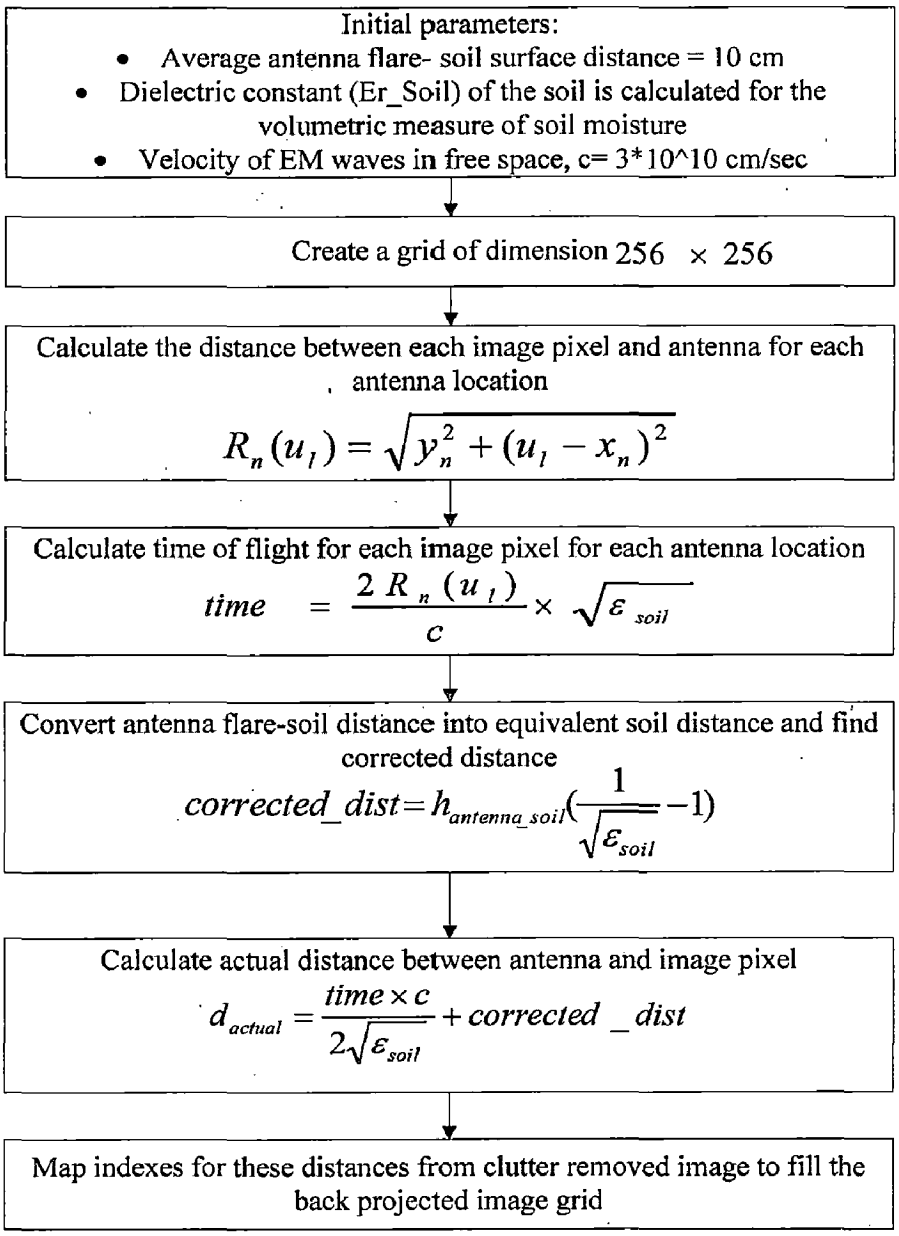


**Figure 3.13: Algorithm for forming back-projected image under various volumetric moisture levels of soil**

Mathematically in free space the back projected signal at pixel $(x_i, y_i)$ in the image plane is given by

$$I(x_i, y_i) = \sum_n s[t_i(n), n] \tag{3.17}$$

Where,

$$t_i = (T_i + R_i(n))/c \tag{3.18}$$

$$T_i = \sqrt{(x_i - x_T)^2 + (y_i - y_T)^2} \tag{3.19}$$

$$R_i(n) = \sqrt{(x_i - x_r(n))^2 + (y_i - y_r(n))^2} \tag{3.20}$$

Where, $c$ is the speed of light in free space, $t$ in second, $x$ , $y$, $T$ and $R$ in meter. $t_i(n)$ is the total time for the transmitted signal to travel. In monostatic mode as transmitter and receiver is the same,

$$t_i = 2(R_i(n))/c \tag{3.21}$$

**Column Filtering [36]-** We have discussed it earlier that the swath that antenna covers at various depths is proportional to square of depth. In image terms it means that antenna covers more number of pixels in a single scan as depth of the targets is increased. As there is interference of the other grid points in that particular pixel's value, filtering needs to be applied to remove the impact of the overlapping data. Out of column filtering, block processing and sliding neighbourhood operation methods of filtering, column filtering has been preferred. Block processing doesn't address overlapping efficiently and sliding neighbourhood is more complex when compared to column filtering. It is observed that neigbouring values in a raw image show sharp discontinuities. To remove these column filtering is done, which makes the transition from one pixel to another smooth and continuous. Filtering is done as shown here:

$$A(x', y') = mean(A((x - 1{:}x + 2), (y - 1{:}y + 2))) \tag{3.22}$$

Where $A(x, y)$ is the original pixel where filtering has to be done and $A(x', y')$ is the pixel after filtering has been applied. The colfilt function in MATLAB has been used to apply column filtering on B-Scan images after ICA.

**Thresholding [23]**- The image so generated after Backprojection may have some pixels which make the image look cluttered. Therefore, thresholding is applied to this image. The thresholding point is a function of mean and variance of the image data. A threshold values is set and image pixels having values less than the threshold are considered to be due to background and those having values higher than the threshold are taken to be due to foreground. A proper tradeoff is required in setting this threshold value. If threshold value is too small, inclusion of noise leads to clutter effects and if it is too high important information such as reflections due to low dielectric material get excluded.

There are primarily two types of thresholding:

1. Otsu Thresholding: It is based on probability and histogram method. Image is divided into two segments- foreground and background. An initial threshold is considered and by using this threshold the probabilities of the particular being in the foreground or background is considered.
2. Mean Deviation based thresholding – The function used for thresholding is the sum of mean and standard deviation multiplied by a weight. This method has been preferred over Otsu as its performance is similar to it but complexity and data processing time is less.

$$\mu = \frac{1}{N}\sum_{j}\sum_{i} x_{ij} \tag{3.23}$$

$$\sigma = \sqrt{\sum_{j}\sum_{i}(x_{ij} - \mu)^2} \tag{3.24}$$

$$Threshold = \sigma + k\mu \tag{3.25}$$

Where, $\mu$ = mean of image pixels, $\sigma$= standard deviation of the image pixels, $k$ is the weight of standard deviation used in the computation.

### 3.3.3. Image Detection Using Hough Transform

A backprojected image gives us hyperbolas corresponding to targets. The apexes of these hyperbolas give us the location of targets. Because of the different reflected strengths of different materials, the hyperbola because of low dielectric material may not be a prominent one. If most important hyperbolas can be extracted out the image our target is

detected irrespective of its dielectric constant. Hough transform has been used in past to address this problem [39], [40], [42]. Basic principle of Hough Tansform [56] is this:

If we want to find a particular shape in usually a binary image, we find all possible parameters that define the shape. And then we extract a subset of parameters which satisfy most number of points in the image.

It is proven that back projection gives hyperbolas in the image. After thresholding sobel operator is applied to get a binary image. Sobel operator is a discrete differential operator constituted of two templates as shown below:

Suppose the resultant GPR image from previous steps be $g(x, y)$. The gradient image $G(x, y)$ of $g(x, y)$ can be obtained by using the Sobel edge operator as followings [39]:

$$G(x,y) = \sqrt{G_x^2 + G_y^2} \tag{3.26}$$

Where $G_x$and $G_y$ are respectively [39],

$$\begin{aligned} G_x = {} & [g(x-1,y+1) - g(x-1,y-1)] \\ & + 2[g(x,y+1) - g(x,y-1)] \\ & + [g(x+1,y+1) - g(x+1,y-1)] \end{aligned} \tag{3.27}$$

$$\begin{aligned} G_y = {} & [g(x+1,y-1) - g(x-1,y-1)] \\ & + 2[g(x+1,y) - g(x-1,y-1)] \\ & + [g(x+1,y+1) - g(x-1,y-1)] \end{aligned} \tag{3.28}$$

Now, the hyperbolas in the back projected image are north-south hyperbolas and only the South portion of them can be seen in the image. A north-south hyperbola is given by:

$$\frac{(y-y_o)^2}{b^2} - \frac{(x-x_o)^2}{a^2} = 1 \tag{3.29}$$

Some valid assumptions can be made here. As the back projected image is a matrix of dimension $256 \times 256$ , for the hyperbola, $y_o = 256$, which is the highest row-value of back projected image matrix generated in this work. '$b$' can be found directly from the binary image. So, we find all the positive possible values of '$a$' for non-zero pixels $(x,y)$ from the binary image by equation (3.30).

$$a = \sqrt{\frac{(x - x_o)^2}{(\frac{y - 256}{b})^2 - 1}} \tag{3.30}$$

Where, $1 \leq x_o \leq 256$, and $a$ can take only positive values. Following flowchart (Figure 3.13) explains how target detection is done using Hough Transformation.

As this work was carried out with three targets viz. an air cavity, a metal sheet and a water bottle, number of peaks that was to be searched in the Hough Transform matrix was set as 3 (three).

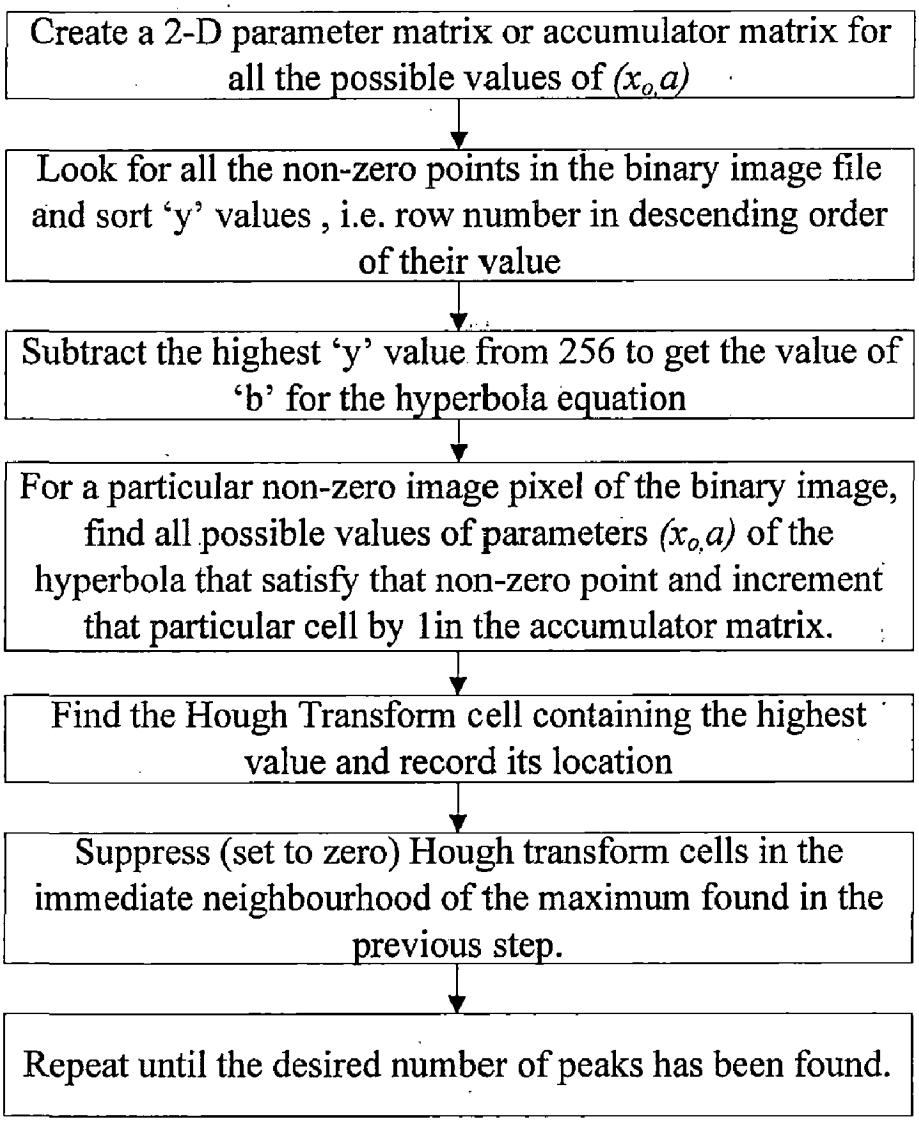


**Figure 3.14: Flowchart for implementation of Hough Transform**

### 3.3.4. Target Classification

**Use of Neural Networks and Correlation Coefficient for Target Classification Using EDS-** The GPR signal from various targets can act as their signatures in the sense that the GPR signal depends upon the target's size, shape, composition as well as its burial depth and orientation. The signal received in frequency domain at a particular location is the composite of signal due to target and signal due to clutters. If we are able to remove clutter, we will have signal only because of target. This information can be used to classify different targets as they vary in their composition and dielectric properties. It is in this view that Energy Density Spectrum has been generated for various scan points and neural networks has been used for pattern classification to identify given targets. As Ho et al. [43] have put in their paper that frequency domain signatures have more consistency in the region between 1 GHz to slightly above 2 GHz, the energy density spectrum was split in 4 frequency bands viz. 1-1.5 GHz, 1.5-2 GHz, 2-2.5 GHz and 2.5-3 GHz. Consistency of signatures of similar targets in first three bands was investigated and used to classify the targets.

Though, the signals can be classified by Pearson's Correlation Coefficient between the spectra of different targets in the 4 frequency bands also, Neural Networks turned out to be more trustworthy for target classification. Probabilistic Neural Networks [42], [46] has been widely used for pattern classification by different researchers. First, the network is trained by spectra of different targets under different moisture conditions and for different burial depth. It was followed by feeding test spectra to the network for their classification. In probabilistic neural networks when an input is presented, the first layer computes distances from the input vector to the training input vectors and produces a vector whose elements indicate how close the input is to a training input. The second layer sums these contributions for each class of inputs to produce as its net output a vector of probabilities. Finally a transfer function on the output of the second layer picks the maximum of these probabilities, and produces a 1 for that class and a 0 for the other classes. Flowchart given in Figure 3.15 explains how EDS can be generated from GPR signal and used for classification.

Salient features of different steps involved in this process have been given below.

**Whitening and normalization [42]-** is done mainly to remove ground effects from each of the reading. Readings are taken for ground where it is known that there is no target. These readings are averaged to find the average behavior of the ground and standard deviation is found to calculate how much the behavior changes in these readings. If the mean behaviour of ground is $m_A(k_z)$ and its standard deviation is $\sigma_A(k_z)$, then the whitened and normalized reading at each of the scan points is:

$$U(x,y,k_z) = \left(\frac{A(x,y,k_z) - m_A(k_z)}{\sigma_A(k_z)}\right) \tag{3.31}$$

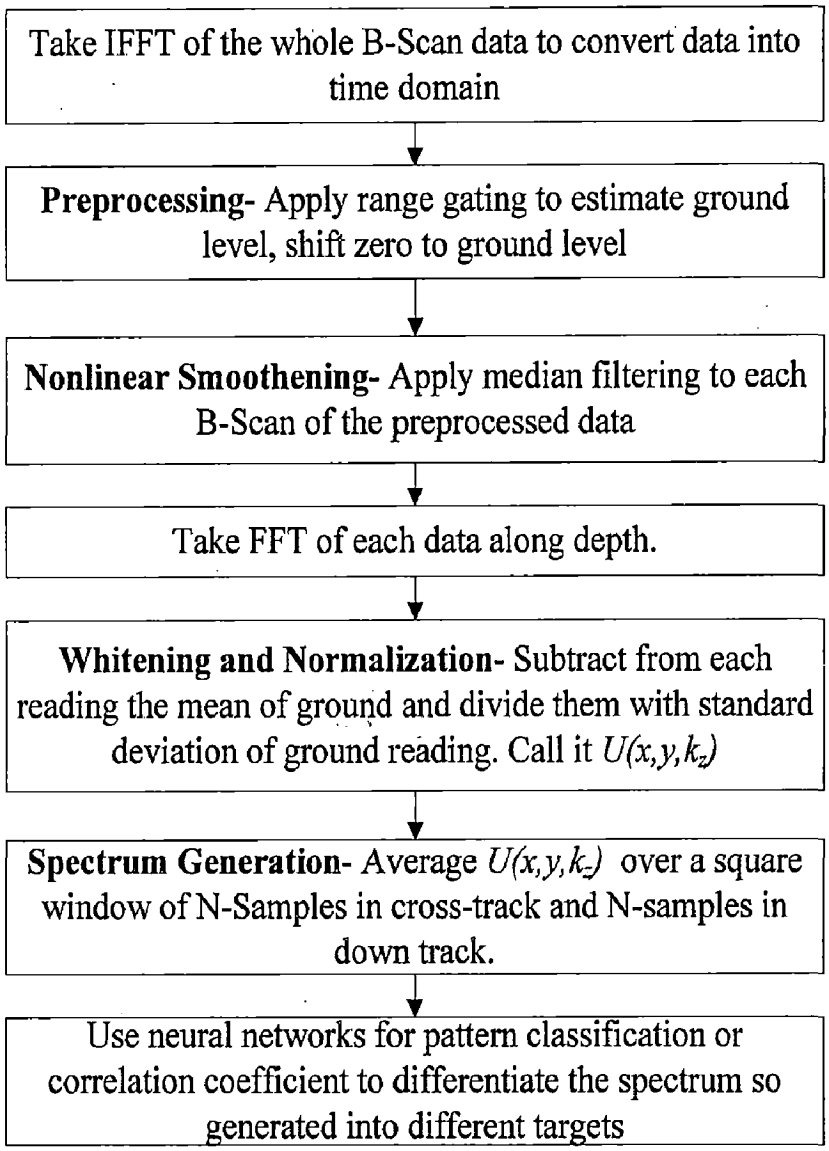


**Figure 3.15: Flowchart for implementation of EDS method of target classification**

**Spectrum Generation [42]-** The spectrum is generated by averaging $U(x, y, k_z)$ over a square window of $N$ samples in cross track and $N$ samples in down-track. This averaging is done to reduce the variance in the EDS estimate. As the average distance of antenna from the soil surface was 10 cm i.e. a swath of 314.15 $cm^2$ at the surface of the soil, or approximately a square with its side of 17cm, averaging was done by taking $N = 4$, assuming that traverse distance between each scan points is roughly equal to 4 cm.

$$P(x_o, y_o, k_z) = \frac{1}{N^2} \sum_{x=x_o-(N-1)/2}^{x_o+(N-1)/2} \sum_{y=y_o-(N-1)/2}^{y_o+(N-1)/2} U(x, y, k_z) \tag{3.32}$$

**Pearson's Correlation Coefficient [42]-** The spectrum so generated can be classified using Pearson's Correlation Coefficient. A standard library can be maintained for different targets at different depths under different moisture conditions. As spectral variation can be expected to vary rapidly at higher frequencies, correlation coefficient can be found separately for four different frequency bands. Pearson's Correlation Coefficient is given as:

$$\rho_{xy} = \frac{\sum(x - \mu_x)(y - \mu_y)}{\sqrt{\sum(x - \mu_x)^2 (y - \mu_y)^2}} \tag{3.33}$$

**Probabilistic Neural Network (PNN) [57]-** Donald F. Specht proposed this method to formulate a neural network. He called this a "*Probabilistic Neural Network*". Figure 3.16 shows the architecture diagram of a PNN network.

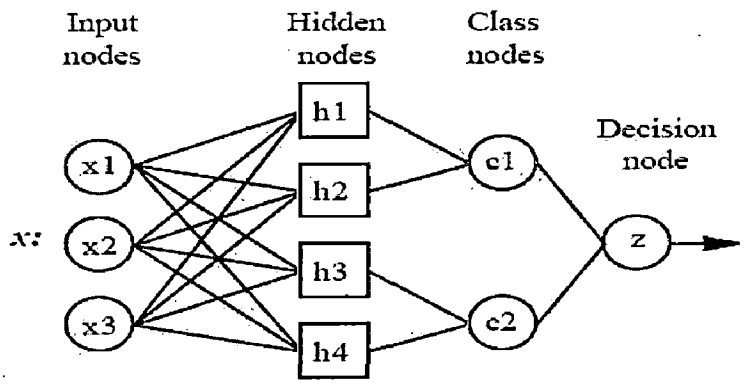


**Figure 3.16: A four layer architecture of probabilistic neural network [57]**

- **Input layer** - there is one neuron in the input layer for each predictor variable. In case of categorical variables, $N$-1 neurons are used where $N$ is the number of categories. The input neurons standardize the range of the values by subtracting the median and dividing it by their inter quartile range. The input neurons then feed the values to each of the neurons in the hidden layer.
- **Hidden layer** - this layer has one neuron for each case in the training data set. The neuron stores the values of the predictor variables for the case along with the target value. When presented with the $x$ vector of input values from the input layer, a hidden neuron computes the Euclidean distance of the test case from the neuron's center point to decide the Kernel function. The resulting value is passed to the neurons in the pattern layer.
- **Pattern layer / Summation layer** - there is one pattern neuron for each category of the target variable. The actual target category of each training case is stored with each hidden neuron; the weighted value coming out of a hidden neuron is fed only to the pattern neuron that corresponds to the hidden neuron's category. The pattern neurons add the values for the class they represent.
- **Decision layer** - the decision layer compares the weighted votes for each target category accumulated in the pattern layer and uses the largest vote to predict the target category.

**Contextual Masking for Successive Classification of Target [22]**- Because of clutters present in the soil and high attenuation of signals in it, spectral features sometimes fail to get the target classified. It was found in experiments that the neural network sometimes confused air cavity with water bottle. We can use another feature of targets to classify them. It is that the reflected signal strength of metal sheet is strongest followed by that of air cavity which is then followed by water bottle. Jain has done an extensive study on the reflected signal strength of these targets under various moisture levels of the sand and at various depths in his dissertation work. After the thresholding stage, the background noise is removed and we are left with targets present at that depth. The pixel values corresponding to these targets have been successively used to classify them. The strongest reflector in the image is classified as:

$$[Ref], [x, y] = \max(\max(Image[1: N_x, 1: N_y])) \quad (3.34)$$

Where, $x,y$ are the coordinates of the strongest pixel and *Ref* is the value of this particular pixel. $N_x, N_y$ are the size of the image in $x$-direction and $y$-direction respectively. A group of pixels in the neighbourhood of this pixel is masked and then the next highest value is looked for. This masking is necessary as sometimes in the presence of strong reflector, signals due to weak reflectors may not be visible at all and we may not know that there is another target as well. Also, the next strongest pixel in the identified object might be stronger than the strongest pixel in the next object to be identified and the target may get missed from being identified. The algorithm can be explained as given in flowchart in figure 3.16.

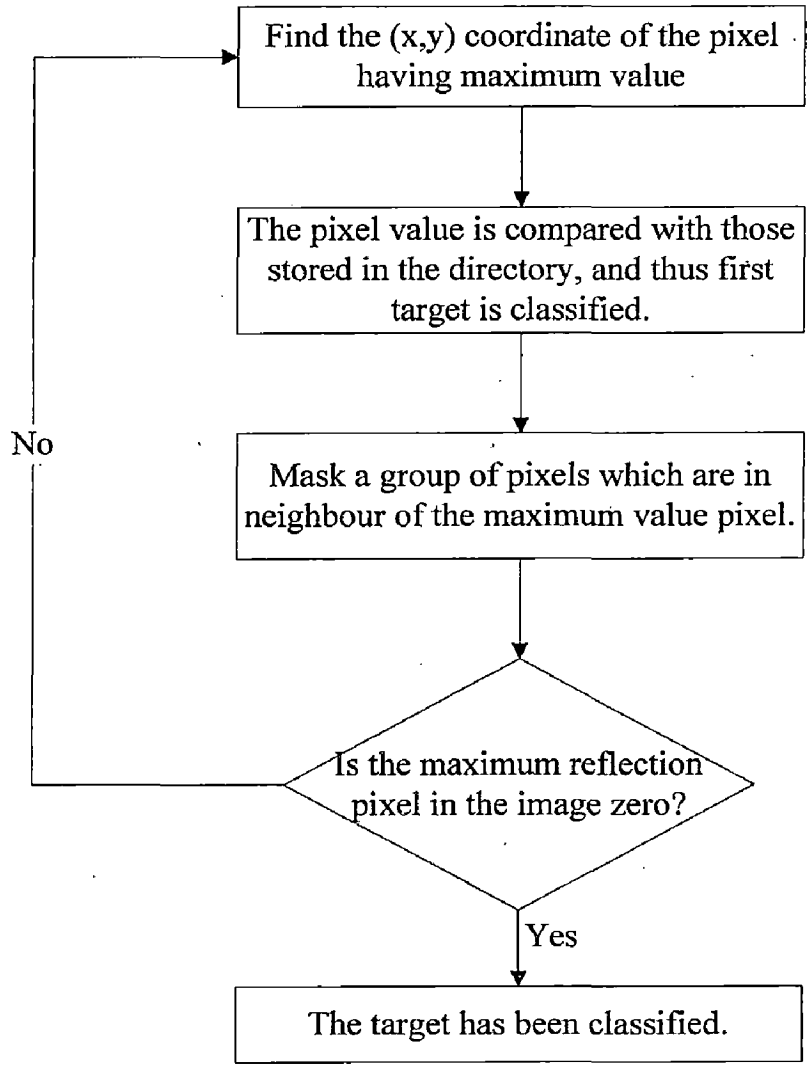


**Figure 3.17: Flowchart for contextual masking for successive identification of targets**

### 3.3.5. Model Development

With this knowledge, a model was developed for real time target detection and classification of the targets. Figure 3.18 gives a succinct account of the same. Target classification can be done in three ways. The first is after each B-Scan using contextual masking. However, it's probable that in that scan our scanner may miss some of the targets and we don't have complete information about all the targets in a single scan. After all the M B-Scans have been done Energy Density Spectrum for each point is generated and is compared with stored spectra to classify the target. It is to be noted that a combination of all the three ways to classify the target is required.



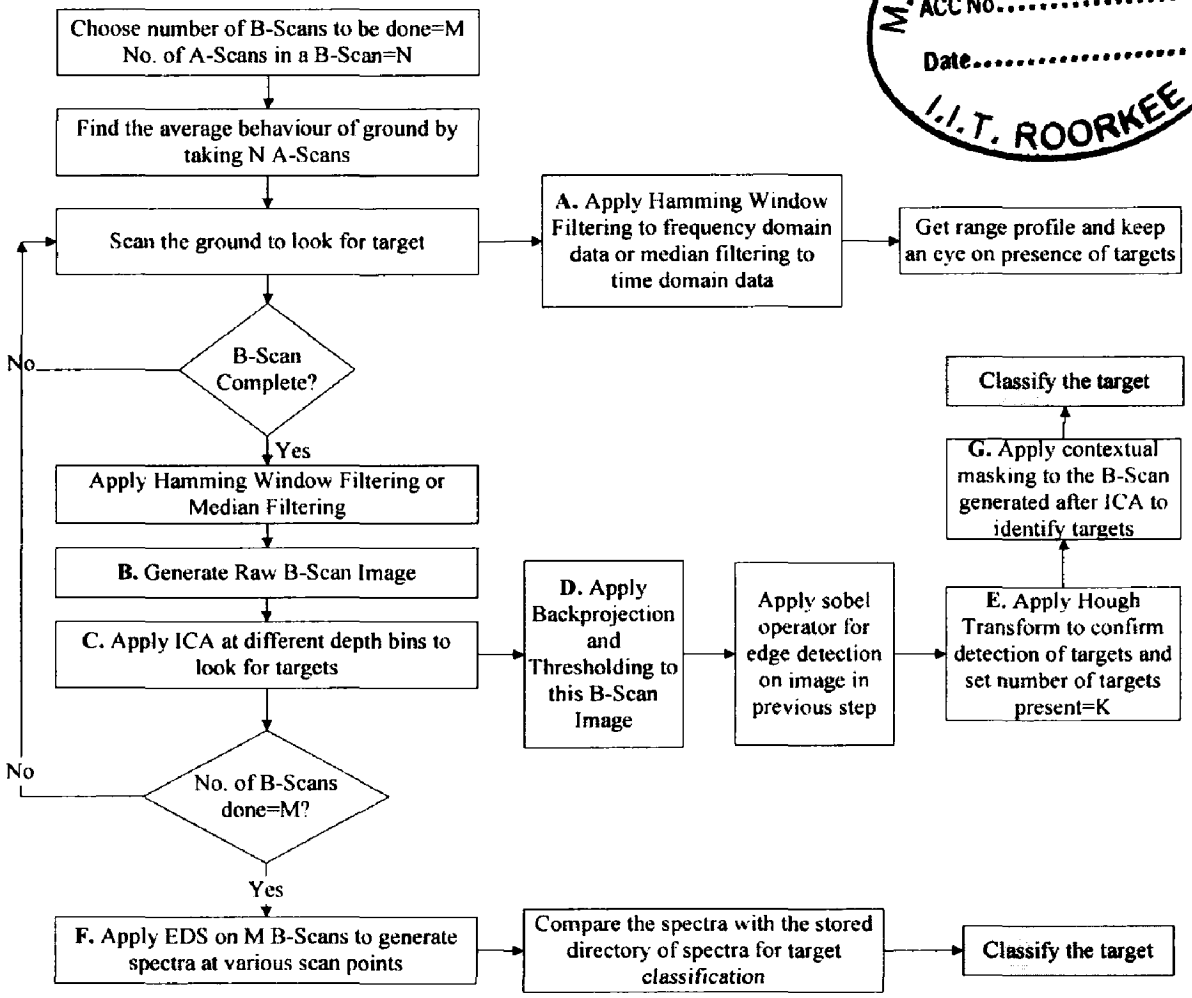


**Figure 3.18: Flowchart for implementation of real time target detection and classification**

# Chapter 4. Implementation, Results and Discussions

As per the model developed in previous chapter, GPR data was taken and processed for target detection and classification. For carrying out the experiments, four to six B-Scans of 30 A-Scans were done with targets buried at different depths under different soil moisture. Before this, average behaviour of ground was estimated by taking readings of ground at 30 different locations at each moisture level of soil. This information was later on used for background subtraction for generating range profiles for individual A-Scans and then for generating EDS of targets. This chapter deals with results obtained on step-by-step implementation of the model developed in section 3.5. The reasons for the results so obtained have also been discussed.

## 4.1. Preprocessing Techniques on A-Scan and B-Scan

Importance of A-Scan detection and how it is done has been discussed in section 3.2.3. Details of how B-Scan image is generated by stacking A-Scans has been given in section 3.2.4. Preprocessing techniques like Hamming window and median filtering and ICA clutter removal has been discussed in section 3.3.1. Subsections of this section show the results obtained by the application of these preprocessing techniques on GPR data.

### 4.1.1. Hamming Window Filtering and Median Filtering for A-Scan

Hamming window filtering (equation 3.10) is applied on frequency domain data. It basically shapes the frequency domain data to roll off abrupt noises. Effect of applying this filter on an S11 waveform has been shown in Figure 4.1. It can be seen in the figure that application of window filtering suppresses the side lobes in the frequency domain GPR data. Hamming window passes this waveform through a cosine shaper. This helps suppress the effects such as ringing.

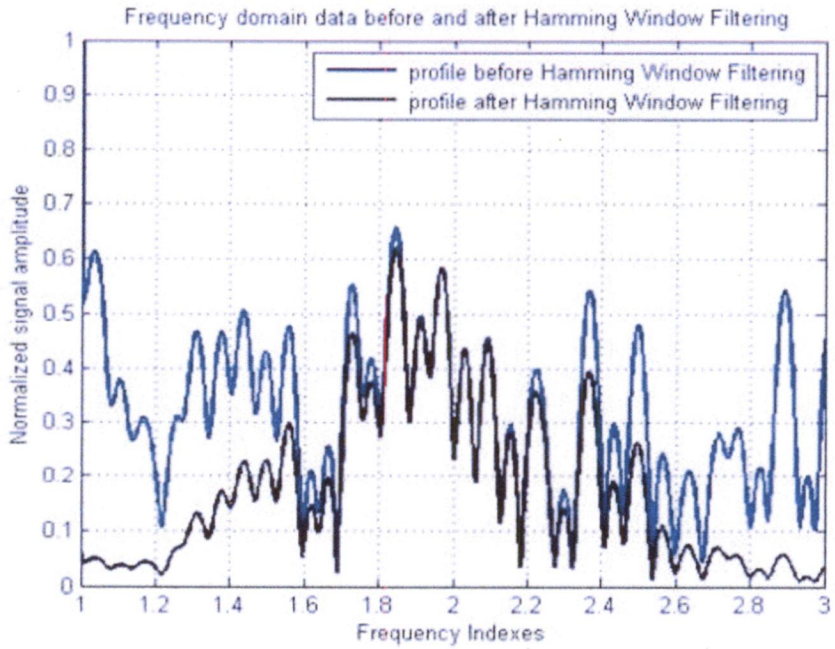


**Figure 4.1: Effect of applying Hamming Window filtering on frequency domain GPR data**

Time domain effect of application of hamming window filter and median filter (step A in the model developed in section 3.3.5) has been shown in Figures 4.2, 4.3 and 4.4 when targets were buried 10 cm deep with volumetric soil moisture level 15 %. Figure 4.2 show the effect on A-Scan (Figure 3.6) taken at the location where cavity was there. Figure 4.2 is for metal and Figure 4.3 is for water bottle.

As it can be seen that Figure 4.2 (a) has clutters in it at distances even after 1m and doesn't show the first reflection that was due to the cavity. It is to be noted that air cavity gives two reflections- first when EM waves enter cavity and second when EM waves exit cavity. Application of hamming window filter (Figure 4.2 (b)) shows both the reflections and also suppresses the reflections that were seen before for the distances after 1 m. Figure 4.2 (c) shows the A-Scan after application of median filtering. Considering the fact that range resolution is 7.5 cm for the GPR system used for carrying out the experiments and the median filter size is 3, it can be explained that the first reflection due to cavity has got eliminated as noise. Also, it can be noted that reflections after distances of 1 m have been suppressed more efficiently than in Figure 4.2 (a). Figure 4.2 (d) shows the A-Scan after application of both- Hamming window filter and median filter. Peaks

due targets are more prominent in this case than in the previous one. And it suppresses unwanted reflections as well.

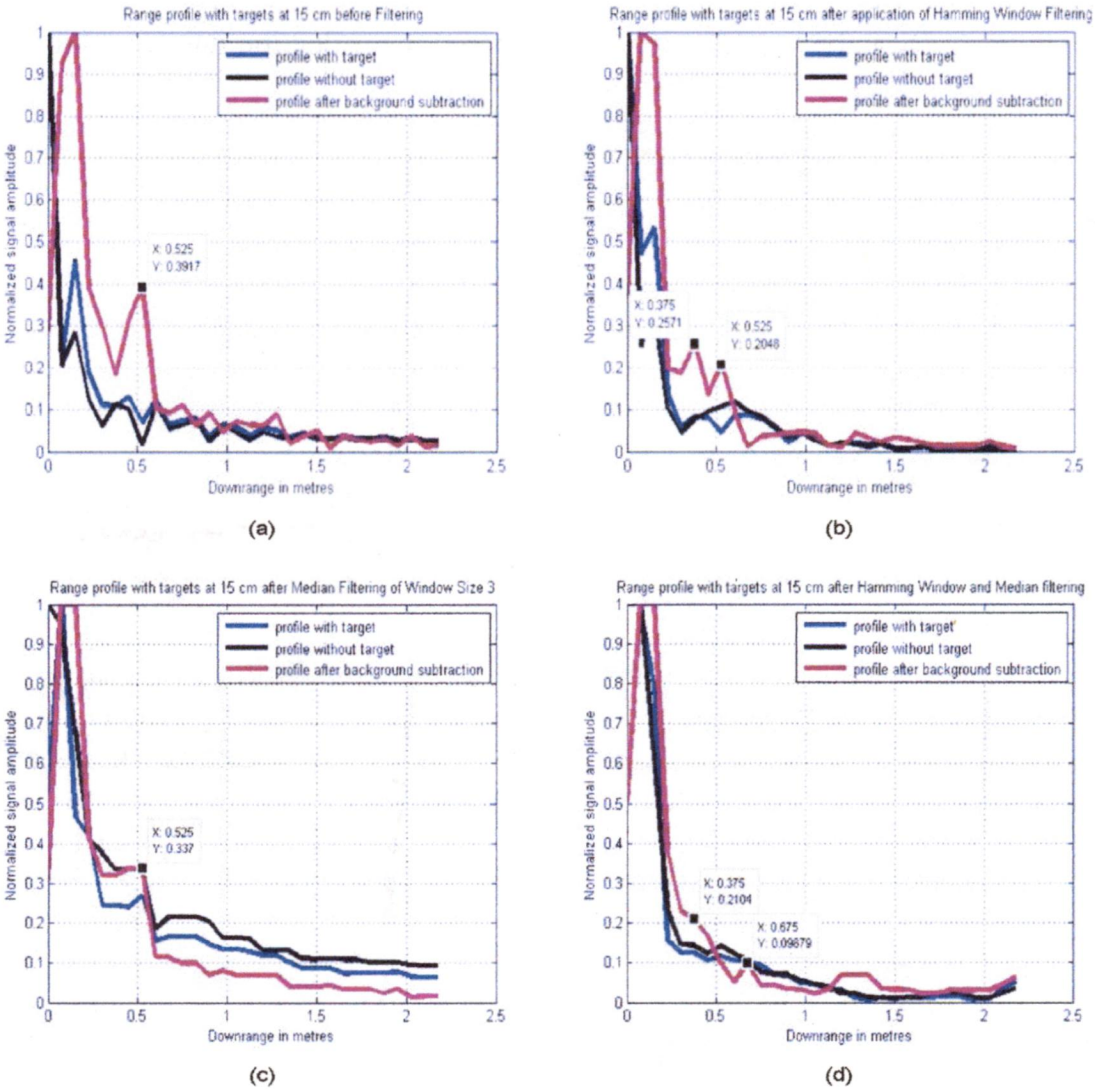


**Figure 4.2: (a) Raw A-Scan for location where cavity was there, (b) A-Scan after application of Hamming window filtering, (c) A-Scan after application of median filtering, (d) A- Scan after application of both- Hamming window and median filter**

Effect of these filtering techniques on metal sheet has been shown in Figure 4.3. Strong signal reflection due to metal sheet has made it possible that reflection due to metal is clearly visible in raw A-Scan (Figure 4.3 (a)). However, extra reflections can be observed in this figure which are surely due to noise. Figure 4.3 (b) shows the effect of application of Hamming window filtering on raw A-Scan. The first reflection is due to air-soil reflection and second is due to soil-metal sheet reflection. Also, it conforms to the concept that signal strength as distance increases should decrease. Figure 4.3 (c) shows

the A-Scan after application of median filtering. Reflection due to metal sheet is visible and has approximately the same signal strength as the first reflection due to air-soil. Figure 4.3 (d) shows the A-Scan after application of hamming window filter as well as median filter. It can be seen that it has suppressed the reflection due to metal sheet.

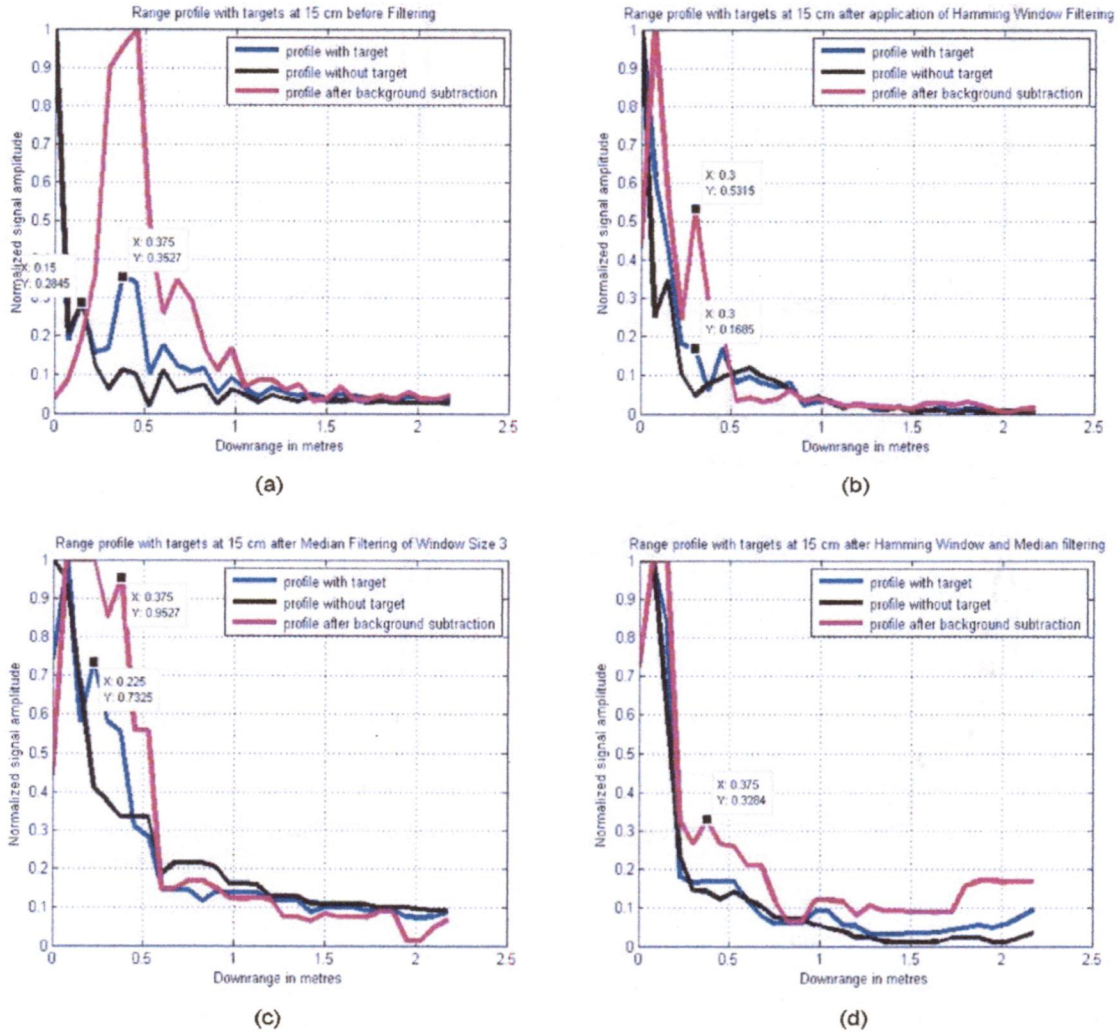


**Figure 4.3: (a) Raw A-Scan for the location where metal sheet was there, (b) A-Scan after application of Hamming window (c) A-Scan after application of median filter, (d) A-Scan after application of hamming window filter and median filter both**

Effects of application of these filters on A-Scan at the location where water bottle was there has been shown in Figure 4.4. Reflection due to water bottle is expected to be the weakest. Dielectric constant difference for bottle and soil is more than that for cavity and soil but, the cylindrical shape of water bottle results in low reflected signal strength for water bottle. Clutters are there in all the three figures Figure 4.4 (a-c). Though median filter has suppressed clutters effectively, reflection due to bottle cannot be distinguished

in the processed A-Scan. Figure 4.4 (d) has reflection due to water bottle visible in it but signal strength is too less.

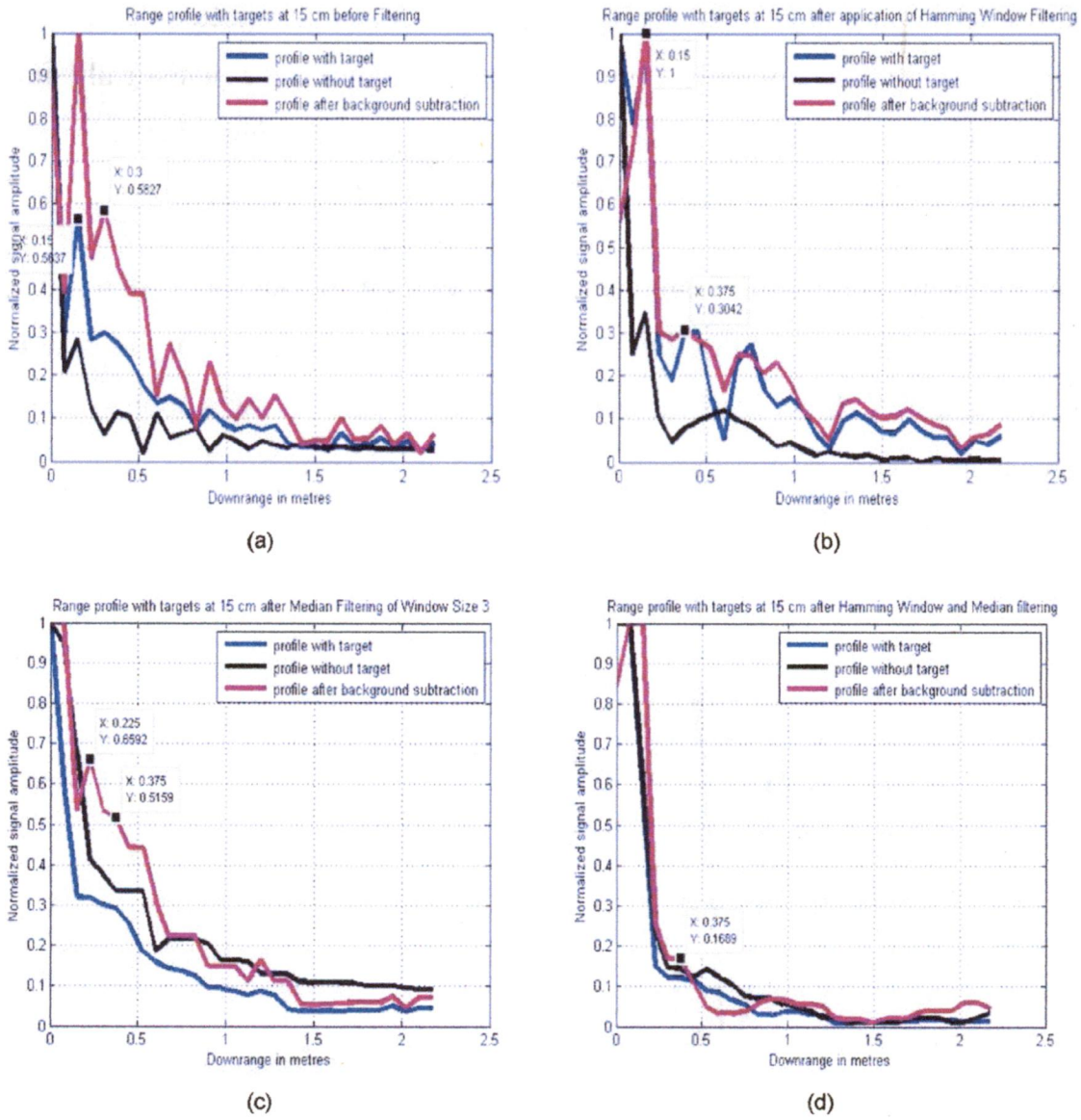


**Figure 4.4: (a) Raw A-Scan for location where water bottle is there (b) A-Scan after hamming window filtering, (c) A-Scan after median filtering, (d) A-Scan after application of hamming window filtering and median filtering**

From Figure 4.2 to Figure 4.4, it can be concluded that these methods are effective in combating noise in GPR signal. But more difficult condition makes it difficult for low dielectric materials, or cylindrical materials to be detected. Also, median filter has this disadvantage of suppressing reflection due to target sometimes. This often happens if there is a single peak representing the target. Thus for next requirements of pre-processing hamming window filter may be used.

### 4.1.2. ICA Clutter Removal for B-Scan Images

In soil EM waves attenuate faster. This makes detection of targets very difficult. Clutter removal techniques have to be applied so that target can be detected. It was explained in Chapter 3 that ICA not only removes clutters it looks for statistically independent components as well. In soil, where signal value to reflections due to target may be considered as clutter by SVD, PCA or FA, ICA serves the purpose better.

After completion of each B-Scan raw B-Scan images were generated (step B in the model developed in section 3.3.5) by following the algorithm discussed by flowchart given by Figure 3 and ICA clutter removal technique (refer Figure 3.9) was applied on this raw B-Scan image (step C in the implementation model of section 3.3.5). Effect of applying ICA on a single A-Scan has been shown in Figure 4.5.

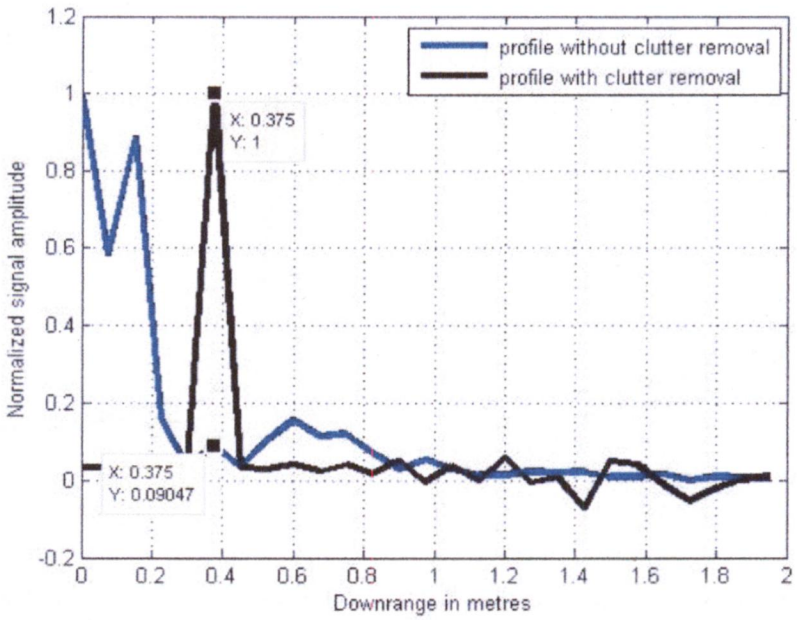


**Figure 4.5: Effect of applying ICA on range profile generated by a single A-Scan**

Results obtained after applying ICA on raw B-Scan images have been shown in Figure 4.6 when targets were buried 10 cm deep and volumetric soil moisture was 15 %.

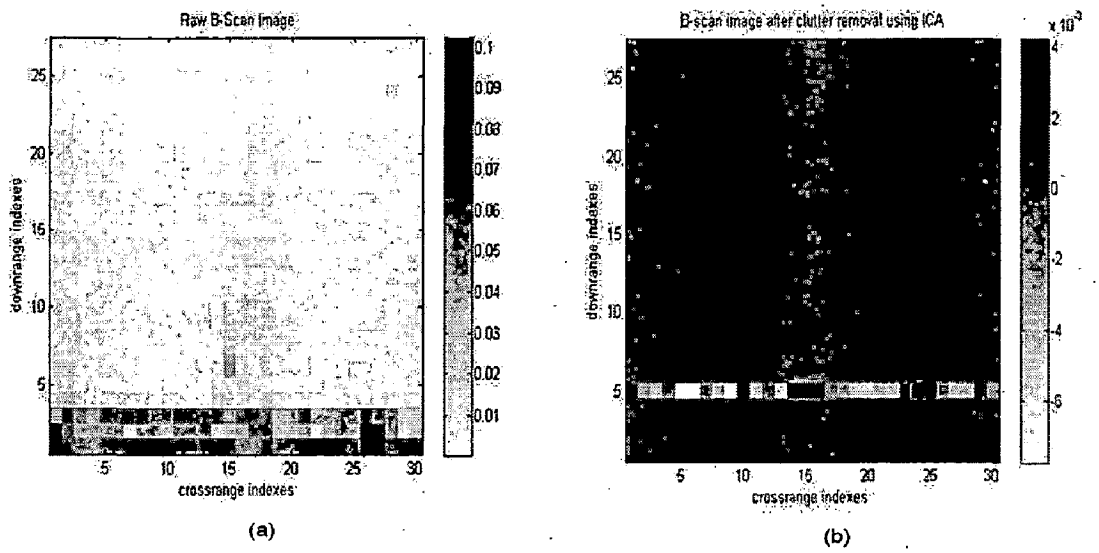


**Figure 4.6: (a) Raw B-Scan image generated of 30 A-Scan when targets were 10 cm deep and volumetric soil moisture was 15%, (b) Targets as detected by application of ICA at depth bin corresponding to 10 cm depth**

As it has been mentioned before, in the pit (of dimension 2m by 1.5 m) three targets were buried at a depth of 10 cm and water was added in a controlled fashion so that the volumetric soil moisture was 15%. Four B-Scans, each consisting of 30 A-Scans were done. From the point of start of scanning the order of the targets was air cavity followed by metal sheet and then water bottle. In first 10 readings presence of air cavity was expected, from $10^{th}$ reading to $20^{th}$ reading presence of metal sheet was expected, and finally from $20^{th}$ to $30^{th}$ reading were expected to show the presence of water bottle. The raw B-Scan generated after clubbing 30 A-Scans has been shown in Figure 4.6 (a). A 10 cm depth in soil having volumetric moisture 15% (dielectric constant of 7.70) means equivalent depth around 27 cm in air. If antenna-flare to soil-surface distance is considered total distance is around 37 cm. With a range resolution of 7.5 cm presence of targets at 5 downrange index is expected. If we consider downrange indexes in raw B-Scan, first two indexes show strong signal values which correspond to strong reflection from air-soil interface. However, no strong signal is visible at downrange index 5. It appears that all the three targets have been missed. ICA was applied on this B-Scan for depth bin 5 and four different patches can be observed. Since the environment is cluttered one of the patches can be due to a false target. But we can see the presence of rest of the three targets.

Another example of application of ICA for clutter removal from B-Scan is given in Figure 4.7.

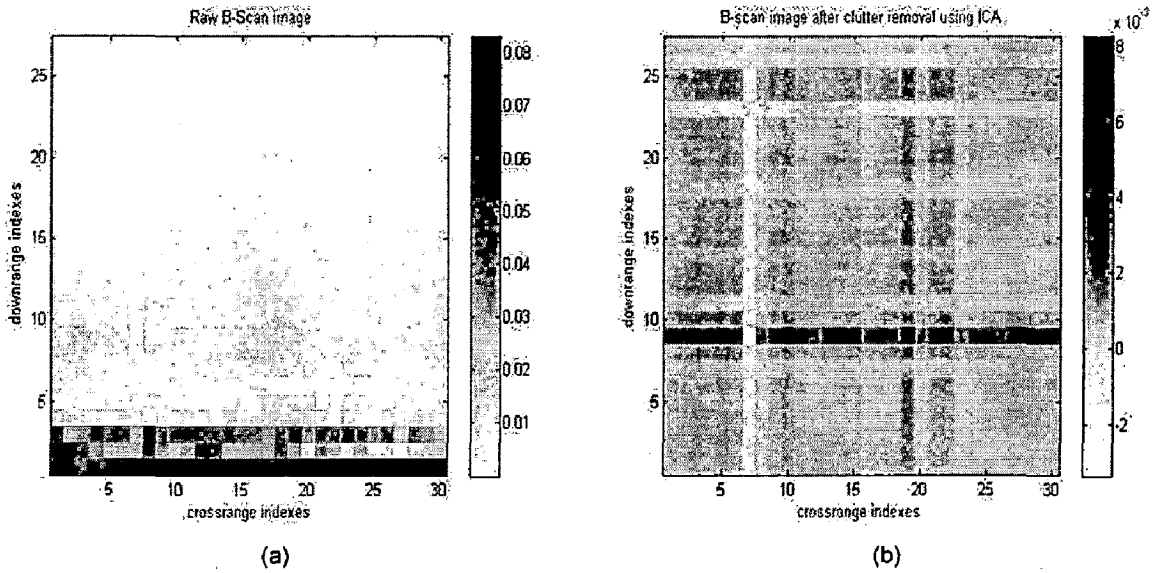


**Figure 4.7: (a) Raw B-Scan image generated by clubbing 30 A-Scans when targets are buried 20 cm deep in volumetric soil moisture of 20%, (b) B-Scan generated after clutter removal using ICA**

Like in the previous case, now soil moisture was increased up to 20% and depth of targets was increased to 20 cm. Arrangement of the targets was same – air cavity followed by metal sheet followed by water bottle. Antenna to target depth in this case is 30 cm but considering the fact that dielectric constant of soil for volumetric soil moisture level of 20% is around 10.12, effective distance becomes 67.5 cm. That is to say, target should be available at downrange index 9. Clearly, B-Scan doesn't give any trace of the targets. However, B-Scan generated after using ICA clutter removal technique some strong signal values can be seen at downrange index of 9. As antenna swath at depth of 30 cm (10 cm + 20 cm) was 3848.5 $cm^2$ , all the targets appear to be mixed up. That is to say, there is a continuous line of strong signal values at downrange index of 9. We have no way to determine the location of the three targets.

Before proceeding further, one more example of ICA is worth consideration. It is shown in Figure 4.8.

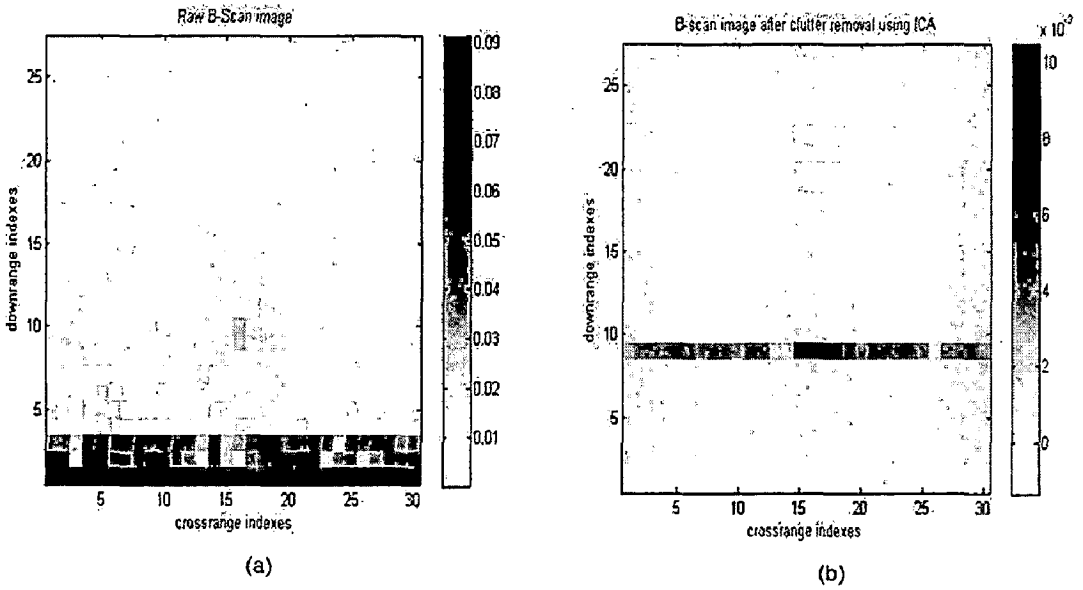


**Figure 4.8:(a) Raw B-Scan image generated when targets are 20 cm deep and soil moisture is 15%, (b) B-Scan image generated after ICA clutter removal**

This time targets are buried at the same depth of 20 cm but in different soil moisture level. Now, volumetric soil moisture is 15%. Arrangement of targets is same as in previous case. A depth of 20 cm in 15% soil moisture is equivalent to 65 cm in air and hence, targets should be expected at $9^{th}$ bin. Raw B Scan (Figure 4.8 (a)) image shows a comparatively strong reflection value at downrange indexes 9 and 10 and crossrange index 16. This should be due to metal. Other targets are not visible in this image. After application of ICA (Figure 4.8 (b)) three different patches can be seen corresponding to three targets. The patches are comparatively resolvable when compared to the image in Figure 4.8 (b). This observation can be explained through dispersion. When soil moisture was 20%, there was more dispersion of EM waves. In this condition though antenna swath is same, dispersion is less and hence separation of targets can be done.

## 4.2. Imaging and Target Detection Using Hough Transform

A clutter removed B-Scan image gives probability of presence of targets. Figure 4.6 (b) showed presence of four targets when actually there were only three targets. On a moving vehicle, uniform scanning becomes difficult and such results are expected. The biggest drawback of generating such B-Scan images is that it considers that reflections are only due to targets just below the antenna. However, it may be because of any reflector that

comes in the swath of antenna. This may also result in a wrong estimate of target location.

It was proposed in the model developed for real time target detection and classification in section 3.3.5 that target detection can be done by applying back projection (section 3.3.2) on clutter removed B-Scan image followed by application of Hough transform (section 3.3.3) on this back projected image. For image detection, first a back projected image is generated (step D in the model developed) using the clutter removed B-Scan image. This gives hyperbolas in the image so generated. If we search for strongest hyperbolas, it may be possible to detect the target. By strongest hyperbola, it is implied that maximum number of non-zero points of an edge detected binary image obtained after applying Sobel operator to this back projected image pass through this hyperbola. The apex of this hyperbola gives location of targets. Hence, the second step for target detection includes applying Hough transform (step E in the model of section 3.3.5) to this back projected image to look for three strongest hyperbolas.

Velocity correction has been applied to get the location of targets at the apex of hyperbolas. Results in this section have been discussed depth wise.

### 4.2.1. For targets at depth of 10 cm

Figure 4.10 shows the results obtained when targets were buried 10 cm deep in volumetric soil moisture level of 15 %. Depth of 10 cm in soil having dielectric constant 7.70 added to 10 cm antenna-soil distance becomes equivalent to 13.6 cm. In Figure 4.9 (b), it can be seen that the apex of targets is at 12.24 cm. However, Figure 4.9 (a) show lots probable candidate hyperbolas which could have been targets, but using Hough transform makes it possible to pick the hyperbola which is strongest. As number of targets was fixed to three, top three hyperbolas have been picked from the Hough transform matrix.

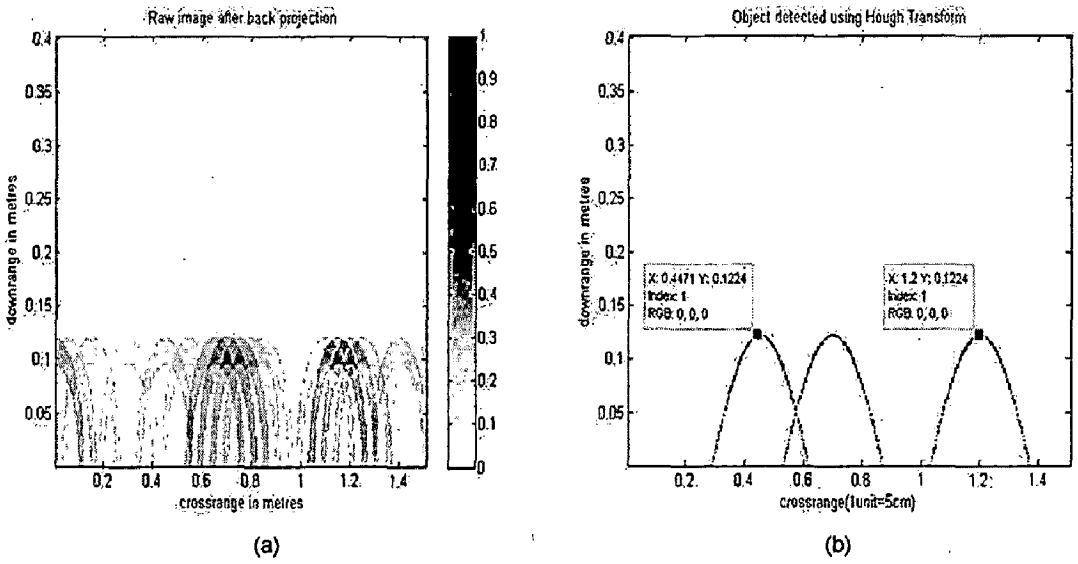


**Figure 4.9: (a) Back projected image as obtained after clutter removed B-Scan image with targets buried 10 cm deep and soil moisture 15 % (b) three targets detected by the use of Hough transform**

It has been mentioned before that for all moisture levels of soil three targets were used. At depth of 10 cm and 7% volumetric soil moisture, targets were buried in this order- metal sheet followed by cavity followed by bottle. Figure 4.10 shows the location of targets detected. In Figure 4.10 (b), three hyperbolas can be seen. But the apexes of last two hyperbolas are very close and they are likely to correspond to a single target. In Figure 4.10 (a) there is a faint hyperbola in the back projected image. This may be due to false target or clutter. A depth of 10 cm in air and 10 cm in soil, with soil having dielectric constant 4.52 is equivalent to 14.70 cm in soil. As it can be seen Figure 4.10 (b) targets are found at roughly 16 cm, which is within tolerance limit. It can also be observed from Figure 4.10 (a) that the hyperbola with highest intensity corresponds to metal sheet.

In a similar fashion, Figure 4.11 show targets detected when targets were inserted 10 cm deep in soil having volumetric soil moisture level of 20 %. Actual distance at which targets were expected to be present was 13.16 cm. Figure 4.11 (b) shows that the observed depth is in great confirmation with the expected depth. Figure 4.11 (a) shows lots of probable hyperbolas. But thresholding followed by edge detection eliminated false hyperbolas. A cursory view at Figure 4.11 (a) shows presence of two targets – air cavity and metal sheet. However application of Hough transform made it possible to search for the location of water bottle.

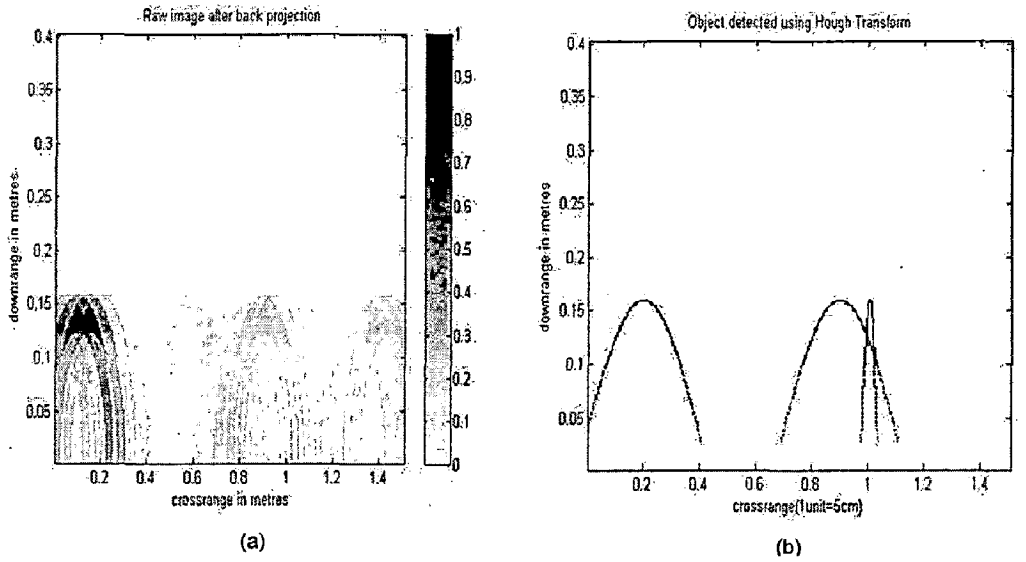


**Figure 4.10: (a) Back projected image as obtained after clutter removed B-Scan image with targets buried 10 cm deep and soil moisture 7 % (b) three targets detected by the use of Hough transform**

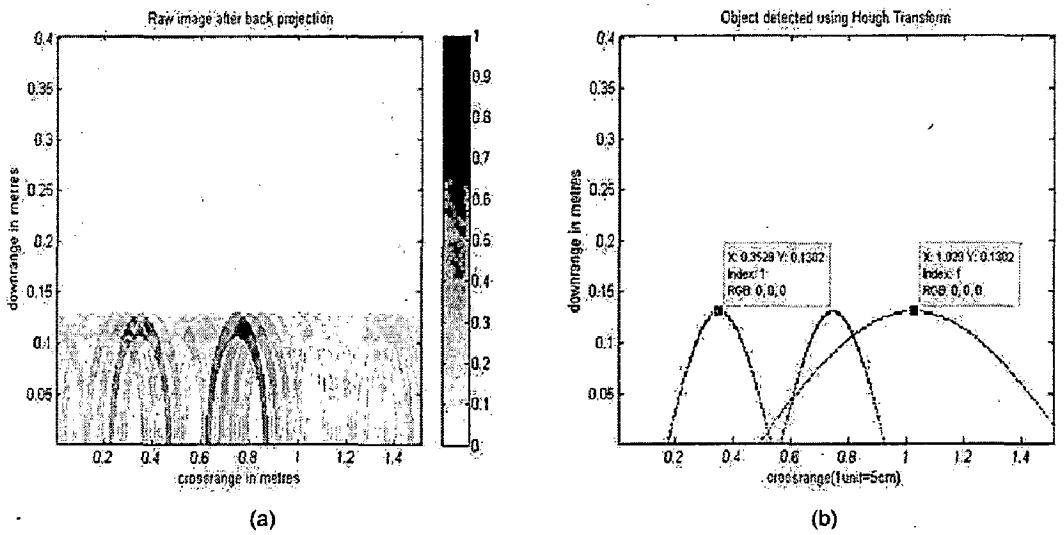


**Figure 4.11: (a) Back projected image as obtained after clutter removed B-Scan image with targets buried 10 cm deep and soil moisture 20 % (b) three targets detected by the use of Hough transform**

### 4.2.2. For targets at 15 cm

Figure 4.12 shows the results targets buried 15 cm deep and soil moisture 7 %. At this depth arrangement of targets was air cavity followed by metal sheet and in the last water bottle. Presence of hyperbola due to metal is conspicuous in Figure 4.12 (a). Other than that there are many hyperbolas, of which many are because of clutters or noise. In Figure 4.12 (b) three hyperbolas can be observed. But the separation of apexes of last two

hyperbolas is too less and it can be concluded that one target has been missed out. Failure of Hough Transform in this case can be because of the high pixel values due to metal sheet.

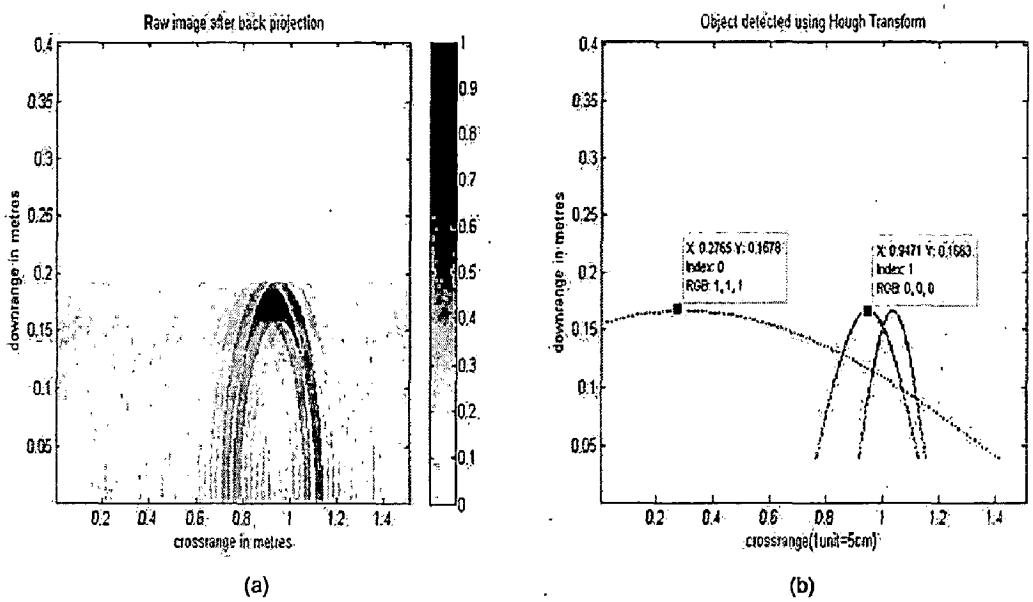


**Figure 4.12: (a) Back projected image as obtained after clutter removed B-Scan image with targets buried 15 cm deep and soil moisture 7 % (b) three targets detected by the use of Hough transform**

Figure 4.13 shows the results of target detection when targets were buried at 15 cm and soil moisture level was 15 % and 20 % respectively. It can be seen that three targets have been detected using Hough transform in both of these cases. In Figure 4.13 (c), presence of metal is conspicuous by high pixel values in the image matrix. For Figure 4.13 (d) we can see that apexes of first two hyperbolas are too close. Hence, it can be inferred that both of them are due to same target and first target i.e. air cavity was not detected.

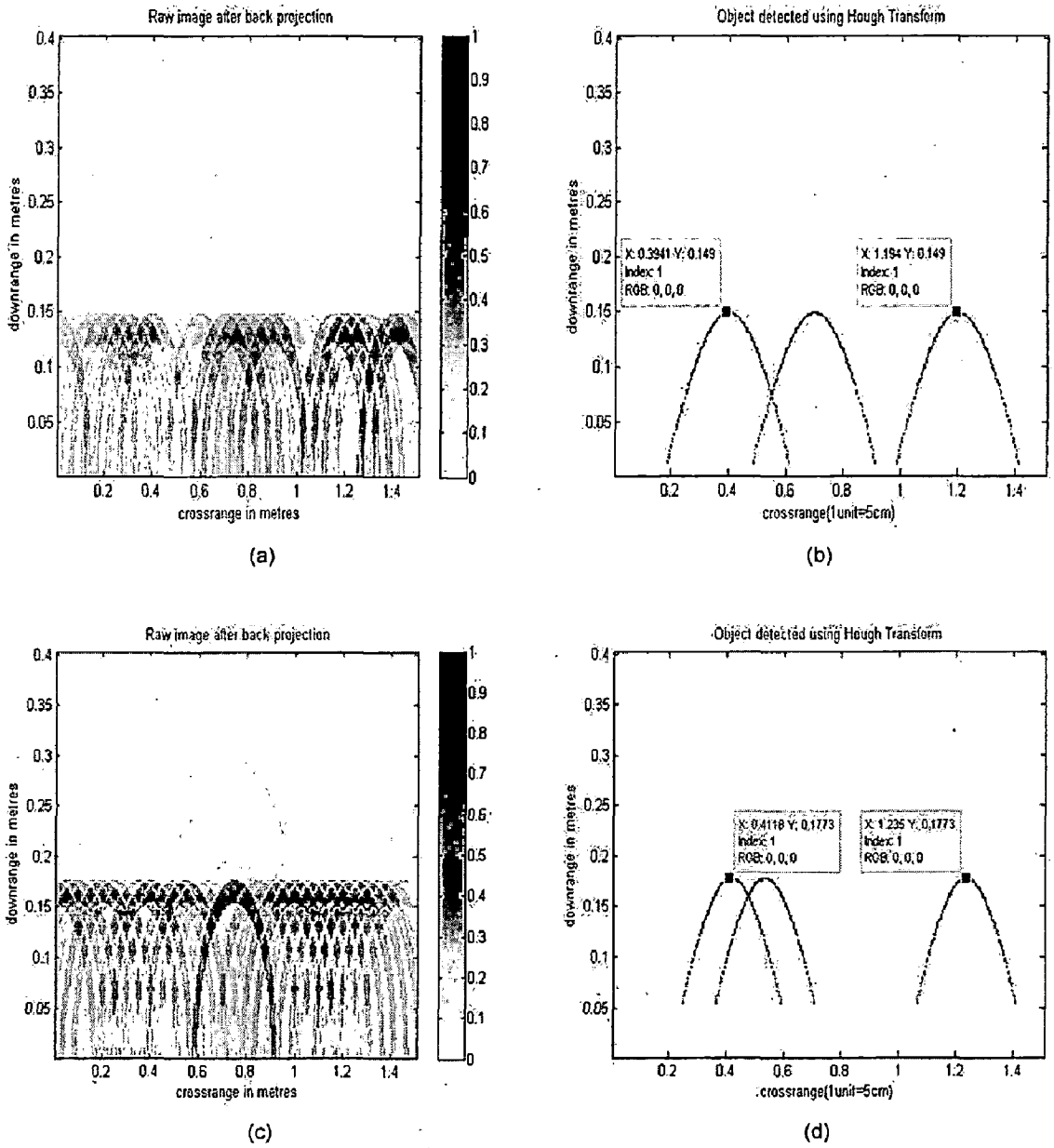


**Figure 4.13: (a) Back projected image as obtained after clutter removed B-Scan image with targets buried 15 cm deep and soil moisture 15 % (b) three targets detected by the use of Hough transform (c) Back projected image as obtained after clutter removed B-Scan image with targets buried 15 cm deep and soil moisture 20 % (d) three targets detected by the use of Hough transform**

### 4.2.3. For Targets at 20 cm

Similarly target detection results were obtained for targets at 20 cm depth. Results have been shown in Figure 4.14 for all moisture levels of soil.

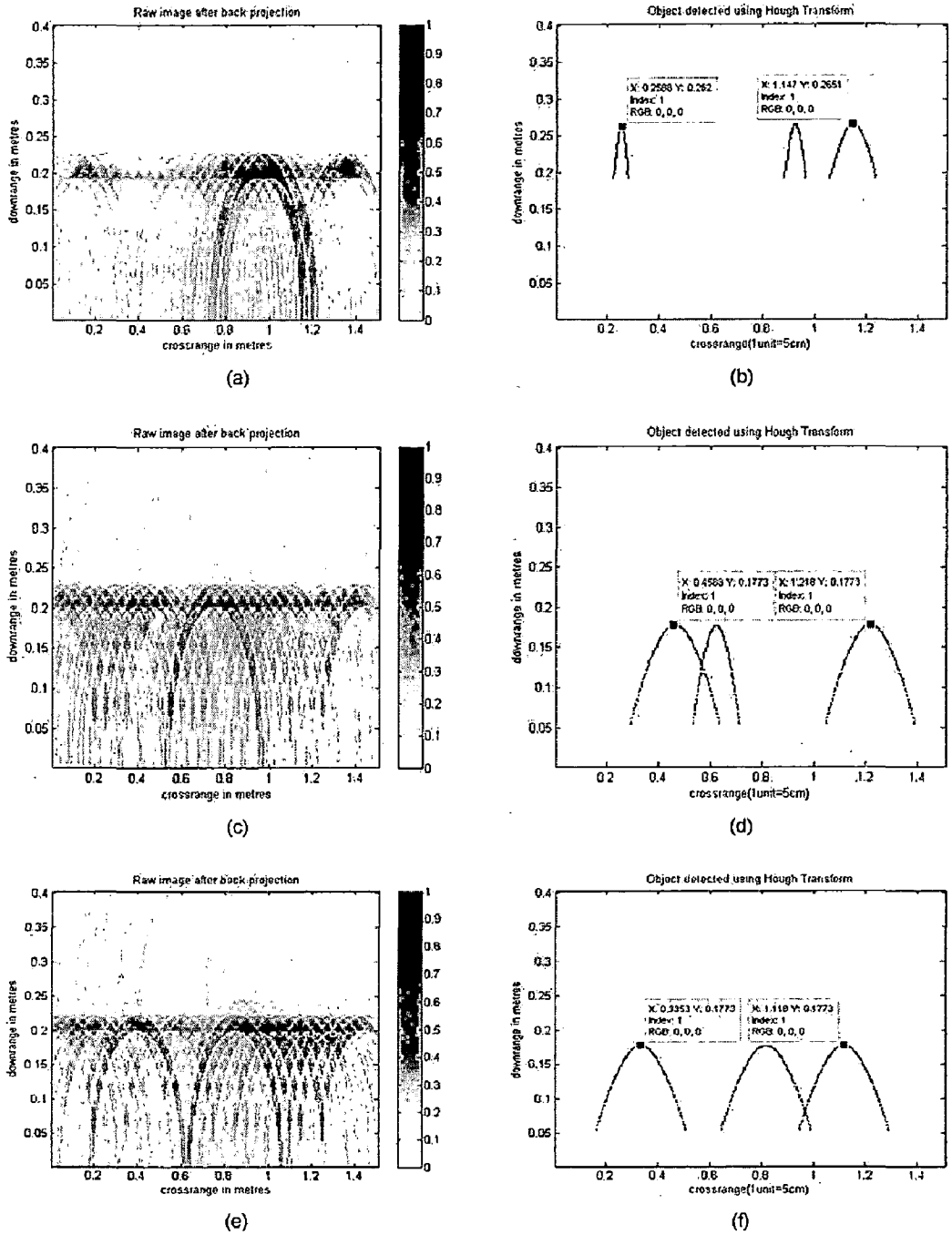


**Figure 4.14: (a) Back projected image for targets 20 cm deep, soil moisture 7 % (b) Detection of targets using Hough Transform (c) Back projected image for targets 20 cm deep, soil moisture 15 % (b) Detection of targets using Hough Transform (a) Back projected image for targets 20 cm deep, soil moisture 20 % (b) Detection of targets using Hough Transform**

It can be seen that in Figure 4.14 (d) apexes of two of the hyperbolas are very close and they represent same target. Hence, one of the targets has been missed. The main reason of failure of Hough transform in some of the cases is attributed to the fact that target detection using Hough transform is unsupervised. It just looks for strong hyperbolas

which largely depend upon the density of non-zero pixels in edge detected binary image. Naturally, targets having stronger reflection values will have corresponding to them a number of non-zero pixels in the edge detected binary image. Also, the programme searches for only top three hyperbolas, so chances are there that some of the target would get missed.

## 4.3. Target Classification by Target Spectra

After presence of targets has been detected, task of target classification remains to be done. Spectra of targets were generated (step F in the model developed) at the depth they were expected to be by the method that has been explained in section 3.3.4. Results obtained have been given in this section.

### 4.3.1. Depth-wise comparison of spectra for pair of same targets

Before this classification technique is used it is important to observe the invariability of target spectra under various conditions. This section deals with making comparison between spectra of same type of targets when they are buried at different depths. Figure 4.15 shows the spectra of different targets for soil moisture level 15 % at depths of 10 cm and 15 cm.

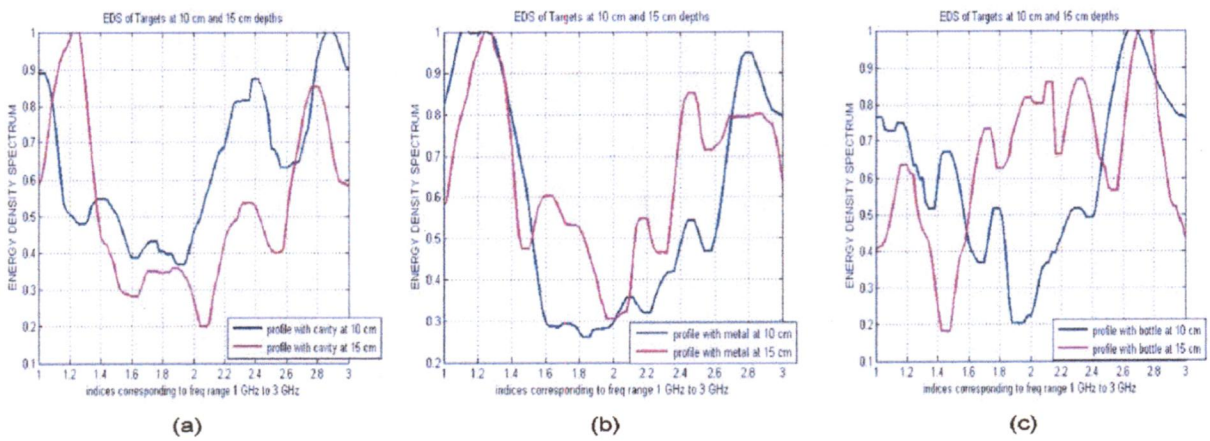


**Figure 4.15: Comparison of EDS of targets at 10 cm and 15 cm at soil moisture level 15 % for (a) Air Cavity, (b) Metal Sheet, (c) Water Bottle**

The spectra of targets at different depths can be compared here. For air cavity and metal sheet the spectra have been almost depth invariant it has changed a lot in the case of

water bottle. The reason can be weak reflections due to the cylindrical shaped water bottle. It is possible that its spectrum is influenced by the presence of clutters as the burial depth increases.

Pearson's correlation coefficient was found for these spectra to evaluate the similarity between them. Table 4.1 shows the values of correlation coefficient for the pair of spectra as shown above. Correlation coefficient has been evaluated for four bands of frequency by splitting the 2 GHz bandwidth into bands of 0.5 GHz. This was done so as to compensate for the spectral variation at higher frequency values due to attenuation.

**Table 4.1: Pearson's correlation coefficient values for different targets at 10 cm and 15 cm with soil moisture 15 %**

| | Pearson's Correlation Coefficient Values | | | |
|---|---|---|---|---|
| | **1-1.5 GHz** | **1.5- 2.0 GHz** | **2.0-2.5 GHz** | **2.5-3.0 GHz** |
| **Air Cavity** | -0.1488 | -0.1535 | 0.9384 | 0.4967 |
| **Metal Sheet** | 0.8678 | 0.1044 | 0.8708 | 0.6803 |
| **Water Bottle** | 0.2326 | -0.8490 | -0.4711 | -0.8471 |

The coloured cells show a great correlation coefficient in that particular frequency band. It is observed that metal sheet shows great correlation in three our four bands, while cavity shows a good correlation only in third band which is from 2.0 GHz to 2.5 GHz. For bottle, spectra are uncorrelated in all the frequency bands of observation.

### 4.3.2. Moisture- wise comparison of spectra for pair of same target

The next analysis would be effect of increasing moisture on target spectra. Comparison of spectra was done for targets buried at same depth but under different moisture level of soil. Figure 4.16 shows the same. For this case also, it is observed that spectral variations with soil moisture level are not that much pronounced for air cavity and metal sheet. But the change in EDS is drastic for water bottle. Contrary to the expectation there are strong reflections at several points while with increase in moisture attenuation should have suppressed them. Table 4.2 makes the comparison between the spectra based on correlation coefficient values.

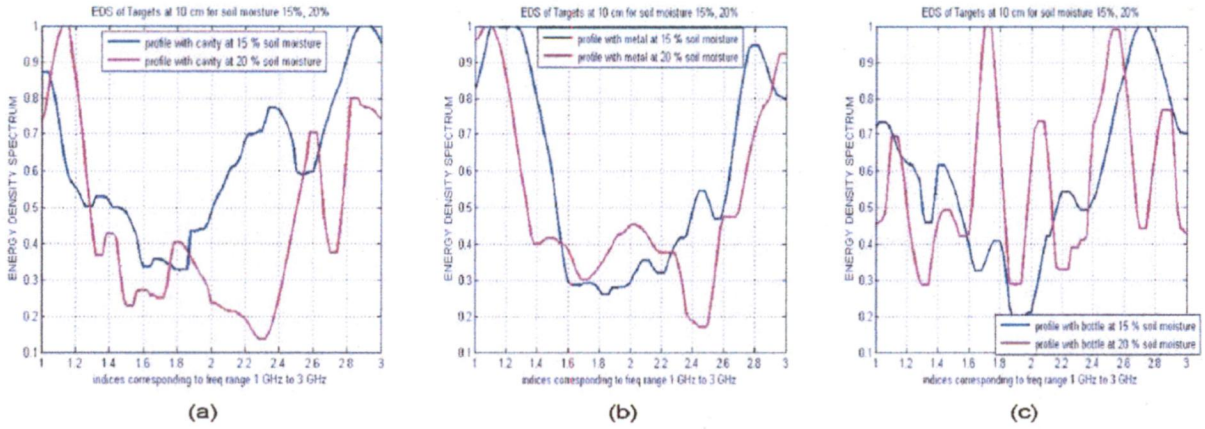


**Figure 4.16: Comparison of spectra of targets at 10 cm with soil moisture level 15% and 20 % for (a) Air Cavity (b) Metal Sheet (c) Water Bottle**

**Table 4.2: Pearson's correlation coefficient values for different targets at 10 cm with soil moisture 15 % and 20 %**

| | Pearson's Correlation Coefficient Values | | | |
|---|---|---|---|---|
| | 1-1.5 GHz | 1.5- 2.0 GHz | 2.0-2.5 GHz | 2.5-3.0 GHz |
| Air Cavity | 0.6052 | -0.3860 | -0.0726 | 0.4742 |
| Metal Sheet | 0.6214 | 0.3445 | -0.9232 | 0.7639 |
| Water Bottle | 0.6654 | -0.3860 | -0.0726 | 0.4742 |

It can be seen that first band shows great correlation for same type of targets for different levels of soil moisture. But, after 1.5 GHz, spectra changes considerably.

### 4.3.3. Target-wise comparison of spectra

Now comparison between spectra of different targets will be made so as to know how much they are capable to classify the targets. Figure 4.17 shows spectra for targets which are at same depth and under same moisture level of soil. For same targets, different look positions were used to make comparisons. As EDS is sensitive to moisture and depth, slight changes in the spectrum is expected. However, changes should not be drastic so that classification techniques can be used. As it can be seen that spectra of same targets specially air cavity and metal sheet have resemblance and spectra of different targets differ a lot. It can also be observed that spectra of bottle is a bit sensitive as it changes a significantly with different look positions. Values of correlation coefficient for these spectra in four frequency bands have been given in Table 4.3.

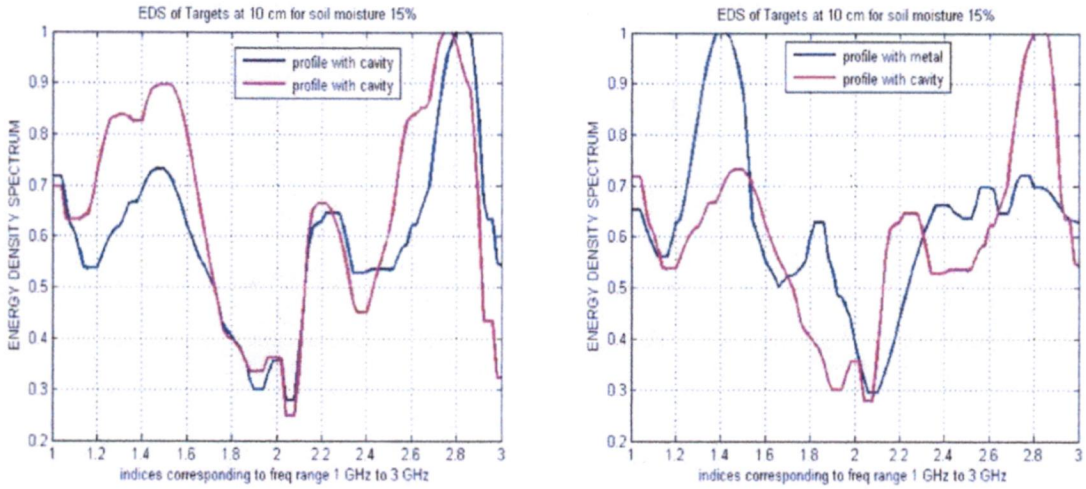


(a)Cavity with Cavity




(b) Cavity with Metal

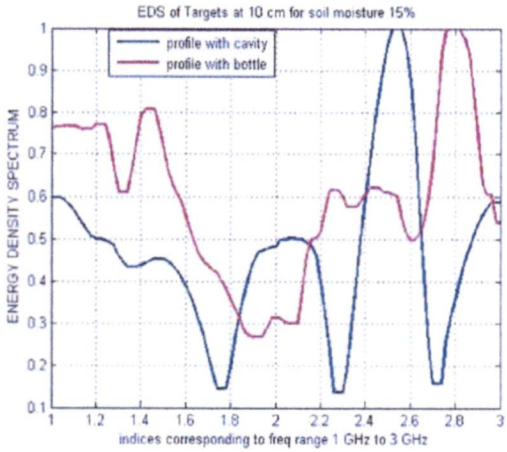


(c)Cavity with Bottle

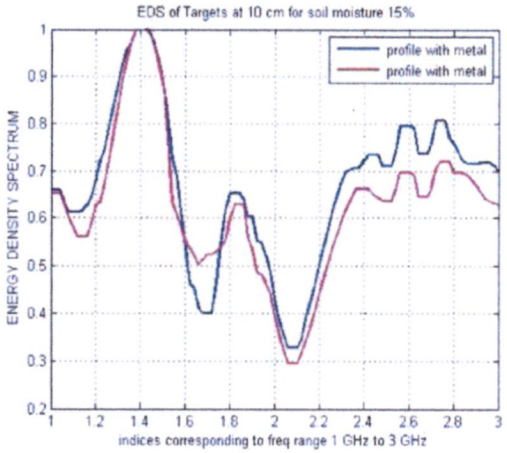


(d) Metal with Metal

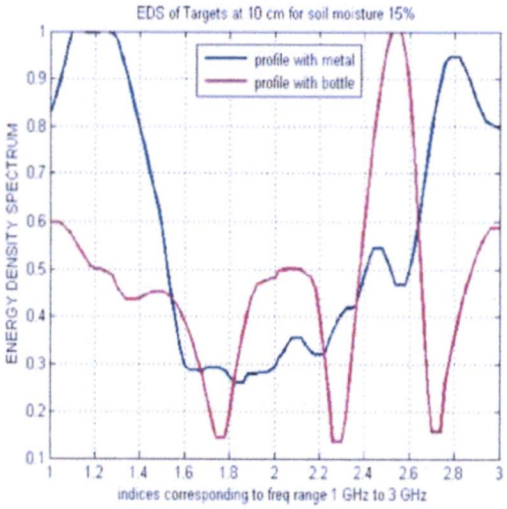


(e) Metal with Bottle

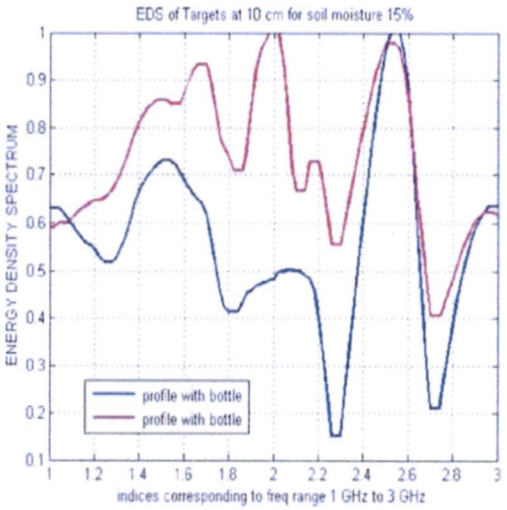


(d) Bottle with bottle

**Figure 4.17: Comparison of spectra of targets with each other at burial depth 10 cm and soil moisture 15 %**

**Table 4.3: Correlation coefficient values for different pair of targets at 10 cm with soil moisture 15 %**

| | Pearson's Correlation Coefficient Values | | | |
|---|---|---|---|---|
| | 1-1.5 GHz | 1.5- 2.0 GHz | 2.0-2.5 GHz | 2.5-3.0 GHz |
| **Air Cavity- Air Cavity** | 0.8260 | 0.9780 | 0.9690 | 0.7820 |
| **Air Cavity- Metal Sheet** | 0.6338 | 0.5513 | 0.5323 | 0.6693 |
| **Air Cavity-Water Bottle** | 0.3311 | 0.0929 | -0.0824 | 0.6069 |
| **Metal sheet- Metal sheet** | 0.9888 | 0.8459 | 0.9963 | 0.7442 |
| **Metal sheet- Water Bottle** | 0.3484 | 0.3552 | 0.5433 | -0.8292 |
| **Water Bottle- Water Bottle** | 0.6338 | 0.5513 | 0.5323 | 0.6693 |

From correlation coefficient values so observed it can be concluded that while air cavity and metal sheet are recognizable through their spectra, same is not true for water bottle. Given the inconsistency of correlation coefficient values, neural network was opted for target classification. The neural network was trained with 30 spectra of targets at different depths and at different moisture levels of soil. For each target there were 10 spectra to train the neural network. Spectra for targets at 12 cm with soil moisture level 17 % were passed to the neural networks for target classification and satisfactory results were obtained. Metal was clearly classified by the network but, there were some ambiguities observed between cavity and water bottle.

## 4.4. Contextual Masking for Successive Classification of Targets

Reflected signal strength of targets can also be used to classify targets. In his dissertation, Jain found our that at all moisture levels of sand and at all depths reflected signal strength of metal was highest, followed by air cavity and the least reflected signal strength was that of water bottle. Keeping this in mind, contextual masking for successive classification of targets was used for detection of targets (step G in the model developed).

Clutter removed B-Scan image was generated using ICA clutter removal technique, and then the image pixel values were normalized. It was assumed that highest signal value was due to reflection from metal sheet and pixels around the highest valued pixel were masked. The image was normalized again and then the highest valued pixel was found. It was taken to be air cavity. Pixels were masked as before and image was normalized

again. The image was left with pixels corresponding to water bottle. Hence, all the three targets were identified. Step by step treatment of B-Scan image for target classification has been shown by Figure 4.18 for the case when targets were buried at 10 cm depth and soil moisture 15 %.

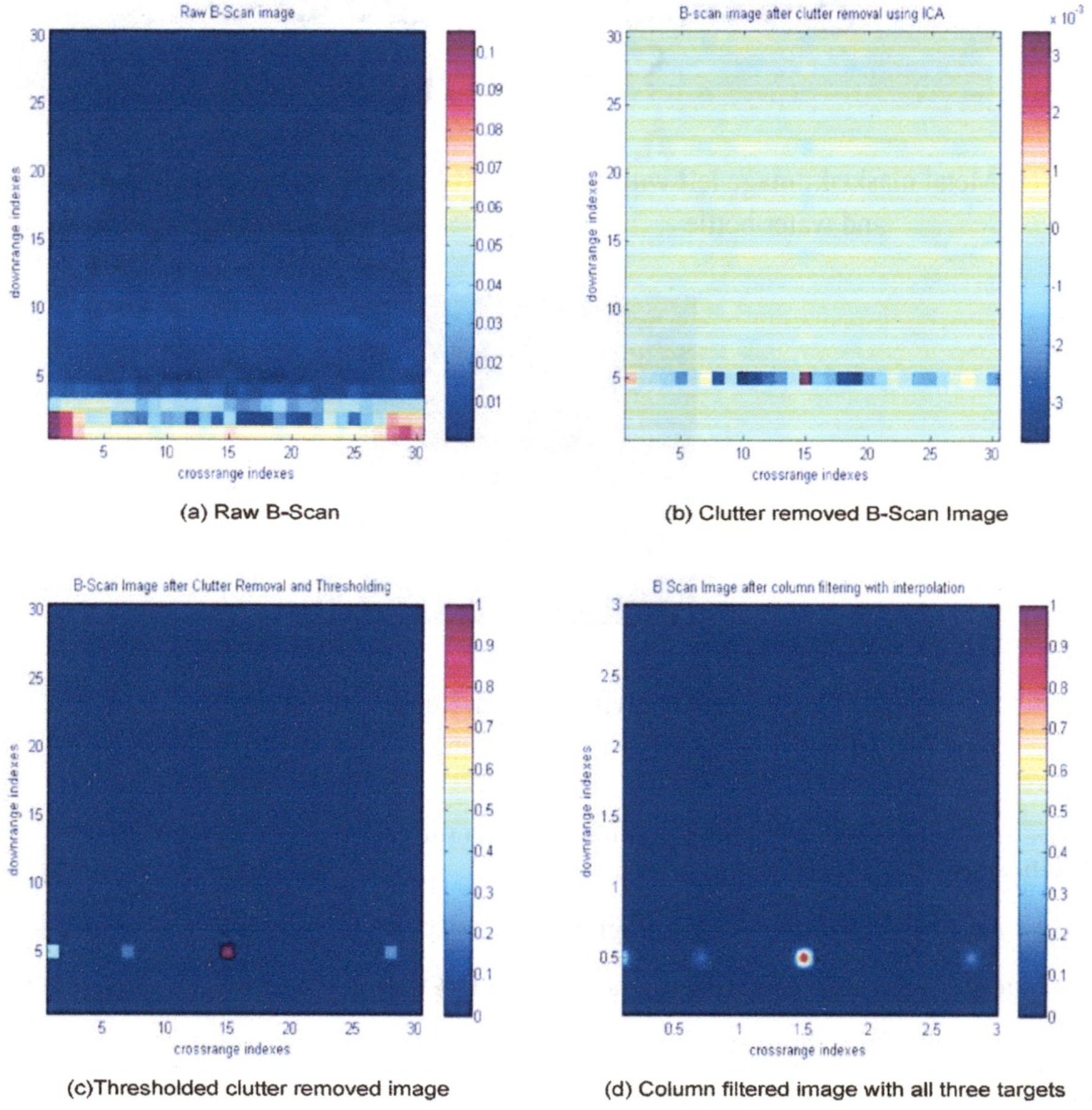


**Figure 4.18: First four steps involved in contextual masking of targets**

First, using ICA clutter removal technique, thresholding and column filtering all the targets were located in the B-Scan image. Figure 4.18 (d) shows presence of four targets. One of them has to be false target as only 3 targets were used. Results obtained after contextual masking have been shown in Figure 4.19.

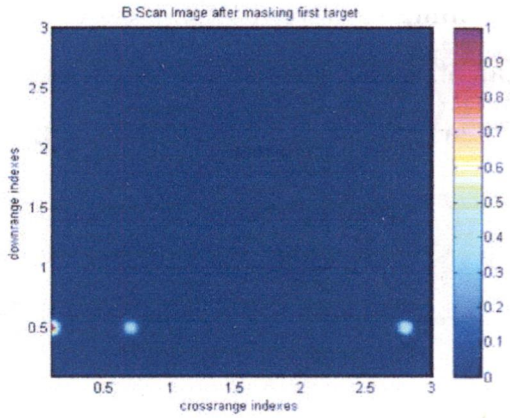


(a) Metal masked, Image left with cavity and water bottle

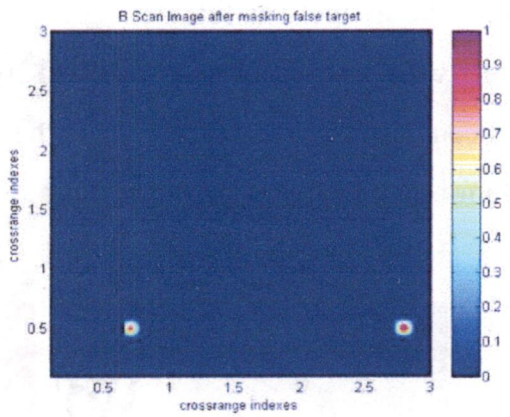


(b) False target masked, Image left with water bottle and cavity

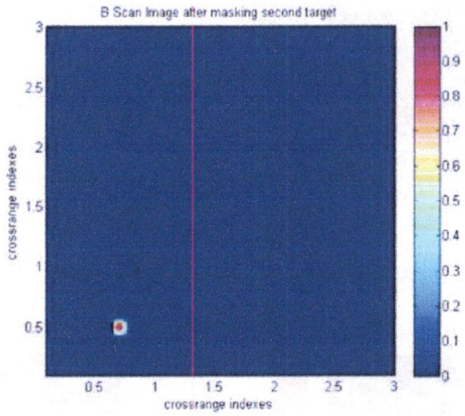


(c)Air cavity masked, Image left with water bottle

**Figure 4.19: Images showing masking of metal sheet, false target and air cavity for target classification**

Pixels around the pixel having highest intensity were masked. These masked pixels corresponded to metal sheet. The resultant image was normalized and the image was left with 3 dots showing three strong reflections. The dot at the leftmost end of the image can be due to clutter or some medium change. After it has been masked, the image is left with presence of air cavity and water bottle. Then the next pixels having higher pixel values are searched. This corresponds to air cavity. It is masked and the image is left with water bottle. Thus, we see how targets can be successively classified by contextual masking. Similarly, target classification was done for other B-Scans as well.

# Chapter 5. Concluding Remarks and Future Scope

## 5.1. Conclusions

Based on the work done so far following conclusions can be drawn:

1. In cluttered environment, target detection and target classification is a challenging job and this dissertation dealt with the same problems.
2. For detection of target using A-Scan various Hamming window filtering and median filtering techniques were used. It was found that, though median filtering combats abrupt noise very well, it may sometime consider reflections due to target as noise and may eliminate them. In the range profile obtained after median filtering, locating target was difficult. Hence, Hamming window filtering was used. This combats noise and preserves important information as well.
3. ICA clutter removal technique was used to locate targets. Other clutter removal techniques like PCA and SVD weren't used as they remove only clutters and reflection values due to targets, being very feeble in moist soil, may get eliminated as clutters. ICA finds statistically independent components and hence, it was possible to find targets using ICA. It was also found that dispersion played and important role in differentiating the location of targets e.g. targets weren't differentiated when targets were buried at 20 cm depth in soil moisture 20%.
4. Back projection was applied on clutter removed image which gave hyperbolas corresponding to probable targets. Hough transform was used to locate targets. Being unsupervised, Hough transform has this drawback of giving multiple hyperbolas corresponding to a single target. For example, in some cases it was found that there were two hyperbolas due to metal sheet. However, overall performance of Hough Transform in finding targets was satisfactory.
5. Neural networks and correlation coefficient between EDS of different targets at different moisture level was used to classify targets. Sensitivity of EDS towards burial depth of target and soil moisture level was a major challenge. But use of neural networks made it possible to combat it and targets were classified using neural networks for pattern classification on Energy density Spectra of targets.

6. Contextual masking for successive target detection was also used successfully for target classification. Results deteriorate if scanning is done in such a way that a strong reflector is far from the scanner and weak reflector is near to it.
7. A real time system was developed which can be used for target detection and classification in real time.

## 5.2. Future Scope

Target detection and classification is a very vibrant field as far as GPR is concerned. For target detection statistical measure of various targets and clutters can be used. Genetic algorithm can also be used to find strong hyperbolas to give a more accurate location of targets.

For target classification parameters which are invariant to burial depth or soil moisture level need to be implemented to make the system more reliable. Time frequency analysis can be used for this purpose. Phase information gets almost lost in the data processing algorithms employed in this work. Using phase information can give better results and future work can make use of this.

## References


[1] Parrini, F., Pieraccini, M., Atzeni, C., "A high-speed continuous wave GPR." *Proceedings of the Tenth International Conference on Ground Penetrating Radar,* vol.1, pp. 183- 186, 2004.

[2] Langman, A., Dimaio, S.P., Burns, B.E., Inggs, M.R., "Development of a low cost SFCW ground penetrating radar." *International Geoscience and Remote Sensing Symposium*, vol. 4, pp. 2020-2022, 1996.

[3] Conyers, L.B., "Moisture and soil differences as related to the spatial accuracy of GPR amplitude maps at two archaeological test sites." *Proceedings of the Tenth International Conference on Ground Penetrating Radar*, pp. 435- 438, 2004.

[4] Langman, A., Inggs, M.R., "A 1-2 GHz SFCW radar for landmine detection." *Proceedings of the 1998 South African Symposium on Communications and Signal Processing,* pp. 453-454, 1998.

[5] Rappaport, C.M., "Soil Moisture and Surface Roughness Effects in Ground Penetrating Radar Detection of Land Mines." *IEEE MTT-S International Microwave Symposium Digest,* pp. 280-283, 2006.

[6] Lambot, S., Slob, E.C., van den Bosch, I., Stockbroeckx, B., Scheers, B., Vanclooster, M., "GPR design and modeling for identifying the shallow subsurface dielectric properties." *Proceedings of the 2nd International Workshop on Advanced Ground Penetrating Radar*, pp. 130- 135, 2003.

[7] Morrow, I.L., van Genderen, P., "Effective imaging of buried dielectric objects." *IEEE Transactions on Geoscience and Remote Sensing,* vol. 40, no. 4, pp. 943-949, 2002.

[8] Ozdemir, C., and Ling, H., "An experimental investigation of buried-object imaging in a homogeneous medium using synthetic-aperture radar concepts." *Microwave and Optical Technology Letters*, pp. 1209-1214, 2006.

[9] Panzner, Berthold, Jostingmeier, Andreas, Omar, Abbas, "Radar signatures of complex buried objects in ground penetrating radar." *11th International Radar Symposium (IRS), 2010*, pp. 1-4, 2010.

[10] Hamran, S., Langley, K., "A 5.3 GHz step-frequency GPR for glacier surface characterization." *Proceedings of the Tenth International Conference on Ground Penetrating Radar*, pp. 761- 764, 2004.

[11] van Genderen, P., "Multi-waveform SFCW radar." *33rd European Microwave Conference*, vol. 2, pp. 849- 852, 2003.

[12] Antoine, M., Gregoire, M., Vanclooster, M., Lambot, S., Slob, E.C., van den Bosch, I., "Modeling of GPR signal and inversion for identifying the subsurface dielectric properties frequency dependence and effect of soil roughness." *Proceedings of the Tenth International Conference on Ground Penetrating Radar, 2004*, vol. 1, pp. 79- 82, 2004.

[13] Lambot, S., Slob, E.C., van den Bosch, I., Stockbroeckx, B., Vanclooster, M., "Modeling of ground-penetrating Radar for accurate characterization of subsurface electric properties." *IEEE Transactions on Geoscience and Remote Sensing*, vol. 42, no. 11, pp. 2555- 2568, 2004.

[14] Kong, L.J., Zhao, B., Cui, G.L., "Sidelobe suppression method for stepped frequency continuous-wave radar." *Electronics Letters*, vol. 47, no. 7, pp. 460-462, 2011.

[15] van Genderen, P., Nicolaescu, I., "Imaging of stepped frequency continuous wave GPR data using the Yule-Walker parametric method." *European Radar Conference*, pp. 77-80, 2005.

[16] Shanker Man Shrestha, Arai, I., Tomizawa, Y., "Landmine detection with GPR using super resolution signal processing algorithm." *Proceedings of the Tenth International Conference on Ground Penetrating Radar*, pp. 705- 708, 2004.

[17] Zhao, Anxing, Jiang, Yansheng, and Wang Wenbing, "Signal-to-Noise Ratio Enhancement in Multichannel GPR Data via the Karhunen-Loeve Transform." *PIERS Online*, vol. 1, no. 6, 754-757, 2005.

[18] Rennie, C., Arendse, B., Inggs, M.R., Langman, A., "Practical measurements of landmine stimulants using a SFCW radar, a pulse induction metal detector and an infrared camera." *Second International Conference on the Detection of Abandoned Land Mines,* pp. 182-186, 1998.

[19] Scheiblhofer, S., Schuster, S., Stelzer, A., "High-Speed FMCW Radar Frequency Synthesizer With DDS Based Linearization." *IEEE Microwave and Wireless Components Letters,* vol. 17, no. 5, pp. 397-399, 2007.

[20] Farmer, G.A., Cuthbert, L.G., Olver, A.D., Botros, A.Z., "Distinguishing between types of hidden objects using an FMCW radar." *Electronics Letters* , vol. 20, no. 20, pp. 824-825, 1984.

[21] Alberti, G., Ciofaniello, L., Della Noce, M., Esposito, S., Galiero, G., Persico, R., Sacchettino, M., Vetrella, S., "A stepped frequency GPR system for underground prospecting." *Annals Of Geophysics,* vol. 45, no. 2, pp. 375-391, 2002.

[22] Jain, Maulik, "Critical Analysis of SFCW-GPR Data for Target Detection and Identification." M.Tech Thesis, Dept. of Electronics and Computer Engineering, IIT Roorkee, India, 2010.

[23] Chandra, R., "Study Of Through Wall Imaging In Uwb Range For Target Detection," M.Tech Thesis, Dept. of Electronics and Computer Engineering, IIT Roorkee, India, 2008.

[24] Verma, P. K., Gaikwad, A. N., Singh, D. , Nigam, M. J., "Analysis of Clutter Reduction Techniques for Through Wall Imaging in UWB Range." *Progress in Electromagnetics Research B,* vol. 17, pp. 29-48, 2009.

[25] Gurbuz, A.C., McClellan, J.H., Scott, W.R., "GPR Imaging Using Compressed Measurements." *IEEE International Geoscience and Remote Sensing Symposium,* vol. 2, pp. II-13-II-16, 2008.

[26] Luo, Mei-fang, Kong, Ling-jiang, Cui, Guo-long, "A sidelobe suppression method based on adaptive pulse compression (apc) for random stepped-frequency radar." *IET International Radar Conference,* pp.1-4, 2009.

[27] Muqaibel, A., Safaai-Jazi, A., Bayram, A., Attiya, A.M., Riad, S.M., "Ultrawideband through-the-wall propagation." *IEE Proceedings Microwaves, Antennas and Propagation,* pp. 581- 588, 2005.

[28] Liu, Xiaoxiang, Leung, Henry, "Clutter Suppression in GPR Using Chaos Modulation." *International Radar Symposium,* pp.1-4, 2006.

[29] Dobrotin, Nikita, Levitas, Boris, "GPR resolution improvement." *11th International Radar Symposium (IRS),* pp.1-3, 2010.

[30] Zhao, Anxing, Jiang, Yansheng, and Wang Wenbing, "Exploring Independent Component Analysis for GPR Signal Processing." *PIERS Online*, vol. 1, no. 6, 750-753, 2005.

[31] Delac, K., Grgic, M., and Grgic, S., "Independent comparative study of PCA, ICA, and LDA on the FERET data set." *International Journal of Imaging Systems and Technology*, vol. 15, pp. 252–260, 2005.

[32] Hyvärinen, A, "Survey on Independent Component Analysis." *Neural Computing Surveys* vol. 2, pp. 94--128, 1999.

[33] Guolong Cui, Lingjiang Kong, Jianyu Yang, "A Back-projection algorithm to stepped-frequency synthetic aperture through-the-wall radar imaging." *1st Asian and Pacific Conference on Synthetic Aperture Radar*, pp. 123-126, 2007.

[34] Zhou, L., Su, Y., "A GPR imaging algorithm with artifacts suppression." *13th International Conference on Ground Penetrating Radar,* pp. 1-7, 2010.

[35] Wentai Lei, Yi Su, Chun Lin Huang, "A TAM-BP imaging algorithm in GPR application." *International Conference on Microwave and Millimeter Wave Technology,* pp. 619- 621, 2004.

[36] Zhang, Y, "Optimisation Of Building Detection In Satellite Images By Combining Multispectral Classification And Texture Filtering." *Journal of Photogrammetry and Remote Sensing*, pp 50-60, 1999.

[37] Teoh, K.K. , Ibrahim, H. , Bejo, S.K., "Investigation On Several Basic Interpolation Methods For The Use In Remote Sensing Applications." *IEEE Conference on Innovative Techniques in Intelligent Systems and Industrial Appliances*, pp. 60-65, 2008.

[38] Yigit, E., Demirci, S., Ozdemir, C., "On the imaging applications of ground penetrating radar." *URSI International Symposium on Electromagnetic Theory (EMTS)*, pp. 253-256, 2010.

[39] Liu, Yayu, Wang, Meiqing, Cai, Qiurong, "The target detection for GPR images based on curve fitting." *3rd International Congress on Image and Signal Processing (CISP), 2010,* vol. 6, pp. 2876-2879, 2010.

[40] Pasolli, E., Melgani, F., Donelli, M., "Gaussian Process Approach to Buried Object Size Estimation in GPR Images." *IEEE Geoscience and Remote Sensing Letters*, vol. 7, no. 1, pp. 141-145, 2010.

[41] Debes, C., Amin, M.G., Zoubir, A.M., "Target Detection in Single- and Multiple-View Through-the-Wall Radar Imaging." *IEEE Transactions on Geoscience and Remote Sensing,* , vol. 47, no. 5, pp.1349-1361, 2009.

[42] Al-Nuaimy, W, Huang, Y, Nakhkash, M, Fang, M. T. C., Nguyen, V. T., Eriksen, A., "Automatic detection of buried utilities and solid objects with GPR using neural networks and pattern recognition." *Journal of Applied Geophysics*, vol. 43, no. 2, pp. 157-165, 2000.

[43] Ho, K.C., Carin, L., Gader, P.D., Wilson, J.N., "An Investigation of Using the Spectral Characteristics From Ground Penetrating Radar for Landmine/Clutter Discrimination." *IEEE Transactions on Geoscience and Remote Sensing,* vol.46, no.4, pp.1177-1191, 2008.

[44] Gader, P., Wen-Hsiung Lee, Wilson, J.N., "Detecting landmines with ground-penetrating radar using feature-based rules, order statistics, and adaptive whitening." *IEEE Transactions on Geoscience and Remote Sensing,* vol. 42, no. 11, pp. 2522- 2534, 2004.

[45] Daniels, D.J., Curtis, P., Lockwood, O., "Classification of landmines using GPR." *IEEE Radar Conference.* pp. 1-6, 2008.

[46] dos Santos, V.R.N., Porsani, J.L., Hirata, N.S.T., "Automatic classification of metallic targets using pattern recognition of GPR reflection: a study in the IAG-USP Test Site, Sao Paulo (Brazil)." *13th International Conference on Ground Penetrating Radar (GPR),* 2010.

[47] Strifors, H.C., Gustafsson, A., Abrahamson, S., Gaunaurd, G.C., "Fuzzy-cluster representation of time-frequency signatures as a means for automatic classification of buried mine-like targets." *Proceedings of the IEEE-SP International Symposium on Time-Frequency and Time-Scale Analysis,* pp. 597-600, 1998.

[48] Sun, Y., Li, J., "Time-frequency analysis for plastic landmine detection via forward-looking ground penetrating radar." *IEE Proceedings- Radar, Sonar and Navigation,* vol. 150, no. 4, pp. 253-61, 2003.

[49] Sugak, V.G., Sugak, A.V., "Phase spectrum of signals in ground Penetrating Radar applications." *IEEE Radar Conference,* pp.1-5, 2009.

[50] Hajnsek, Irena, "Inversion of Surface Parameters Using Polarimetric SAR." PhD Thesis, Institut fur Hochfrequenztechnik und Radarsysteme Oberpfaffenhofen, Germany, 2001.

[51] Manual, Rohde & Schwarz R&S®FSH4/FSH8 Spectrum Analyzer, Version 04.03, June 2010.

[52] Manual, Rohde & Schwarz R&S® HF-906.

[53] Yelf, R., "Where is true time zero ?" *Proceedings of the Tenth International Conference on Ground Penetrating Radar, 2004. GPR 2004,* vol. 1, pp. 279- 282, 2004.

[54] Internet: http://www.mathworks.com/help/toolbox/images/ref/medfilt2.html.

[55] Gauthier, Sylvain S., Chamma, Walid, "Surveillance through concrete walls." Sensors, and Command, Control, Communications, and Intelligence (C3I)

Technologies for Homeland Defense III, Defence Research and Development Canada, 2003.

[56] Gonzalez, Rafael C., Woods, Richard E., Eddins, Steven L., *Digital Image Processing Using MATLAB,* Pearson Education (Singapore) Pvt. Ltd., Third Edition, 2005.

[57] Internet: http://www.dtreg.com/pnn.htm.

# APPENDIX

## a) Target detection and classification when targets were buried at 10 cm depth and soil moisture was 20 %

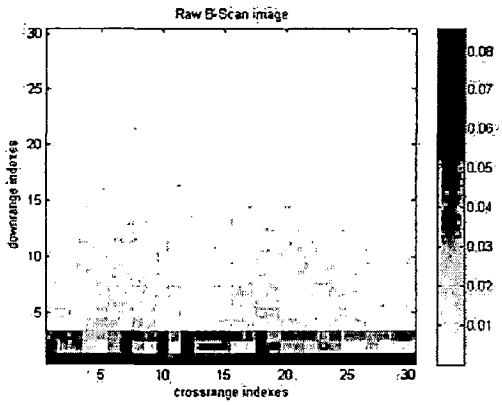


(a) Raw B-Scan Image

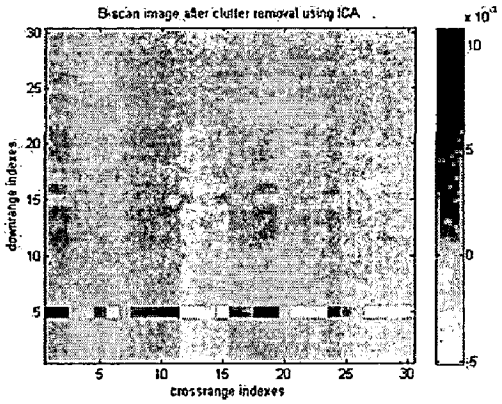


(b) B-Scan after ICA clutter removal

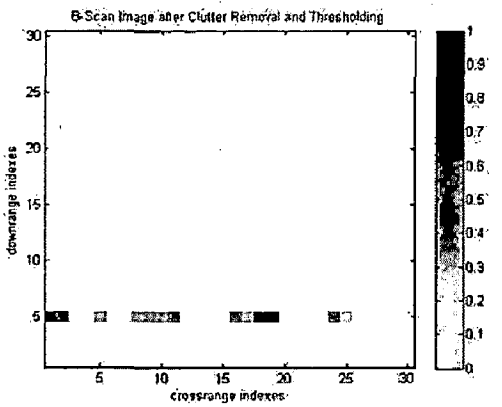


(c)B-Scan after thresholding

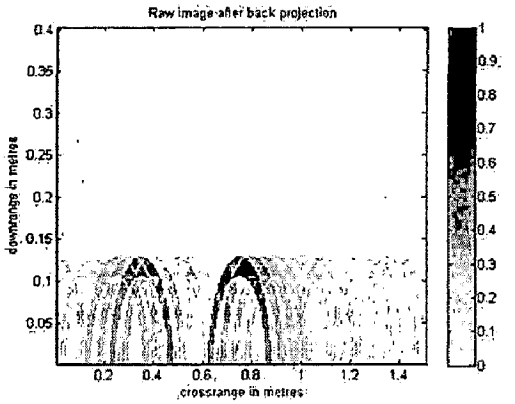


(d)Back projected image

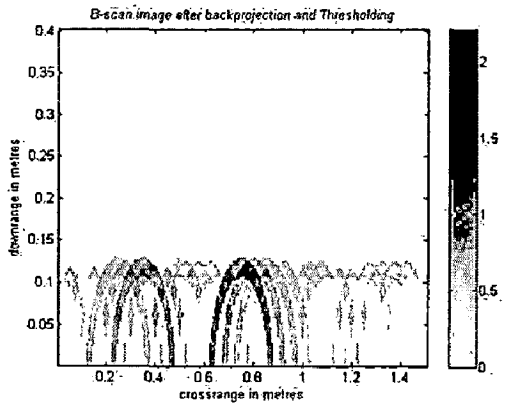


(e)Back projected and thresholded

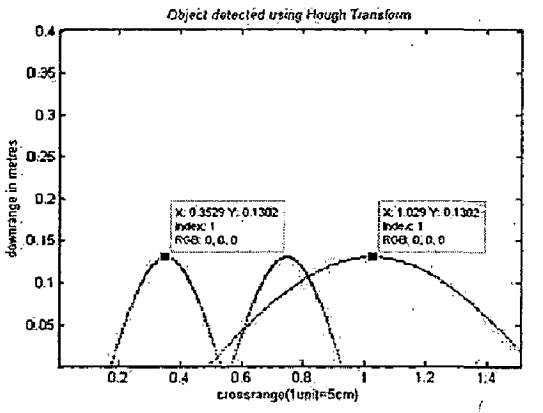


(f)Targets detected after Hough transform

**Figure 1: Steps involved in target detection**

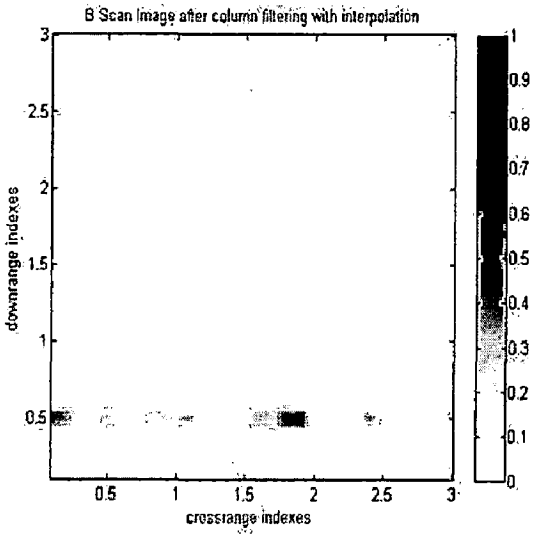


(a)Column filter applied on clutter removed image

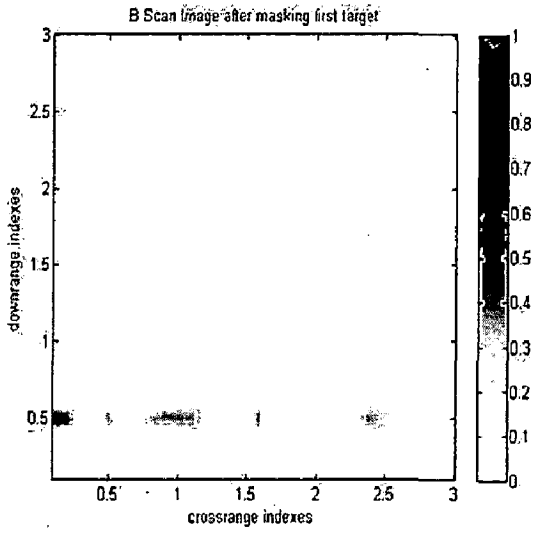


(b)B-Scan after first target detected and masked

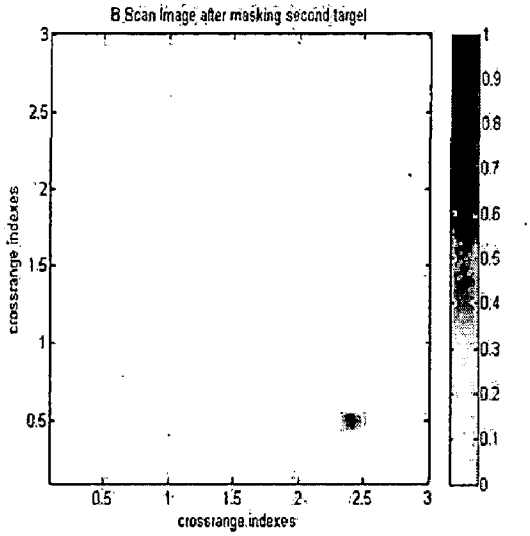


(c)B-Scan after second target has been detected and masked

**Figure 2: Steps involved in target classification**

**b) Steps involved in target identification and classification with targets at 20 cm and soil moisture level 20%**

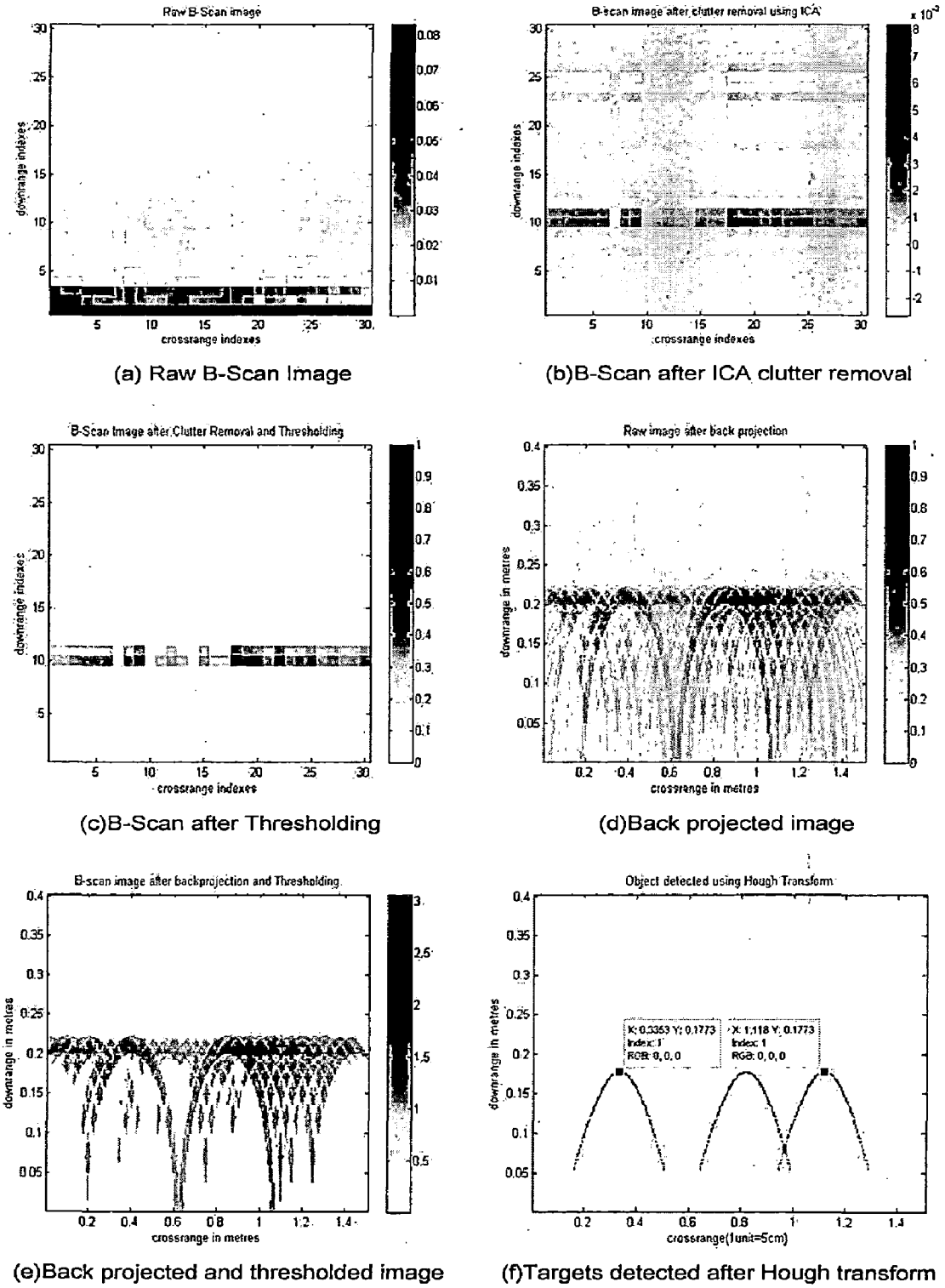


(a) Raw B-Scan Image

(b)B-Scan after ICA clutter removal

(c)B-Scan after Thresholding

(d)Back projected image

(e)Back projected and thresholded image

(f)Targets detected after Hough transform

**Figure 3: Steps involved in target detection**

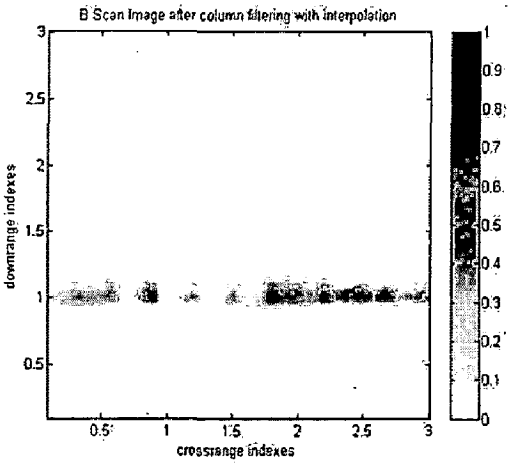


(a)B-Scan after column filtering

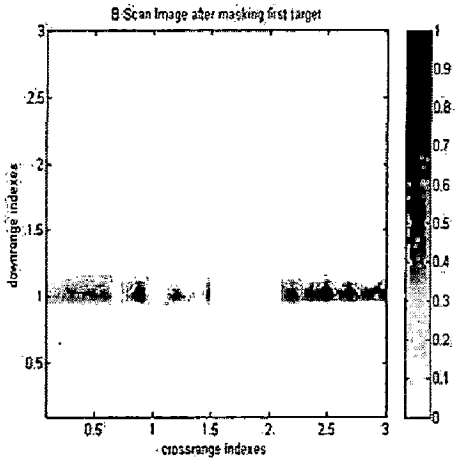


(b)B-Scan after first target has been identified and masked

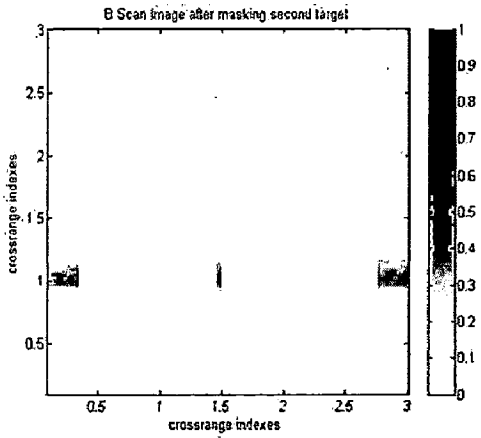


(c)B-Scan after second target has been identified and masked

**Figure 4: Steps involved in target classification**

## c) GUI developed for real time target detection and classification

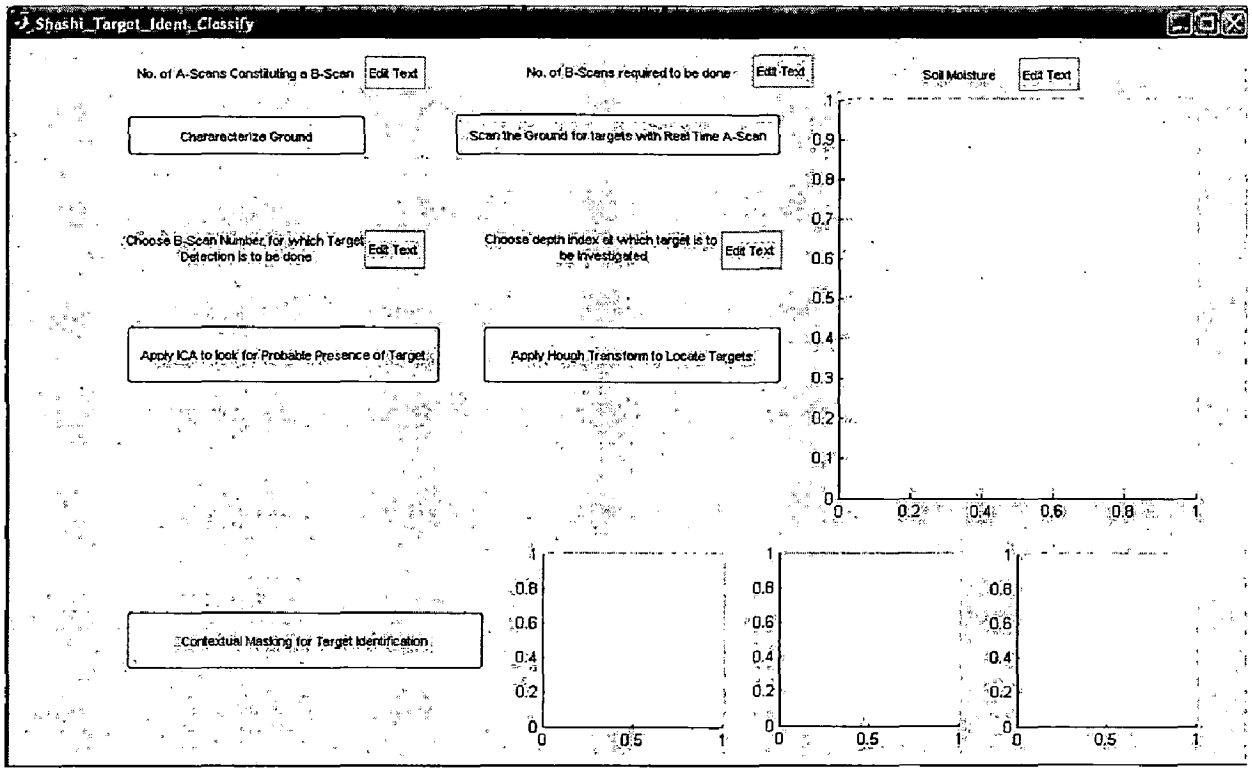


**Figure 5: GUI developed for real time target detection and classification**